MICROCOPY RESOLUTION TEST CHART

NATIONAL BUREAU OF STANDARDS-1963-A

R & D 3035-R-EN

UNCLASSIFIED

REPORT DOCUMENTATION PAGE		READ INSTRUCTIONS BEFORE COMPLETING FORM
1. REPORT NUMBER	2. GOVT ACCESSION NO. AD-A138 753	3. RECIPIENT'S CATALOG NUMBER
4. TITLE (and Subtitle) ACOUSTIC-TO-SEISMIC COUPLING OVER POROUS GROUND SURFACES		5. TYPE OF REPORT & PERIOD COVERED FINAL TECHNICAL REPORT Jun 81 - Oct 83
		6. PERFORMING ORG. REPORT NUMBER
7. AUTHOR(s) KEITH ATTENBOROUGH, NICHOLAS W. HEAP, TREVOR L. RICHARDS, V.V.S.S. SASTRY		8. CONTRACT OR GRANT NUMBER(s) DAJA37-81-C-0210
9. PERFORMING ORGANIZATION NAME AND ADDRESS FACULTY OF TECHNOLOGY, OPEN UNIVERSITY WALTON HALL, MILTON KEYNES, MK7 6AA, ENGLAND		10. PROGRAM ELEMENT, PROJECT, TASK AREA & WORK UNIT NUMBERS 61102A-IT161102-BH57-01
11. CONTROLLING OFFICE NAME AND ADDRESS USARDSG-UK BOX 65, FPO NEW YORK, NY 09510		12. REPORT DATE OCTOBER 1983
		13. NUMBER OF PAGES 191
14. MONITORING AGENCY NAME & ADDRESS(if different from Controlling Office)		15. SECURITY CLASS. (of this report) UNCLASSIFIED
		15a. DECLASSIFICATION/DOWNGRADING SCHEDULE

16. DISTRIBUTION STATEMENT (of this Report)

APPROVED FOR PUBLIC RELEASE; DISTRIBUTION UNLIMITED

17. DISTRIBUTION STATEMENT (of the abstract entered in Block 20, if different from Report)

MAR 6   1984

A

18. SUPPLEMENTARY NOTES

19. KEY WORDS (Continue on reverse side if necessary and identify by block number)

Acoustic/ seismic/ coupling/ wave propagation/ spherical waves/ plane waves/ acoustic surface wave/ rigid porous solid/ poro-elastic solid/ semi-infinite layer/ rigidly-backed layer/ dilational waves/ shear wave/ model experiments/ fibreglass data/ air-jet source/ spark source/ air and water-saturated soils/ probe microphone data/ intensity ratio/ branch cut integrals/light fluid limit

20. ABSTRACT (Continue on reverse side if necessary and identify by block number)

1.1 Use of seismic sensors in battle-field surveillance is frequently made difficult by buried geophone response to above ground acoustic disturbances. The response to such acoustic-to-seismic coupling frequently generates signals in the same frequency range and of the same amplitude as those purely seismic signals that are of interest in surveillance. This report is concerned with the theoretical understanding of the phenomenon of acoustic seismic coupling.

DD FORM 1473 EDITION OF 1 NOV 65 IS OBSOLETE

UNCLASSIFIED

1.2 In the work reported here, the penetration of sound into the ground is predicted for both spherical and plane acoustic waves incident upon two models of the ground viz (i) a rigid porous solid half-space and (ii) a poro-elastic granular half-space. In addition the plane wave analysis is extended to incidence on a rigidly-backed finite rigid-porous layer

1.3 In the frequency range of interest (1 - 1000 Hz) the rigid porous model of the ground is found to be sufficiently locally-reacting to predict identical results for spherical and plane wave incidence. The predictions are found to correspond to buried microphone measurements in sand and soils of above-ground acoustic disturbances. Furthermore it is found possible to predict the results of model measurements using continuous and pulsed acoustic sources and microphone receivers above and below the surface of fibreglass blanket.

1.4 The plane-wave analysis for a poro-elastic half-space predicts the existence in general, of three body waves i.e. two compressional waves which we call "fast" and "slow" borrowing from the literature on propagation in water saturated sediments and one shear wave. The solid particle motion, in general is the result of the contributions from all three wave types. At normal incidence the contribution is mainly from the fast-wave type travelling predominantly in the solid grains. The pore-fluid particle motion has a primary contribution from the slow wave type and for dry soils is practically identical to that predicted by the rigid porous model of the ground.

1.5 The predictions of the poro-elastic models for normally-incident plane-wave incidence are found to explain qualitative features of plots of intensity ratios reported in the literature and calculated from simultaneous. measurements with microphones and geophones collocated ie. vertically separated above and below porous ground surfaces.

1.6 The analysis for spherical wave incidence on a poro-elastic half-space predicts that the surface motion potentially results from five wave contributions viz. the incident wave and four coupled waves in the poro-elastic medium. The coupled waves consist of two compressional waves, a shear wave and a Rayleigh-type wave.

1.7 Computations of the near- and far-field approximations of the surface motion, resulting from an above-ground acoustic point source, for a horizontal source-receiver separation of 100m and using a set of typical soil parameters, show that, for source heights of zero and 1M (grazing-incidence) and low-frequencies i.e. less than 100 Hz the Rayleigh-type wave is dominant. At higher frequencies for grazing-incidence or for all frequencies if the source is elevated to 50M, computations reveal that the direct-coupled plane-wave contribution is dominant. All contributions are predicted to decrease with increasing frequency which is in accordance with the trend exhibited by measured data.

CONTENTS :

LIST OF FIGURES AND CAPTIONS

LIST OF SYMBOLS

CHAPTER 2

$\kappa_{1,2}$ — Propagation constants in medium 1 and 2

$\rho_{1,2}$ — densities of media 1 and 2

$R_{1,2}$ — distance from source and image to observer respectively

$M = \rho_1/\rho_2$ — ratio of densities

$n = \kappa_2/\kappa_1$ — ratio of propagation constants

κ — complex variables of integration

CHAPTER 4

$\rho_c(\omega)$ — complex density of fluid

$J_{0,1}(.)$ — cylindrical bessel functions of zeroth and first order

κ_c — pore parameter, Eq.(4.3)

ρ_0 — density of fluid

ν — kinematic viscosity

N_{Pr} — Prandtl number

$C(\omega)$ — frequency dependent complex compressibility Eq. (4.8)

n — oscillatory flow pore shape factor

q — tortuosity

Ω — volume porosity

μ — dynamic viscosity

s — steady flow pore shape factor

$Z/\rho c$ — relative surface impedance

n' — grain shape factor

m — hydraulic radius, Eq.(4.23)

B — permeability, Eq.(4.24)

CHAPTER 5

$\phi_{1,2}$	scalar potential
$\psi_{1,2}$	vector potential
$\underline{u}$	skeletal frame displacement
$\underline{U}$	fluid displacement
$\underline{w}$	displacement of the fluid relative to the frame
H,C,M	elastic constants
ρ	average mass density
ρ_f	density of fluid
m	'effective fluid density' see paragraph following Eq.(5.2)
K_r	bulk modulus of the individual grains
K_f	bulk modulus of the pore fluid
G_b	shear modulus
K_b	bulk modulus of the assemblage of particles
η	dynamic viscosity of fluid
k	permeability of porous frame of dimension $[L]_2$
n^2	grain shape factor
$F(\lambda)$	complex viscosity correction factor Eq. (5.3)
μ	kinematic viscosity of fluid
γ	ratio of specific heats
P_o	atmospheric pressure
P,Q,R,	elastic parameters, Eq.(5.12)
N	shear modulus of the solid and composite
$a'_s\ a''_s$	amplitudes of slow and fast waves
a^r	amplitude of shear wave
$u_{x,y}$	displacements in the solid
$U_{x,y}$	displacements in the fluid
e_{xx}	strain components in the solid
ε	fluid dilatation
σ_{ij}	strain tensor
δ_{ij}	Dirac's symbol
V_s	normal solid particle velocity

k', k'' and k^r	propagation constants for slow, fast and shear waves
k_o	wave number in air
p	pressure at the surface
θ', θ'' and θ^r	angles of refraction of slow, fast and shear waves
$\Gamma_{1,2}$	Eq. (5.26)
T', T'', T^r	relative amplitudes, Eq. (5.28)

Chapter 6

ψ	scalar potential
p	acoustic pressure
K_a	bulk modulus of air
$\underline{u}$	displacement vector
$\underline{w}$	displacement of fluid relative to the solid
$\underline{U}$	absolute fluid displacement
ω	porosity
$\phi_{2,3}$	scalar potentials
$\times_{1,2}$	vector potentials
H and μ	elastic moduli of the medium
M	effective bulk modulus of the fluid in the pores
ρ_1	density of fluid
ρ_2	complex density, Eq.(6.15)
ρ	average density of the porous medium
m	effective inertial density of the fluid in the pores
η	viscosity of fluid
k	permeability of the porous medium
α	a parameter which relates changes in pore volume to overall
t_{ij}	changes in volume
$k_{1,2,3,4}$	'effective stress' propagation constants Eqs. (6.14), (6.20)
$k'_{2,3}$	see Eqs. (6.33) and (6.34)

1 INTRODUCTION

1.1 Scientific interest in the phenomenon of *acoustic-to-seismic coupling* has
     spanned at least the last thirty-two years [1.1]. The motivations have
     included seismic exploration using sources in air, studies of sonic boom
     effects, and studies of the ground-induced motion due to rocket launches.
     Furthermore ground-air coupling is an important phenomenon in any attempt
     to monitor sub-surface conditions acoustically e.g. to detect buried objects
     using sources in air.

1.2 Systematic experimental studies of the near surface seismic signals induced
     by air-borne acoustic waves are relatively recent. Bass et al [1.2, 1.3]
     have used continuous signals from a loudspeaker source and impulsive signals
     directed along a line array of triaxial geophones and microphones and have
     reported results in terms of the squared ratio of surface seismic particle
     velocity to sound pressure immediately above the surface termed the intensity
     ratio. Similar measurements have been carried out by Powell [1.1] and,
     recently, by several delegates of NATO AC Panel III RSG II on mechanical Waves [1.4].

1.3 Typical results show that
        (i)   the intensity ratio decreases with frequency overall but has several
              peaks some of which fall outside the "exciting" frequency band
        (ii) the coupling is not very sensitive to "incident" angle of excitation
        (iii) the time of first arrival response at the seismic sensor to an above-ground
              acoustic impulse corresponds to the speed of sound in air and is followed
              by a dispersive Rayleigh wave train.
        (iv) the amplitude of seismic disturbance is unaffected by depth up to 1.5 m.
        (v)   the nature of the acoustically-induced seismic disturbance is strongly
              affected by the presence of snow.

1.4 Cress and Flohr (1.3) have attempted an analysis of the coupling using assumptions of

    (i) perfectly flat, homogeneous and infinitely deep ground.

    (ii) continuous vertical displacement across the boundary.

    (iii) continuous vertical stress across the boundary.

    (iv) zero horizontal stress components at the boundary, and

    (v) compressional wave velocity in soil $= 34\frac{1}{2}$ ms^{-1} (i.e. and equal to that in air).

The boundary conditions are used to obtain a set of equations relating the reflected and transmitted displacement at the ground surface and hence the vertical component of velocity. It is assumed further that the acoustic pressure can be related to the particle velocity in air at the surface by the usual plane wave relation.

The predicted intensity ratio is found to be independent of frequency and very sensitive to angle of incidence. Both of these conclusions are at variance with measured results.

1.5 This report is concerned with the development of a theory for the phenomenon of acoustic-to-seismic coupling which is in accordance with observation. The starting point is the well-developed theory for propagation of sound from a point source above a locally-reacting boundary. Appendices 1 and 2 repeat and confirm this analysis. In Chapter 2 the analysis is extended to predict the field within the locally-reacting homogeneous medium. The prediction is found to depend crucially upon the acoustical characteristics of the locally-reacting medium. Chapter 3 describes "model" experiments carried out in a anechoic chamber to provide data for detailed comparison with theoretical predictions and Appendix 3 describes the basis for the models and the instrumentation. Consequently, in Chapter 4, a development of the Rayleigh model (1.5) for such a medium is found, in combination with the propagation (transmission) theory, to give predictions that agree both with the data

obtained in "model" measurements using fibreglass as the "ground"
medium and with microphone probe measurements made outdoors in sound
and soils.

1.6   These predictions do not agree, however, with the geophone data reviewed
in 1.3. Thus, in Chapter 5 and Appendix 4, a semi-infinite, homogeneous
poro-elastic model of the ground is adopted (1.6) and used to give
predictions of the surface intensity ratio after a review of model
parameters appropriate to sands and surficial soils.

Predictions are obtained for the surface intensity ratio due to acoustic
plane waves normally incident on both a semi-infinite and a finite depth
rigidly-backed poro-elastic layer and obliquely-incident on a semi-infinite
poro-elastic medium. Finally, since the plane wave analysis will not be
valid near grazing-incidence, the theory of spherical wave incidence on
an air/poro-elastic boundary is derived in Chapter 6 and Appendix 5 and shows
the possibility of five wave contributions at the interface. Near- and far-
field approximations are used in Appendix 5 to show the relative importance
of the various wave types in acoustic-to-seismic coupling. The predictions
are qualitatively in agreement with features of the measured data that are
available in the literature.

LITERATURE CITED

[1.1]   R.F. POWELL, Acoustic wave propagation near the ground surface

        M.Sc. (Applied Acoustics) Dissertation Chelsea College

        University of London September 1982.

[1.2]   H.E. BASS, L.N. BOLEN, D.H. CRESS, J. LUNDIEN AND M. FLOHR,

        Coupling of air-borne sound into the earth: frequency dependence

        J. Acoust. Soc. Am 67 1502-±506 (1980)

[1.3]   M.D. FLOHR and D.H. CRESS Acoustic-to-seismic coupling properties

        and applications to seismic sensors, Technical Report EL-79-1

        U.S. Army WES, February 1979.

[1.4]   NATO AC PANEL III RSG-II Final Report (1983)

[1.5]   K. ATTENBOROUGH, Acoustical characteristics of rigid fibrous absorbents

        and granular materials J. Acoust.Soc Am 73 (3) 785-799 (1983)

[1.6]   K. ATTENBOROUGH, Influence of Microstructure on viscous attenuation

        in unconsolidated marine sediments, Proc. Inst of Acoustics

        Acoustics and the Sea Bed ed. N.G. Pace Bath University Press (1983)

2   TRANSMISSION OF A SPHERICAL WAVE AT A RIGID POROUS INTERFACE

2.1 Introduction

The sound field due to a point source above a plane interface separating
two semi-infinite fluid media is a problem of great interest to those
concerned with the propagation of sound over different types of ground
surface, where the soil can be approximated by a rigid, porous absorbing
medium [2.1]. Considerable effort has been made to evaluate the field
in the upper medium (air) in the short-wave, asymptotic limit. A geometric
approximation is adequate for sufficiently large elevation of the source
and/or receiver, but this breaks down at grazing incidence where small

correcting terms play an increasingly dominant role. The grazing-
incidence case, of course, is precisely that which applies in long-range
propagation studies. One of these correcting terms has the form of a
surface wave and in Appendix 2 we show that it corresponds to a physically-
real surface wave.

The evaluation of the field in the lower medium has recieved comparatively
little attention, but Paul ([2.2], [2.3]) and Brekhovskikh [2.4]
discuss the problem in some detail. Our motivation for considering this
case arises from a desire to compare the magnitude of sound waves penetrating
into the ground with that of any accompanying seismic disturbance.

We start in a similar manner to Paul and Brekhovskikh, that is by expressing
the solution as an inverse Hankel transform. The resulting integral
is then evaluated asymptotically using two steepest descent contours which
pass around the two branch points of the integrand. The presence of a pole,
which affects the solution at grazing incidence over ground having a
high impedance, is also taken into account. We only consider cases for which
the refractive index has a magnitude greater than unity.

In his first paper [2.2] Paul integrates around two vertical (in the plane of complex wavenumber) paths originating at the branch points, as opposed to the true saddle paths that we use. This initial simplification still results in complicated algebraic espressions and furthermore no ready physical interpretation is possible in terms of geometric rays. He deals with the pole by subtraction, and while this method appears to be essentially equivalant to ours, we feel that the final result is not expressed so simply.

Paul later considers alternative integration paths [2.3] which in part resemble more closely those used here. He does not consider the presence of the pole in this work.

Brekhovskikh [2.4] does not describe his derivation in detail, but it would appear that he uses the true saddle paths as he is able to identify geometrically the two wave types. It is not made clear, however, how to deal with a complex refractive index (i.e. an absorbing medium) except in an approximate form, and the problem of the pole is only mentioned briefly.

In a more recent paper by Candel and Crance [2.5] the related problem of a horizontal line source is discussed. Their stationary phase method can only give a single term which is the same as that obtained using geometrical acoustics, and is therefore not suitable at grazing incidence. They do not acknowledge the presence of a lateral wave, nor is the pole taken into account.

2.2 The integral representation for the field

Expressed as an inverse Hankel transform the velocity potential in the lower medium is given by [2.2]

$$\phi = V(z_1,z_2,r) = \frac{M}{4\pi} \int_{-\infty}^{\infty} \frac{e^{-\nu_1 z_1 - \nu_2 z_2 + iKr}}{\nu_1 + M\nu_2} \; H_o^1(Kr)e^{-iKr} \; KdK$$

$$(2.1)$$

where z_1, z_2 are the depth of source and height of receiver and r is their horizontal separation,

$$\nu_1 = (K^2 - k_1^2)^{\frac{1}{2}}, \quad \nu_2 = (K - k_2^2)^{\frac{1}{2}}, \; Re\nu_1, \; Re\nu_2 > 0,$$

k_1, k_2 are the wavenumber (complex in general) in the upper and lower media, and

$$M = \rho_1/\rho_2 \; , \text{ the ratio of densities (again complex)}$$

Equation (2.1) can be used to obtain an expression for the field in the upper medium:

$$\phi = \frac{e^{ik_1R_1}}{4\pi R_1} - \frac{e^{ik_1R_2}}{4\pi R_2} + \frac{1}{M} V\,(H,0,r) \qquad\qquad (2.2)$$

where H is the sum of source and receiver heights and R_1, R_2 are the distances from the receiver to the source and to its image.

2.3 The steepest descent method with a pole near a saddle point

The rapid oscillation of the integrand in equation (2.1) for large source-receiver separations can be handled satisfactorily by using the saddle-point method.

In general we need to evaluate integrals of the form

$$I = \int_{-\infty}^{\infty} A(K) e^{f(K)} dK \qquad (2.3)$$

in which the behaviour of $f(K)$ causes the integrand to oscillate rapidly. The saddle points occur where $f'(K) = 0$, and the steepest descent paths emanate from these in a direction in the complex plane in which the exponential term decays most rapidly. The imaginary part of $f(K)$ is constant along a steepest descent path and can be taken outside the integral, leaving a purely real exponential term which decays on either side of the saddle point. If $f'(K_s) = 0$, then

$f(K) = f(K_s) - S^2$ for real S gives the behaviour of the exponent along the steepest descent path. The integral along this path becomes

$$I_{SDP} = e^{f(K_s)} \int_{-\infty}^{\infty} A(K) \frac{dK}{dS} e^{-S^2} dS \qquad (2.4)$$

If $A(K) \frac{dK}{dS}$ can be expanded in a power series in S with a large radius of convergence we can integrate the successive terms. With $A(k)dK/dS = \phi(S)$, this results in

$$I_{SDP} = \pi^{\frac{1}{2}} e^{f(K_s)} \left[\phi(0) + \frac{1}{4} \phi''(0) + \ldots \right] \qquad (2.5)$$

If one or more (but not necessarily all) of the steepest descent paths are added in such a way that the resulting contour can be deformed into the real axis without crossing any branch points, then the resulting integral, along with the contributions from any poles crossed, will be equal to the integral in equation (2.3)

If the radius of convergence of the series for $\phi(S)$ is limited by the presence of a pole equation (2.5) may be inapplicable. In this case we write

$$\phi(S) = \psi(S) / (S - S_p) \qquad (2.6)$$

and use the series for $\psi(S)$, which has no pole, instead. We now obtain

$$\begin{aligned}
I_{SDP} = e^{f(K_s)} \Big[&\psi(0) I_0 \\
&+ \psi'(0) (S_p I_0 + \sqrt{\pi}) \\
&+ \tfrac{1}{2}\psi''(0) (S_p^2 I_0 + S_p \sqrt{\pi}) \\
&+ 1/6\, \psi'''(0) (S_p^3 I_0 + S_p^2 \sqrt{\pi} + \tfrac{1}{2}\sqrt{\pi}) \\
&+ \ldots\ldots \Big] \qquad (2.7)
\end{aligned}$$

where
$$I_o = \int_{-\infty}^{\infty} \frac{e^{-S^2}}{S-S_p} \, dS$$

Noting that $\psi(S_p) = \psi(0) + \psi'(0)S_p + \frac{1}{2}\psi''(0)S_p^2 + \ldots$

and making use of equation (2.6) gives

$$I_{SDP} = \pi^{\frac{1}{2}} e^{f(K_g)} \; [\psi(S_p) \; (I_o \sqrt{\pi} + \frac{1}{S_p} + \frac{1}{2S_p^3} + \ldots)$$
$$+ \phi(0) + \frac{1}{4}\phi''(0) + \ldots] \qquad (2.8)$$

It can be seen that

$$I_{SDP} \rightarrow \pi^{\frac{1}{2}} e^{f(K_g)} \; [\psi'(0) + 1/12\psi'''(0) + \ldots]$$

as $S_p \rightarrow 0$.

The expression therefore remains finite as the pole approaches the saddle point.

We can write

$$I_o = i\pi \; \{W(S_p) - 2e^{-S_p^2} \; H \; [-Im(S_p)]\}$$

where $W(S_p) = e^{-S_p^2} \, erfc \, (-iS_p)$ and $H[\ ]$ is the Heaviside step function. This second term is cancelled by the contribution from the pole residue if the pole lies between the SDP and the real axis, leaving the total contribution

$$I^* = \sqrt{\pi} e^{f(K_g)} \; [\psi(S_p) \; \{i\sqrt{\pi} \; w(S_p) + \frac{1}{S_p} + \frac{1}{2S_p^3} + \ldots)$$
$$+ \phi(0) + \frac{1}{4}\phi''(0) + \ldots] \qquad (2.9)$$

To investigate the behaviour of this expression for large values
of S_p we use the asymptotic expansion

$$i\sqrt{\pi}\, w(S_p) = -[\frac{1}{S_p} + \frac{1}{2S_p^3} + \frac{3}{4S_p^5} + \ldots]$$

$$+\ 2H\ [-Im(S_p)]e^{-S_p^2}$$

Substituting into equation (2.9) using only those terms shown gives

$$I^* = \sqrt{\pi}\, e^{f(K_s)}\ [\phi(0) + \frac{1}{4}\phi''(0)$$

$$+\ 2H\ [-Im(S_p)]\ e^{-S_p^2}\, \psi\ (S_p)]$$

$$+\ 0\left(\frac{1}{S_p^5}\right)$$

(2.10)

As expected, this expression approaches the behaviour of equation (2.5)
along with the contribution from the pole when it lies between the SDP
and the real axis. In this application the latter term gives rise
to the famous 'surface wave'.

Thus the SDP integral may calculated using equation (2.5) and if
the pole is near the saddle point we simply add the extra terms shown
in equation (2.9). This straightforward procedure appears to be
much less cumbersome than previous methods such as subtraction of the
pole.

The subsequent means used to evaluate the expression in equation
(2.5) are well-established and Brekhovskikh [2.4] gives a good
account of these, and the appropriate formulae.

For the extra term in equation (2.3.9) we use

$$\psi(S_p) = \lim_{K \to K_p} (K - K_p)A(K),$$

(2.11)

where K_p is the position of the pole in the complex K plane.

Returning to equation (2.1) we have

$$f(K) = -\nu_1 z_1 - \nu_2 z_2 + iKr$$

(2.12)

and

$$A(K) = \frac{M}{4\pi} [H'_o (Kr)e^{-iKr}] K/(\nu_1 + M\nu_2).$$

(2.13)

For grazing incidence, with z_1, $z_2 \ll r$, there are two saddle points, one near $K = k_1$ and another near $K = k_2$. The steepest descent paths through these points can be used to close the contour of integration without enclosing the branch points. The pole, given by $\nu_1 + M\nu_2 = 0$, can closely approach the first of these saddle points at grazing incidence if $M \ll 1$, $k_2 > k_1$, and will be dealt with accordingly using equation (2.9)

At sufficiently large source heights or receiver depths closure of the path of integration can be effected by using only one of the two paths. We will not pursue this matter further, but both Paul [2.3] and Brekhovskikh [2.4] consider such cases.

2.4 The geometrical wave

The contribution from the saddle point near the $K = k_1$ branch point corresponds to the ray refracted according to Snell's law in the geometrical approximation.

We locate this saddle point using the interation

$$\alpha_{i+1} = z_1\beta \ / (r - z_2\beta_i \ /\gamma_i) \qquad (2.14)$$

where $\nu_1 = -ik_1\alpha$, $\nu_2 = -ik_1\gamma$, $K = k_1\beta$ with $\beta_i = (1 - \alpha_i^2)^{\frac{1}{2}}$,

$$\gamma = (\alpha_i^2 + n^2 - 1)^{\frac{1}{2}}, \quad n = k_2/k_1.$$

For large angles of incidence (i.e. $z_1 < r$) $\alpha_1 = 0$ is a suitable starting value, and the calculations may be performed for complex k_1 and k_2. If $z_1 = 0$ then $\alpha = 0$, but equation (2.5) now becomes

$$I_{SDP} = \pi^{\frac{1}{2}} e^{ik_1(\alpha z_1 + \gamma z_2 + \beta r)}$$

$$\times \left(\frac{-2}{f''}\right)^{\frac{1}{2}} \left[A\left(1 + \frac{1}{8} \frac{f^{IV}}{(f'')^2} - \frac{5}{24} \frac{(f''')^2}{(f'')^3} \right) \right.$$

$$\left. + \frac{1}{2} \frac{A'f'''}{(f'')^2} - \frac{1}{2} \frac{A''}{f''} \right] \qquad (2.15)$$

where

$$f'' = \frac{-i}{k_1} \left[\frac{z_1}{\alpha^3} + \frac{z_2}{n\gamma^3} \right]$$

$$f''' = \frac{-3i\beta}{k_1^2} \left[\frac{z_1}{\alpha^5} + \frac{z_2}{n^2\gamma^5} \right]$$

$$f^{IV} = \frac{-3i(4\beta^2 + 1)}{k_1^3} \left[\frac{z_1}{\alpha^7} + \frac{z_2}{n^3\gamma^7} \right]$$

and

$$A = \frac{iMk_1\beta}{4\pi} \left(\frac{2}{i\pi k_1\beta r} \right)^{\frac{1}{2}} \left(1 + \frac{1}{8ik_1\beta r} \right) \Big/ (\alpha + M\gamma).$$

The first two terms of the asymptotic expansion

$$H_o^1(z)e^{-iz} \approx \left(\frac{2}{i\pi z} \right)^{\frac{1}{2}} \left(1 + \frac{1}{8iz} + \dots \right)$$

have been used. This is acceptable if $|k_1\beta r| \gg 1$, that is when $k_1 r \gg 1$ and the angle of incidence is large.

There is little necessity in seeking further simplification of equation (2.15) once the appropriate differentiations of $A(k)$ have been carried out, except to ensure that the correct value is given at $\alpha = 0$. To do this we examine the limiting behaviour of the various terms as $\alpha \to 0$, and find that only the last two terms in the square brackets contribute.

2.5   The lateral wave

To find the second saddle point we take into account the
fact that at grazing incidence it is close to the $K = k_2$
branch point, and consequently $|\nu_2|$ is small, and ν_1 is
predominantly real. We re-define α, β, γ and use the
iteration

$$\gamma_{i+1} = z_2 \beta_i / (r + iz_1 \beta_i / \alpha_i) \qquad (2.17)$$

where $\nu_1 = k_2 \alpha$, $\nu_2 = -ik_2 \gamma$, $K = k_2 \beta$

and $\beta_i = (1 - \gamma_i^2)^{\frac{1}{2}}$,

$\alpha_i = (1 - \frac{1}{n^2} - \gamma^2)^{\frac{1}{2}}$, $\gamma_o = 0$

This gives

$f(K_s) = - k_2 \alpha z_1 + ik_2 (\gamma z_2 + \beta r)$.

From this we can see that the exponential term decays as z_1,
the height of the source, increases. Further exponential decay
occurs if k_2 has a significant imaginary part.

The steepest descent method may now be applied in the usual
way, and in this case it will not be necessary to take into
account the presence of the pole.

2.6   Special cases

(i) The geometric approximation.

If n, the refractive index, is real, then equation

(2.14)   is satisfied if

$\alpha = \cos \theta_i$,

$\beta = \sin \theta_i$,

$\gamma = n \cos \theta_r$,

To calculate the further terms in equation (2.9) we need to locate the position of the pole using $\nu_1 + M\nu_2 = 0$. At this point

$$\nu_1 = -ik_1\alpha_p, \quad \nu_2 = -ik_1\gamma_p, \quad K = k_1\beta_p$$

where

$$\alpha_p = \frac{M(n^2 - 1)^{\frac{1}{2}}}{(1 - M^2)^{\frac{1}{2}}}$$

$$\beta_p = \frac{(1 - n^2 M^2)^{\frac{1}{2}}}{(1 - M^2)^{\frac{1}{2}}}$$

$$\gamma_p = -\alpha_p / M$$

giving

$$s_p^2 = ik_1 [(\alpha - \alpha_p)z_1 + (\gamma - \gamma_p)z_2 + (\beta - \beta_p)r] \qquad (2.16)$$

$\sin \Theta_i / \sin \Theta_r = n$, (Snell's Law)

and z_1, z_2. r are as depicted:
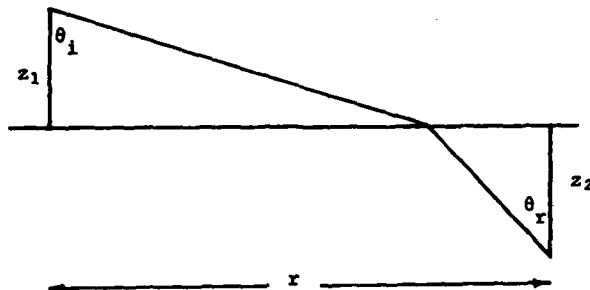
Taking the first term in equation 2.3.15 and using the first term of the expansion for the Hankel function so that

$$I = k_1 \beta \left(\frac{-2\pi}{f^n} \right)^{\frac{1}{2}} \frac{iM}{4\pi} \left(\frac{2}{i\pi k_1 \beta r} \right)^{\frac{1}{2}} / \alpha + M\gamma$$

$$x \; \exp ik_1 (\alpha z_1 + \gamma z_2 + \beta r)$$

$$= \frac{2 \; \sqrt{\sin \theta i} \; \exp ik_1 \; (z_1/\cos\theta_i + nz_2/\cos\theta_r)}{\{r \; (z_1/\cos^3\theta_i + z_2/n \cos^3\theta_r)\}^{\frac{1}{2}} (n \cos\theta_r + \frac{\cos\theta_i}{M})} \qquad (2.18)$$

which is the geometric approximation given by Brekhovskikh

ii) Grazing incidence with a large, complex refractive index.

If n has an appreciable imaginary component then the lateral wave will decay to negligible proportions at large distances.

If z_2 is sufficiently small so that in equation (2.3.14)

$$z_2 \beta / \gamma \; \ll \; r \qquad (2.19)$$

Then $\alpha = \frac{z_1}{r} \beta$

Since $|\beta| < 1$, α is small at grazing incidence
equation (2.3.29) becomes

$$\frac{z_2}{r(n^2 - 1)^{\frac{1}{2}}} \ll 1 \qquad (2.20)$$

Under these circumstances $\alpha = \cos\Theta$ where $\tan\Theta =$
r/z_1

If in addition $\cos\Theta$ is sufficiently small so that the
terms containing z_2 are negligible in f^{11}, f^{111}, f^{1V}
Then $\forall(z_1, z_2, r) \rightarrow$

$$e^{ik_1\gamma z_2} \nu(z_1, 0, r)$$
$$= e^{ik_1 z_2 (n^2 - \sin^2\Theta)^{\frac{1}{2}}} \nu(z_1, 0, r)$$

which gives a simple exponential relationship with the field
on the surface above the receiver. This expression is
derived somewhat less rigorously by Brekhovskikh.

LITERATURE CITED

[2.1]   K. ATTENBOROUGH, S.I. HAYEK, and J.M. LAWTHER

"Propagation of Sound above a Porous Half-space."

J. Acoust. Soc. Am 68, 1493-1501 (1980)

[2.2]   D. I. PAUL, Acoustical Radiation from a Point Source in the presence

of two Media, J. Acoust. Soc. Am. 29, 1102-1109 (1957)

[2.3]   D.I. PAUL, Wave propagation in Acoustic Using the Saddle-Point method.

J. Math. Phys. 38, 1-15 (1959)

[2.4]   L. M. BREKHOVSKIKH, "Waves in Layered Media"

Academic Press, New York (1960).

[2.5]   S. M. CANDEL and C. J. CRANCE, Direct Fourier Synthesis of Waves

in Layered Media and the Method of Stationary Phase, J. Sound. Vib 74(4)

477-498 (1981)

3.   POINT TO POINT PROPAGATION MEASURMENTS USING ACOUSTIC MODELLING

3.0   *Introduction*

In order to validate the foregoing theory for both reflection and
transmission of spherical waves, measurements of point propagation
over plane absorbing and rigid boundaries were made in the small
anechoic chamber. Two cases have been examined in detail:

(i)   attenuation over a rigid boundary;

(ii)   attenuation over and within a porous boundary.

The two materials selected to model these surfaces were varnished
blockboard and Crown 150 fibreglass quilt. The basis and facilities used for
these measurements are outlined in Appendix 3.

3.1   *Rigid surface measurements*

The rigid boundary measurements were made in order to examine the
effects of:

(i)   source height uncertainty;

(ii)   spectral smoothing;

(iii) near surface turbulence; and

(iv)   source and receiver size.

The source and receiver were placed 100 cm apart above the varnished blockboard surface as shown in Figure (3.1). The source and receiver heights could be varied independently.

An air jet was used as the sound source and a 1/4" microphone as the receiver. A block diagram of the measurement system is shown in Figure (3.2)

3.1.1. Source height errors

For a rigid boundary the excess attenuation minima result from the destructive interference of the direct and reflected waves. The frequencies at which these minima occur are therefore very sensitive to source-receiver geometry.

Figure (3.3) shows a comparison of the measured and predicted excess attenuation for propagation over a rigid boundary. The prediction is based upon a source and receiver height of 5 cm. It can be seen that the location of the predicted attenuation minima do not coincide with the measured.

The source height estimate was based upon a measurement of the distance between the rigid surface and the top of the air jet nozzle. However, in view of the large mass of air flowing through the jet, the acoustic centre of the source is unlikely to coincide with the top of the nozzle.
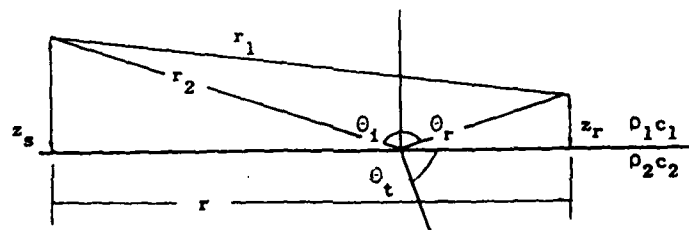
Figure 3.1 Source Receiver Geometry for Model Experiments.
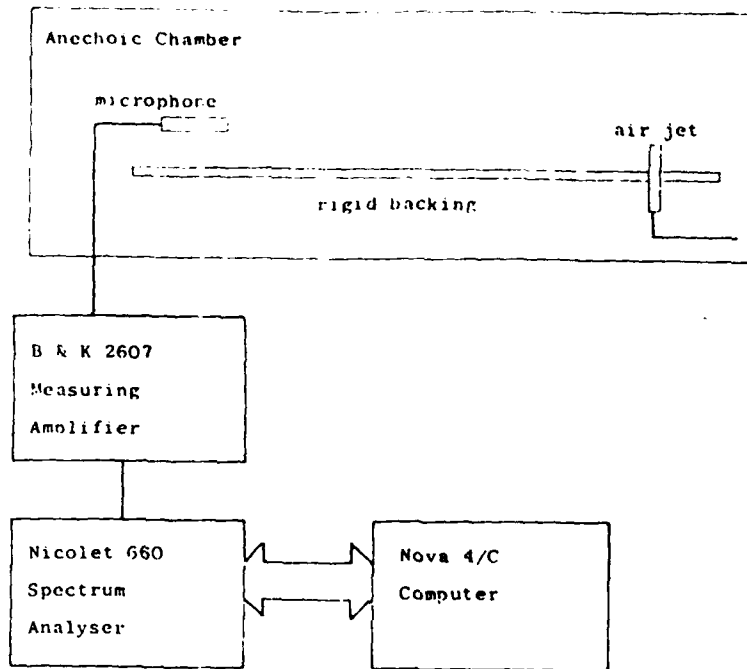
Figure 3.2 Block Diagram of Model Experiment Instrumentation.
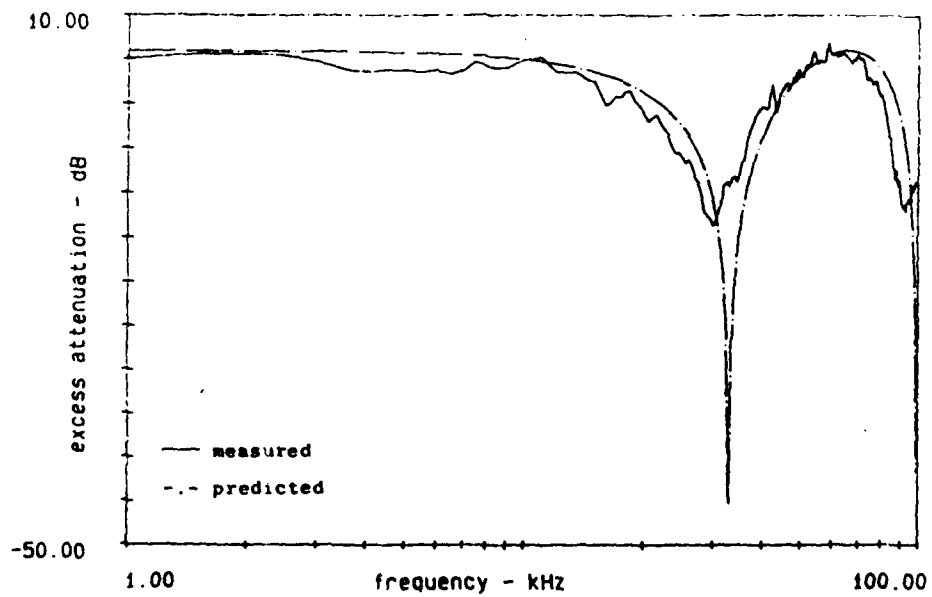
Figure 3.3   Comparison of Measured and Predicted Excess Attenuation
for Propagation over a Rigid Surface.

A better estimate of the source height can be obtained by
varying the height used in the pure-tone predictive algorithm
until the locations of the measured and predicted minima
coincide. The variation in the minima location and source height
can be seen in Figure (3.4) increasing the source height increases
the path length difference and hence moves the minima to lower
frequencies.

The results of this procedure indicated that the source height
is actually 5.3 cm above the rigid surface. A comparison of
the measured and predicted excess attenuation curves, based
upon a source height of 5.3 cm is shown in Figure (3.5)

3.1.2. Spectral smoothing

The predicted excess attenuation curves shown in Figure (3.3)
and (3.5) exhibit much deeper minima than the measured results.
Part of this discrepancy arises from the fact that the predictions
are based upon pure tone interference, whereas the measured values
are based upon the average energy in a 250 Hz wide filter. The
effect of increasing the analysis bandwidth is to increase the
sound pressure at the minima and so smooth the excess attenuation
spectrum.

Correction procedures for the pure-tone calculations have been
derived [3.1] but they cannot account for the observed differences.
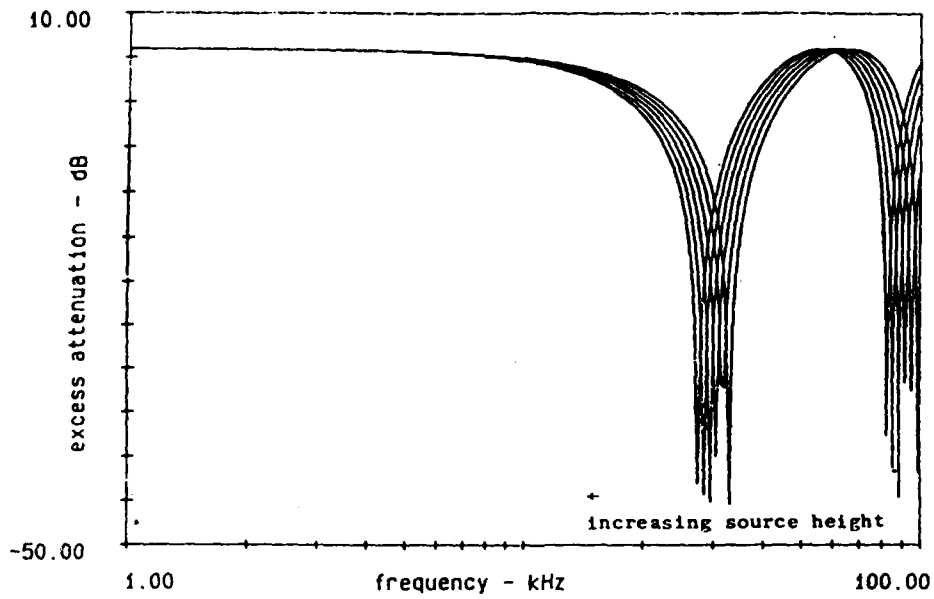
Figure 3. 4 Predicted Excess Attenuation Minima as a Function
of Source Height.
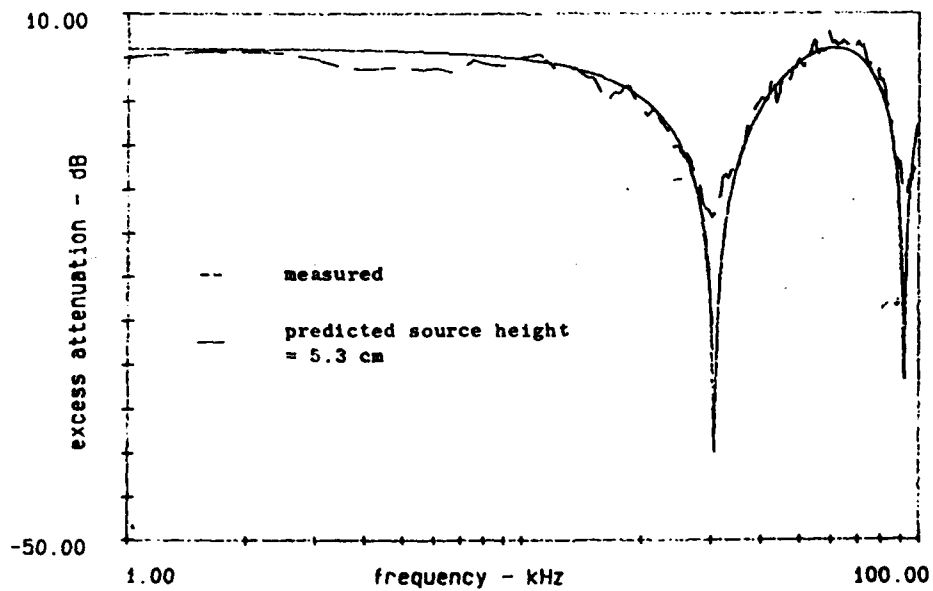
Figure 3. 5   Comparison of Measured and Predicted Excess Attenuation
After Correcting for Source Height.

3.1.3. Near surface turbulence

Another factor to consider when trying to account for the observed
difference between the measured and predicted excess attenuation
curves is the effect of near surface turbulence.

Daigle [3.2] has proposed modelling turbulent air motion as an
additional propagation path length, with random direction and
attenuation. The extra path length disturbs the strong interference
pattern due to the surface. A correction procedure based upon
the measurement of four meterological parameters shows good
agreement with experimental results. These parameters are:

- variance of sound velocity deviations
- variance of air temperature deviations

L_v - sound velocity correlation length

L_t - temperature correlation length

L_v and L_t are measures of the autocorrelation function of the wind
and temperature variations. The time delay corresponding to maximum
correlation is converted to an equivalent path length difference
by multiplying the velocity of sound by the time delay.

Whilst it has not been possible to measure the parameters required
to correct for turbulence effects, an examination of Daigle's
results indicate that they could account for the observed
discrepancies between the measured and predicted excess attenuation
curves.

3.2. Fibreglass Measurements

Two sets of measurements were made using a fibreglass quilt material to model a porous half-space, the first to measure the amplitude ratio of the direct and transmitted sound fields and the second to measure the phase difference between the arrivals of those fields

3.2.1. Amplitude Ratio Measurements

The source receiver geometry for these measurements is shown in Figure (3.1) The surface receiver was a standard 1/4" microphone with a normal protection grid, whilst for the sub-surface receiver the 1/4" microphone was fitted with a nose-cone. The nose-cone serves two purposes, first its shape enables one to ease the microphone through the fibreglass quilt and second it improves the directivity response of the microphone.

The sound source used for these measurements was a mid-range loudspeaker, with the cross-over network removed, and the source signal was derived from a swept frequency oscillator covering the range 100Hz to 15kHz.

In order to minimise the effects of phase distortion that can arise from incoherent averaging of swept frequency signals, a time gating system was employed to synchronise the source signal sweep and the digital sampling of the received signals.

The narrow band spectrum at each of the receiving microphones was measured with the Nicolet 660B spectrum analyser, and the amplitudes ratio obtained from the modulus of the 'transfer function'. Three sets of results are reproduced here as Figure (3.6) Part (a) shows the amplitude ratio and phase difference for a source height of 5cm and a receiver depth of 3cm.
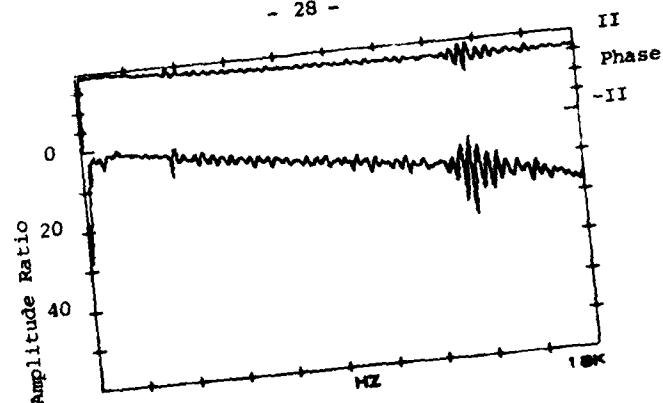
(a)   Receiver Depth 3cm
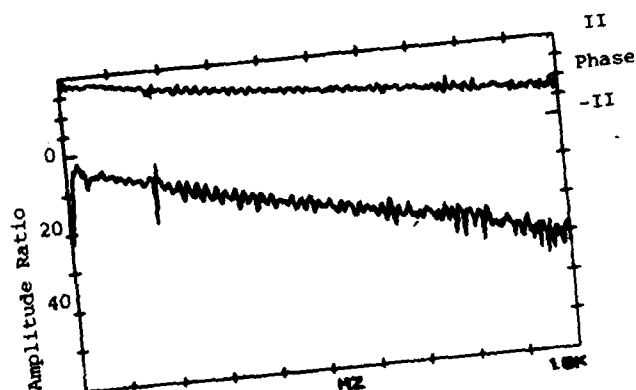
(b)   Receiver Depth 7cm
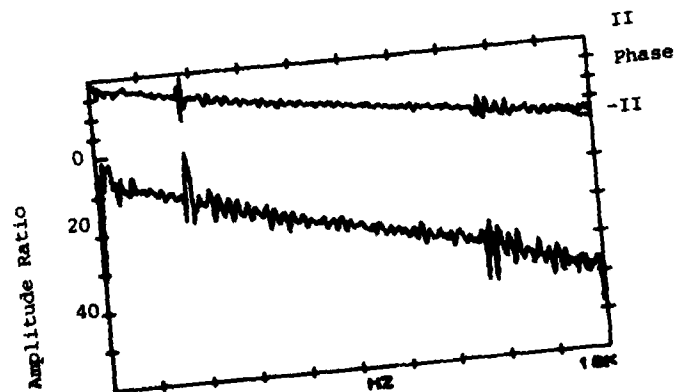
(c) Receiver Depth 10cm

Figure 3.6 Amplitude of Surface and Sub-surface spectra

The ripple in the transfer function at 8kHz, arises from resonance of the loudspeaker diaphragm. Parts (b) and (c) show the results for receiver depths of 7cm and 10cm respectively.

A test of the reliability of these measurements was performed by calculating the coherence function. The results for the three receiver depths, shown in Figure (3.7), indicate that only the estimates of the amplitude ratio at a depth of 10cm for frequencies above 8kHz may be erroneous; since the value of the coherence function drops below 0.8. The reduction in coherence arises from the high level of attenuation at this receiver depth.

All these results show that there is little attenuation of the transmitted sound at low frequencies. At high frequencies the attenuation is dependent upon the depth of the buried receiver. At 10kHz, the upper limit of the measurements, the attenuation increases from 16dB at a depth of 3cm, to approximately 50dB at a depth of 10cm.

3.2.2. Pulse measurements

The time delay measurements were made using the same source receiver geometry described in section (3.2.1), but with the loudspeaker replaced by an electrical spark discharge source. This device produces a low intensity sound pulse of approximately 200 microseconds duration.
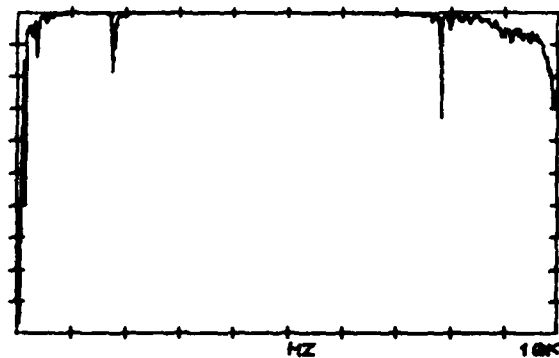
(a)   Receiver Depth 3cm
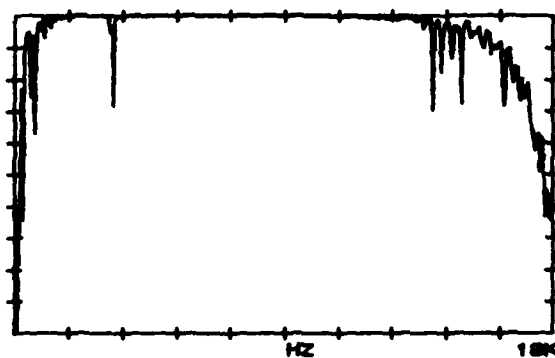
(b)   Receiver Depth 7cm
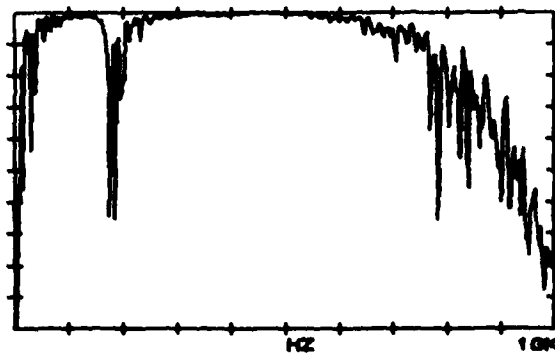
(c)   Receiver Depth 10cm

Figure 3.7   Coherence Function of Surface and Sub-surface Spectra

The trigger transformer circuit used to generate the high voltage spark
can cause significant errors due to electro-magnetic radiation, which
swamps the response of the condenser microphone capsules. In view of
this the spark was operated at its minimum energy level of 4mJ, and time
averaging used to improve the signal to noise ratio.

Examples of the direct (surface microphone) and transmitted pulses are
shown in Figure (3.8) for a source height of 5cm and a receiver depth
of 3cm. The total duration of the signal samples is 4 milliseconds.

The direct microphone signal shows a distinct pulse at 1 millisecond,
corresponding to the spark discharge. The other fluctuations at 2.5
and 3.5 milliseconds correspond to the arrival of reflections from
metallic fittings within the anechoic chamber. The transmitted pulse
occurs at the same time, but the trace shows no subsequent arrivals due
to extraneous reflections within the chamber.

The spectrum of the direct and transmitted pulses are shown in Figure
(3.9) for the range 125Hz - 50kHz. The upper trace corresponds to the
direct pulse and the lower trace the transmitted pulse. The raggedness
of these curves is due partly to the presence of reflection and partly
to the electrical noise in the microphone pre-amplifiers.

The amplitude ratio and phase difference for the direct and transmitted
sound fields are shown plotted in Figure (3.10). Both curves show
considerable fluctuations below 5kHz, due primarily to the poor resolution
of the spectrum analyser at low frequencies. However, the underlying
shape of the amplitude ratio curve is similar to that obtained from the
loudspeaker source measurements.

Measurements of the direct and transmitted pulses were made
for receiver depths of 3, 7 and 10 cm and the results are shown
in Figure (3.11). The pulse at a depth of 10 cm shows considerable
attenuation and is only just discernable above the background
noise level.
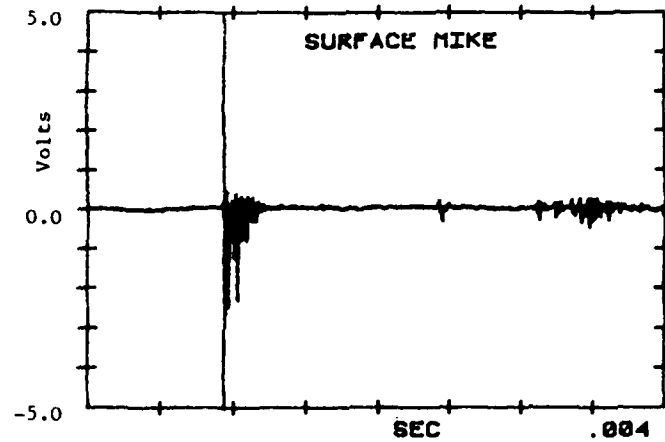
a) Surface Microphone.
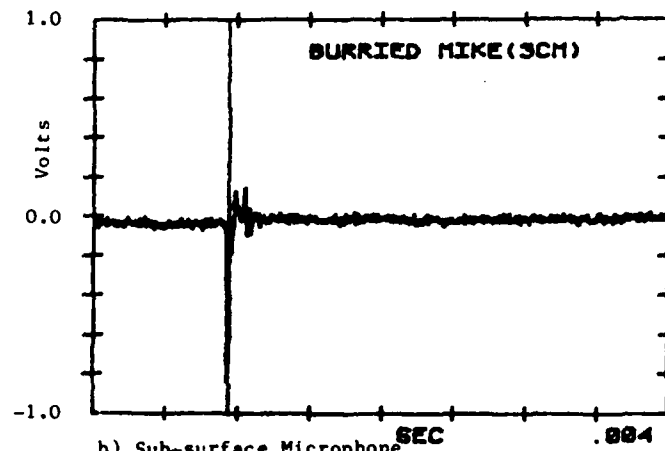
b) Sub-surface Microphone

Figure 3.8 Surface and Sub-surface Microphone
Pulse Waveforms.
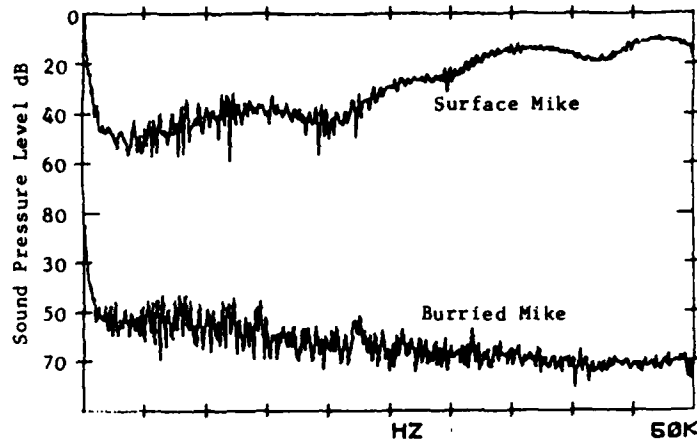
Figure 3.9   Measured Pulse Spectra for Surface
and Buried Microphones.
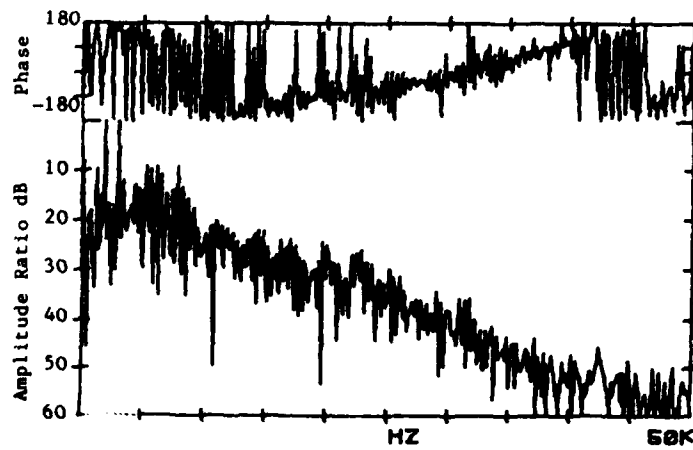
Figure 3.10 Amplitude Ratio of Surface and Sub-surface
Spectra.

a) Surface Microphone

SURFACE MIKE

SEC   .004

b) Sub-surface Microphone at 7cm

BURRIED MIKE(7CM)

SEC   .004

c) Surface Microphone

SURFACE MIKE

SEC   .008

d) Sub-surface Microphone at 10cm

BURRIED MIKE(10CM)

SEC   .008
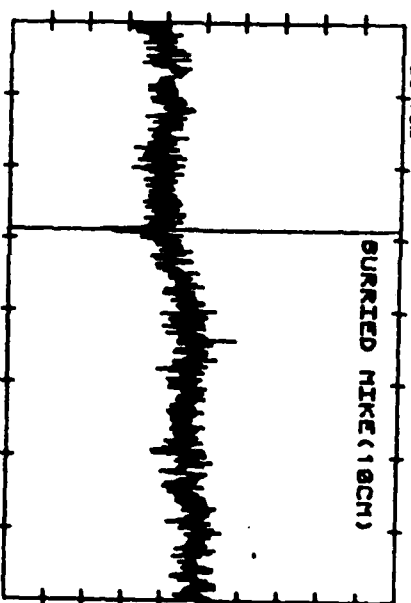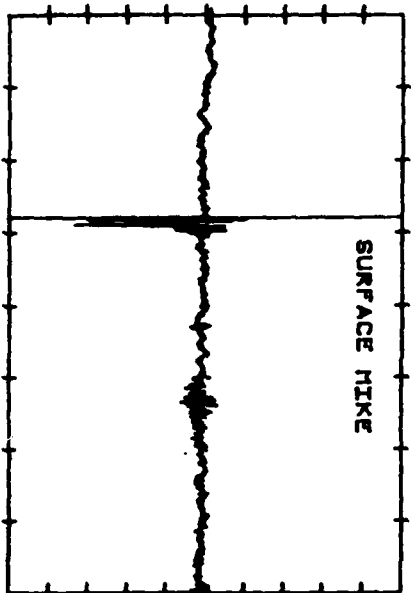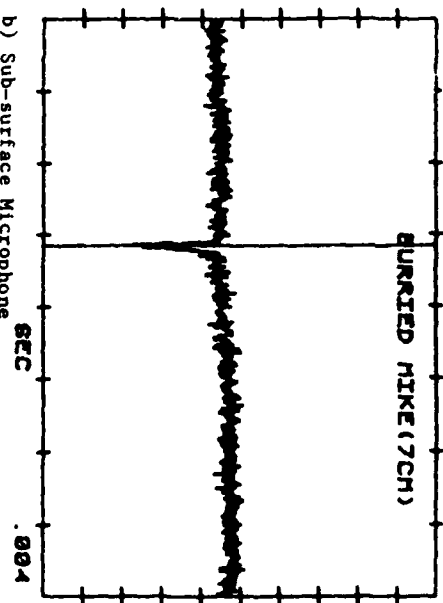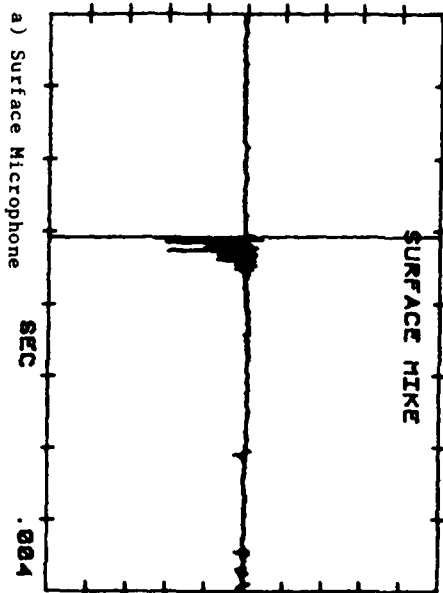
Figure 3.11 Surface and Sub-surface Receiver Pulse Measurements for different Receiver Depths.

LITERATURE CITED

3.1 Sutherland, L.C. and Bass, H.E.: Influence of atmospheric Absorption on the Propagation of Bands of Noise. J.A.S.A. (66) 885-894 1979.

3.2 Daigle, G.A.: Effects of Atmospheric Turbulence on the Interference of Sound Waves Near a Hard Boundary. J.A.S.A.

4 GROUND AS A RIGID POROUS MEDIUM

4.1 Introduction

The theories of spherical wave transmission and reflection at porous boundaries that have been advanced in the previous chapters rely upon the assumption that the ground can be regarded, effectively, either as a locally reacting fluid or as a homogeneous isotropic fluid sustaining a single (compressional) wave type. If the ground is locally-reacting then for computation of the reflected field it may be characterised acoustically by its normal (complex) surface impedance, and for computation of the transmitted field the required additional acoustical parameter is the propagation constant within the effective fluid. For a model of external reaction then computation of the reflected field requires knowledge of both surface impedance and propagation constant.

A model of the ground as supporting a single compressional wave type is consistent with propagation in a rigid porous medium in which the acoustic disturbance is transmitted only through the pore fluid and is attenuated by viscous and thermal effects. This model has been found adequate to represent the behaviour of porous boundaries in room and duct acoustics [4.1, 4.2] and in studies of outdoor sound propagation [4.3].

Indirect estimation of the surface impedance of any ground, that can
be modelled as locally reacting, is possible from a propagation
measurement with a fixed source-receiver geometry [4.3,4.4]. The
impedance values result from fitting the data on excess attenuation
between source and receiver after allowing for spherical divergence
air absorption. Since the surface impedance is complex, the fitting
procedure requires simultaneous variation of real and imaginary parts.
The questions arise (a) of a suitable initial guess and (b) of
suitable ranges and the type of relationship between real and
imaginary parts. Empirical formulae for impedance and propagation
constant in terms of a single parameter, the specific flow resistivity
of the porous medium [4.5], originally developed from acoustical
measurements on glass fiber materials, fix the frequency dependence of
the real and imaginary parts of the complex variables and the
relationship between them. They have been used to derive the
characteristics of ground surfaces needed for predictions of
propagation near to outdoor ground surfaces [4.4, 4.6, 4.7] in terms
of a best-fit flow resistivity. Although successful in some instances,
the empirical formulae have been shown to have shortcomings in this
application. These are evident particularly where measured values of
flow resistivity are available. In these circumstances the best-fit
value of flow resistivity has been found to be approximately half of the
mean measured value [4.4]. The large scatter in the deduced
impedance values with frequency, also obscures whether or not the
empirical formulae predict the correct frequency dependence. The

transmitted field, which is of particular interest in this report, depends upon the propagation constant. Although the empirical formulae include a set for real and imaginary parts of propagation constant, these have not been tested for soils and sands to the same extent as those for surface impedance. For these reasons the remainder of this chapter is devoted to the development of theoretically-based alternatives to the empirical formulae for the acoustical characteristics of rigid air-filled granular media and to a consequent examination of the limits of applicability of the empirical formulae. Comparison of the theoretical predictions and measured data are made for glass fibre materials, sands and soils.

4.2   The Modified - Raleigh Model

4.2.1.Introduction·

A comprehensive review of the available theories for propagation in porous media is given elsewhere [4.8]. In granular media the micro-structure is   best described in terms of grain shape size and packing density, all of which may be determined accurately by non-acoustic means.   However theoretical approaches which specify the form of the rigid solid constituent while attempting to describe the acoustic field in the fluid-filled interstices have been constrained in each case to particular grain shapes and find particular difficulties in describing the field near points of grain contact.   There is a further fundamental problem with such approaches, of course, where the rigid porous medium is consolidated such that individual solid elements cannot be identified. A conceptual model first suggested by Rayleigh, of a rigid solid matrix through which run parallel identical circular

cylindrical pores normal to the surface, has been shown capable of generalisation to many types of porous media [4.8]. The generalisation is achieved at the cost of introducing an adjustable parameter, the oscillatory-flow pore shape factor, which, strictly, is determinable only from best-fit to acoustical measurements. On the other hand, a suggested semi-empirical relationship between this parameter and another, the steady-flow pore shape factor, which is calculable for certain known pore geometries, means that, in principle, the acoustic properties of a rigid fluid-saturated granular medium can be deduced from four non-acoustic measurements. These are of flow resistivity, volume porosity, grain shape and mean grain diameter.

4.3. Propagation in a single pore

In this development, viscous and thermal effects are treated separately. Zwikker and Kosten [4.2] have shown that, at least in the limiting cases of low and high frequencies, such independent treatments give the correct result for the field within a cylindrical tube with rigid but heat-conducting walls containing a viscons, heat conducting fluid. Viscous effects may be imcorporated into a complex (i.e. frequency-dependent) density of fluid in the pore (ρ_c (ω)) subjected to an oscillatory disturbance with time-dependence exp($-i\omega t$), ω being the angular frequency. The result of analysis may be written [4.2] as

$$\rho_c (\omega) = \rho_0 [1 - 2 (\kappa_c \sqrt{T})^{-1} T (\kappa_c \sqrt{i})]^{-1} \quad (4.1)$$

where $T(\kappa_c \sqrt{i}) = J_1 (\kappa_c \sqrt{i}) / J_0 (\kappa_c \sqrt{i})$ $\quad (4.2)$

$J_0()$ and $J_1()$ being cylindrical Bessel functions of zeroth and first

order, respectively, and

$$\kappa_c = a \ (\omega/\nu)^{\frac{1}{2}} \qquad\qquad (4.3)$$

where a is the pore radius and ν is the Kinematic viscosity of the
fluid and ρ_0 is its equilibrium density.

In the context of developing a general theory for acoustic propagation in
fluid-saturated granular poro elastic media, Biot [4.10] considered
propagation in a paralled-sided infinite slit of semi-width b.
The expression for the complex fluid density in such a slit
corresponding to equation (4.1) may be deduced to be

$$\rho_s(\omega) = \rho_0 \{1 - [\kappa_s \ (-i)^{\frac{1}{2}}]^{-1} \ \tanh \ [\kappa_s(-i)^{\frac{1}{2}}]\}^{-1} \quad (4.4)$$

where $\qquad \kappa_s = b(\omega/\nu)^{\frac{1}{2}} \qquad\qquad\qquad (4.5)$

Analysis of the net flow of heat per unit mass within a circular
cylindrical tube containing a non viscous conducting fluid, supposing
(i) that heat is transported in transverse (radial) direction only and
(ii) that pressure is uniform over the pore cross section, produces
a relationship for the complex (frequency-dependent) compressibility
of the fluid within the pore, as follows [4.2];

$$C_c(\omega) = (\gamma \rho_0)^{-1} \ [1 + 2(\gamma - 1)T(N_{\rho r}^{\frac{1}{2}} \ \kappa_c \sqrt{i})] \quad (4.6)$$

where $\qquad N_{\rho r}$ is the Prandtl number and

$$C(\omega) = \frac{1}{P_0} \frac{dp}{d\rho} \qquad\qquad\qquad (4.7)$$

ρ and p being the time-dependent density and pressure respectively. A
similar analysis for net flow within a parallel-sides infinite slit of
thickness 2b produces [4.11]

$$C_s(w) = (\gamma P_0)^{-1} \left(1 + \frac{\gamma-1}{N_{pr}^{\frac{1}{2}} \kappa_s(-i)^{\frac{1}{2}}} \quad \tanh\left[N_{pr}^{\frac{1}{2}} k_s(-1)^{\frac{1}{2}}\right]\right) \qquad (4.8)$$

The functions for complex density for the fluid in the circular cylindrical tube and the parallel-sided slit have similar frequency dependence. The frequency dependence of the functions for complex compressibility are similar also. The real part of $\rho(\omega)$ and the imaginary part of $C(\omega)$ show very little frequency dependence for a wide range of κ. However the variations of imaginary part of $\rho(\omega)$ and the real part of $C(\omega)$ with κ show that

(i) $\mathrm{Im}\,\rho_s(\omega)$ for a slit of semi-width b $\approx \mathrm{Im}\,\rho_c(\omega)$ for a circular cylindrical tube of radius b/n

and (ii) $\mathrm{Re}\,C_s(\omega)$ for a slit of semi-width D $\approx \mathrm{Re}\,C_c(\omega)$ for a circular cylindrical tube of radius b/n.

The value of n for which these approximations hold is roughly constant and equal to 0.5 for $1.8 \leq \kappa_c \leq 10.66$ (see Table 4.1). This suggests that for a pore of a general shape but with a constant characteristic dimension ℓ along its length, it is possible to choose an equivalent radius a = ℓ/n and to evaluate $\rho(\kappa)$ and $C(\kappa)$ where $\kappa = (\ell/n)(\omega/\nu)^{\frac{1}{2}}$ (4.9). n represents an <u>oscillatory-flow pore-shape factor.</u>

4.2.3 Extension to bulk medium

If the pores in the bulk medium may be assumed identical and to run parallel to the surface then extension to the bulk medium from the expression for a single pore is straight forward and introduces the volume porosity and flow resistivity in addition to the single pore parameters

ℓ and n. In a real medium, for various reasons, including changing pore
orientation and cross section, the particle path lines will deviate from
the surface normal. The changing pore orientation is referred to as the
sinuosity or tortuosity, q, of the pore [4.2, 4.12, 4.13]. The tortuosity
factor q has the particular value $1/\cos \theta$ for a medium containing parallel-
cylindrical pores inclined at angle θ to the surface normal. It is
possible to incorporate a further factor (>1) when the pores have
cross-section which vary along their lengths. However this possibility
is not pursued further in the present analysis.

On the assumption that all of the pores are identical, the fluid velocity
averaged over a single pore's cross section, < v >, can be related to
the velocity u, averaged over unit cross-section of the porous medium by

$$< v > \; = q \, u \, / \Omega$$

where Ω is the volume porosity.

Consideration of the pressure gradient along a streamline in a
single pore during laminar flow gives [4.13]

$$- \frac{dp}{dx} = q^2 \, \phi_p \, \frac{u}{\Omega} \qquad (4.11)$$

ϕ_p, the flow resistance per unit length in a single pore, is given by

$$\phi_p = 8\mu s/\ell^2 \qquad (4.12)$$

where μ is the dunamic viscosity of the fluid, and s is a steady-flow
pore-shape factor. s may be calculated from a standard fluid-dynamical
analysis for a pore of any regular cross-section. For a circular-
cylindrical pore s has the value 1 and for a parallel sided slit

$s = 1.5$. A more extensive list of values of s corresponding to pores of various regular cross sections is given in ref [4.13].

From equations (4.11) and (4.12) the flow resistance per unit length, or flow resistivity of the porous medium, which is a measurable quantity, can be calculated from

$$\phi = 8\mu q^2 s / \ell^2 \Omega \qquad (4.13)$$

By eliminating the characteristic dimension ℓ between equations (4.9) and (4.13) it is possible to deduce that

$$\kappa = (s^{\frac{1}{2}}/n) (8\rho_0 q^2 \omega/\phi)^{\frac{1}{2}} \qquad (4.14)$$

for pores of arbitrary cross-section.

The one-dimensional equations of continuity and motion in the rigid porous medium which are sufficiently general if the medium is isotropic may be written [4.2] as

$$- \frac{\partial u}{\partial x} = \left(\frac{\Omega}{\rho_0}\right)\left(\frac{d\rho}{d\rho}\right)\left(\frac{\partial\rho}{\partial t}\right) \qquad (4.15)$$

and

$$- \frac{\partial \rho}{\partial x} = (q^2/\Omega)\, \rho\,(\omega)\, \frac{\partial u}{\partial t} \qquad (4.16)$$

Combining these equations with use of (4.7) enables production of the compressional wave equation inside the rigid porous medium.

$$\frac{\partial^2 \rho}{\partial x^2} = q^2 \rho\,(\omega)\, C(\omega)\, \frac{\partial^2 \rho}{\partial t^2} \qquad (4.17)$$

Finally from equations (4.1), (4.6) and (4.17) the propagation
constant k within the medium is given by

$$k^2 = q^2 (\omega/c_0)^2 \; [1 - 2 \, (k \sqrt{T})^{-1} \; T \, (k \sqrt{i}) \;]^{-1}$$

$$\times \; [1 + 2 \, (\gamma - 1)(N_{pr}^{\frac{1}{2}} \, k \sqrt{T})^{-1} \; T(N_{pr}^{\frac{1}{2}} \, k \sqrt{i})] \qquad (4.18)$$

and the relative surface impedance $Z/\rho c = 1/\beta$ which is the
characteristic impedance of a semi-infinite medium is given by

$$Z = \omega \rho \, (\omega)/k \qquad\qquad\qquad\qquad\qquad (4.19).$$

It is of particular interest to note that for low frequencies and
small values of the characteristic dimension, i.e. small pores or high
flow resistivity, equations (4.18) and (4.19) reduce to relatively
simple expressions by virtue of the small argument approximations of
the Bessel Functions. Hence, at low frequencies and for high flow
resistivities

$$Z/\rho_o c_o \approx k \approx (1 + i) \; (n^2 \Omega \phi \gamma \, \omega / (2\rho_o \, s c_o^2) \,)^{\frac{1}{2}} \quad (4.20)$$

4.2.4   Calculations of tortuosity

Tortuosity has an influence not only upon fluid-flow in porous media
but also upon their electrical conductivity when the pore space is
filled with an electrically conducting liquid and upon diffusion of water
vapour through the pore space. It has been related also to the index
of refraction of fourth sound when the porous medium is fixed with
liquid helium [4.14]. In the context of difusion of gases through
porous granular materials, the following relationship, known as
Bruggeman's relationship, has been found to hold [4.15],

$$q^2 = \Omega^{-n'} \qquad\qquad\qquad (4.21)$$

where n' is a grain shape factor taking the value 0.5 for
spherical grains. This and other values of n' are listed in Table
4.2. Hence knowledge of porosity and grain shape should be sufficient,
in principle, to calculate the appropriate tortuosity value. It should
be noted that for porosities near unity, the tortuosity will also be
near unity irrespective of particle shape.

4.2.5 Calculations of shape factors

For packings of spheres, of porosities in the range $0.34 < \Omega < 0.45$
CARMAN [4.13] gives a range of values of $2q^2s$,

$$4.5 < 2q^2s < 5.1$$

Using the Bruggeman relationship (4.21) for spheres, the stated range
of porosities implies a range of tortuosities given by

$$1.49 < q^2 < 1.715.$$

Hence from the range for $2q^2s$, it is possible to deduce $s \approx 1.5$ which
is the value for parallel-sided slit pores.

In principle it should be possible to deduce values of s for any
regular microstructure from an analysis of steady flow through the
known pore cross-section. n, the oscillatory-flow shape factor would
require computation from a separate analysis of the microvelocity field
for each pore cross-section. Nevertheless the values of n and s for
the supposed extremes of circular cylindrical tube and parallel-sided
slit suggest the possibility of the relationship

$$n = 2 - s \qquad\qquad (4.22)$$

Consequently for a packing of spheres, with s=1.5, it is possible to expect that n = 0.5.

For non-spherical and non-uniform particles appropriate values of n and s are more difficult to specify. Indirectly if the flow resistivity, porosity and mean grain shape are known then it may be possible to deduce a value for s, and hence n through equation (4.22), by utilising the concept of hydraulic radius.

Hydraulic radius, m is given by

$$m = \Omega/S \qquad (4.23)$$

Where S is the exposed particle surface area per unit volume of material. A more usual concept than flow resistivity in describing flow through porous media is permeability. As long as the pores have fairly smooth perimeters, the permeability B is related to m by

$$B = \Omega m^2 / (2q^2 s) \qquad (4.24)$$

Flow resistivity and permability are related through

$$B = \Omega^2/\phi \qquad (4.25)$$

Since m is calculated from geometrical considerations then knowledge of ϕ, Ω and n' should enable calculation of s.

4.3 Comparison of rigid porous model with reflection measurements

Although there are many measurements available in the literature

on the acoustical characteristics of materials of interest in room

acoustics and duct acoustics, there is a paucity of data for the acoustical

characteristics of soils and sands. An exhaustive set of data, on

various types of sand and artificial porous granular media

consisting of spherical lead shot, were obtained by Ferrero and

Sacerdote [4.15]. Their measurement technique involved measurement

of the pressure standing wave (plane wave fronts) formed in a

cylindrical tube with the sample forming one termination and the

loudspeaker source of pure tones forming the other. The propagation

constant and characteristic impedance were calculated from

measurements of surface impedance for two different thickness of

sample; one thickness being twice the other. This method was first

advocated by Pyett [4.16]. Ferrero and Sacerdote also measured the

porosities and flow resistivities of their samples. Thus for the

spherical lead shot and sand samples (n'=0.5) of all the parameters

are known, with the exception of the pore-shape factors for

application of the theory developed in earlier sections of this

chapter. The appropriate value of q^2 for all samples is approximately

1.6, since all $\Omega \approx 0.4$. Best agreement is obtained with the

po: shape factor ratio $n/\sqrt{s} = 0.5$ rather than 0.75 or 1. This value

corresponds approximately to n = 0.5, s = 1.5 i.e. the values for

parallel-sided slit pores as expected for packings of spheres (see

section 4.6). The measured data and theoretical predictions are

shown in Figures 4.1 to 4.5.
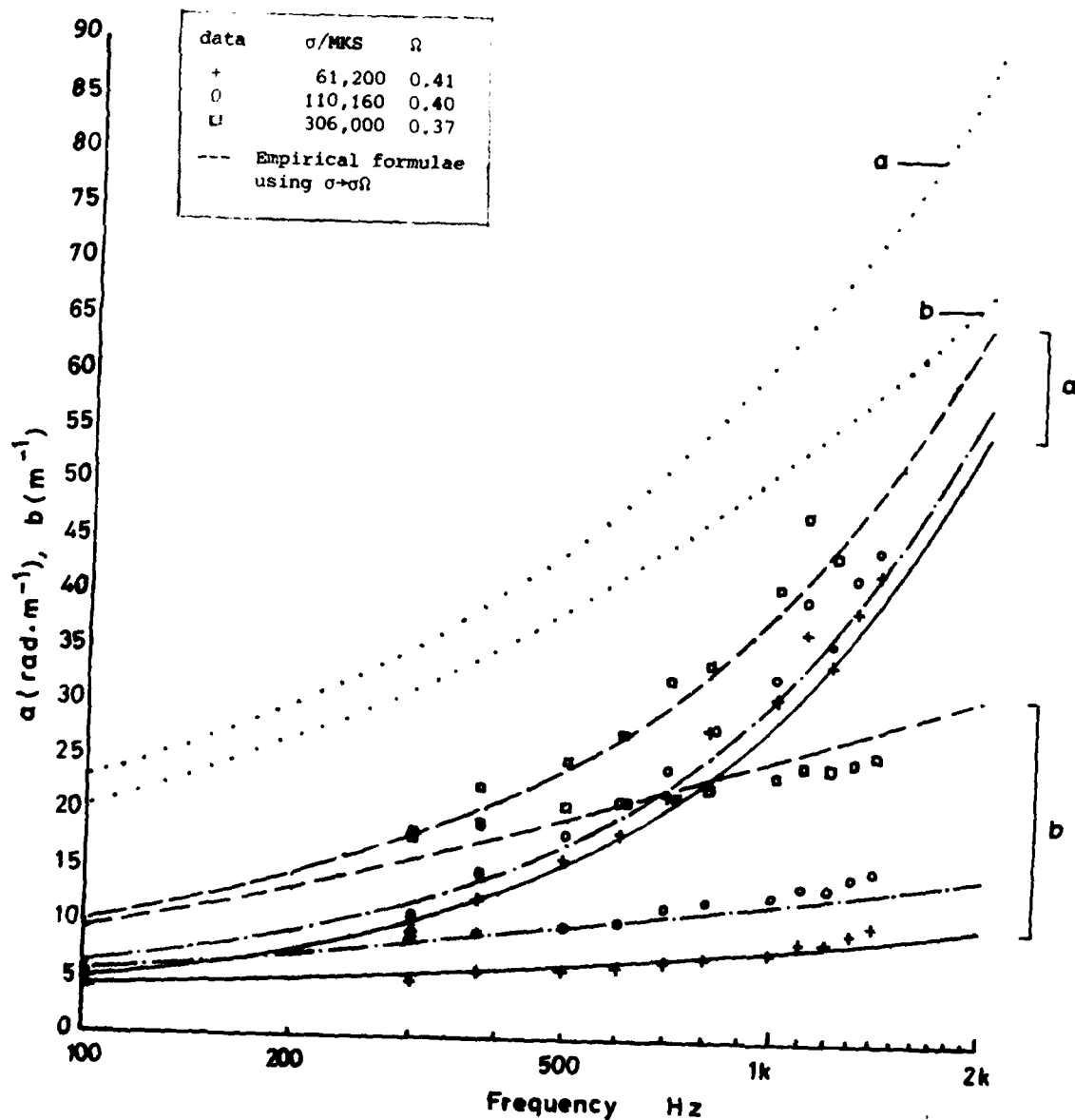
Figure 4.1 Comparison of measured data (+ 0 □) of propagation constants (a + ib) in sands, of measured flow resistivities and porosities as given in the key, with predictions based on these values and assumed values of n' = 0.5 and n/√a = 0.5
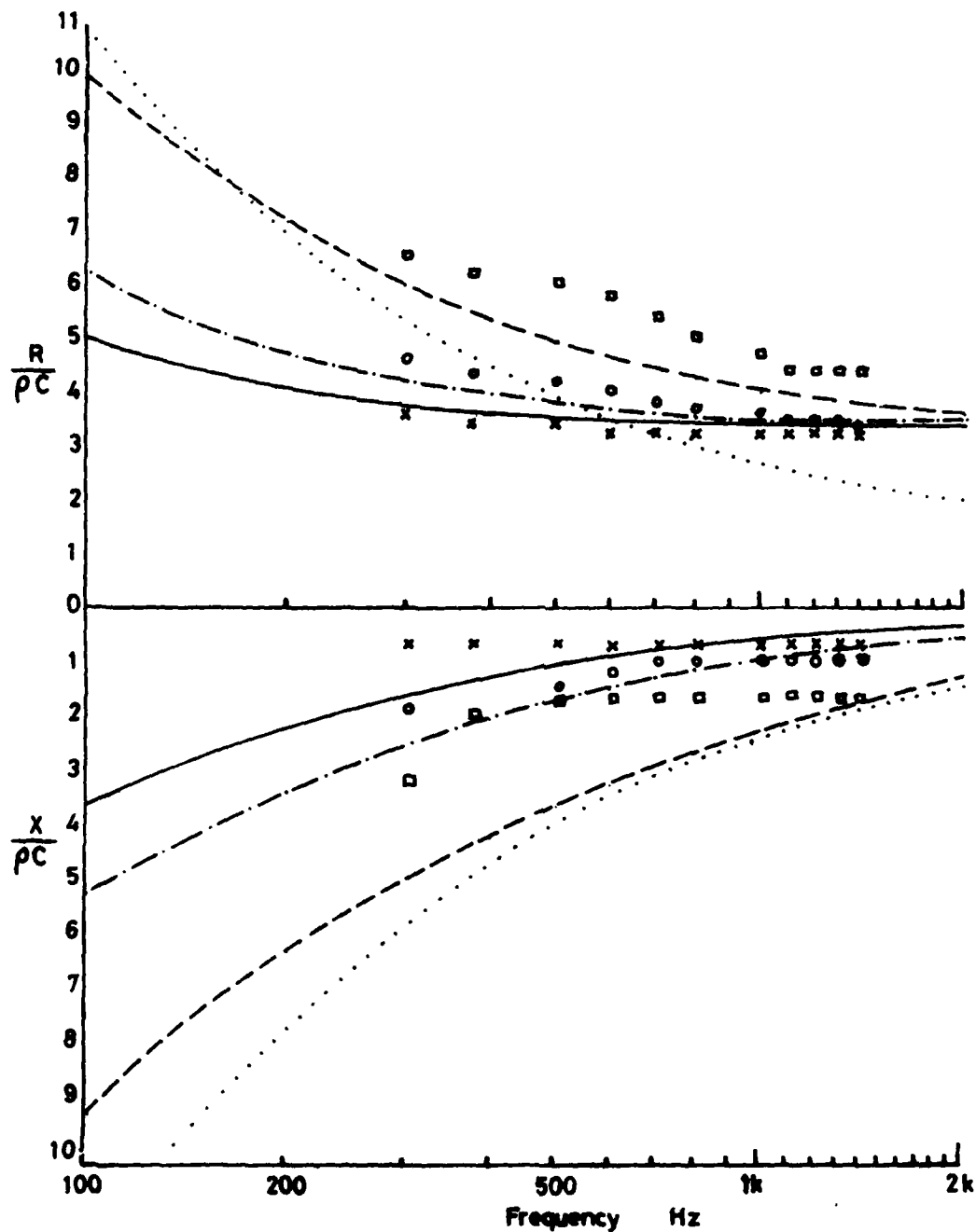
Figure 4.2 Comparison of measured data on characteristic independence (R + iX) of sand with predictions of rigid porous model. Key as in Figure 4.1.
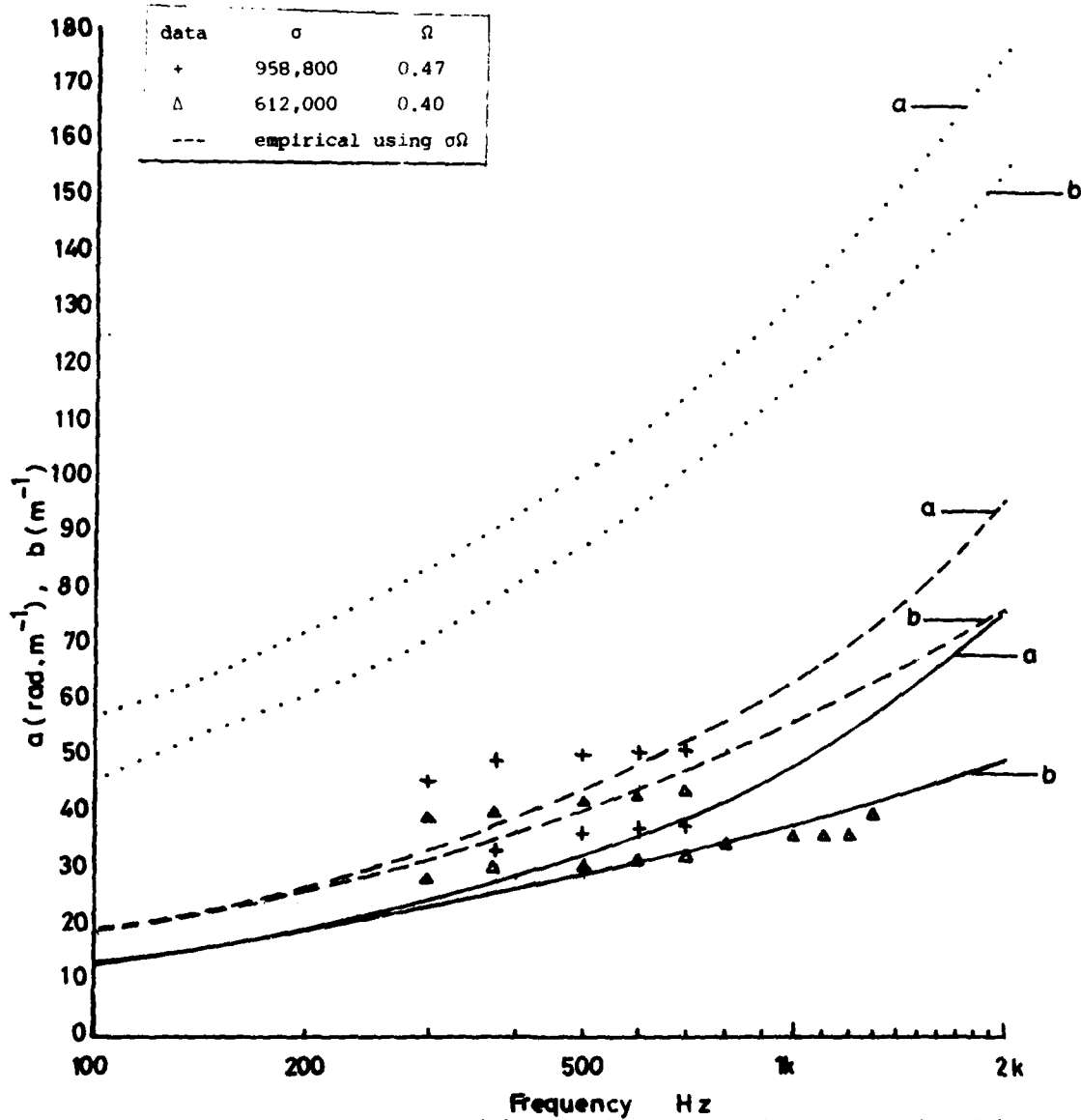
Figure 4.3 Comparison of measured data (+ Δ) on propagation constant (a + ib) in sands, having measured parameters as in the key above, with predictions based upon these parameters and n' = 0.5, n/√s = 0.5.
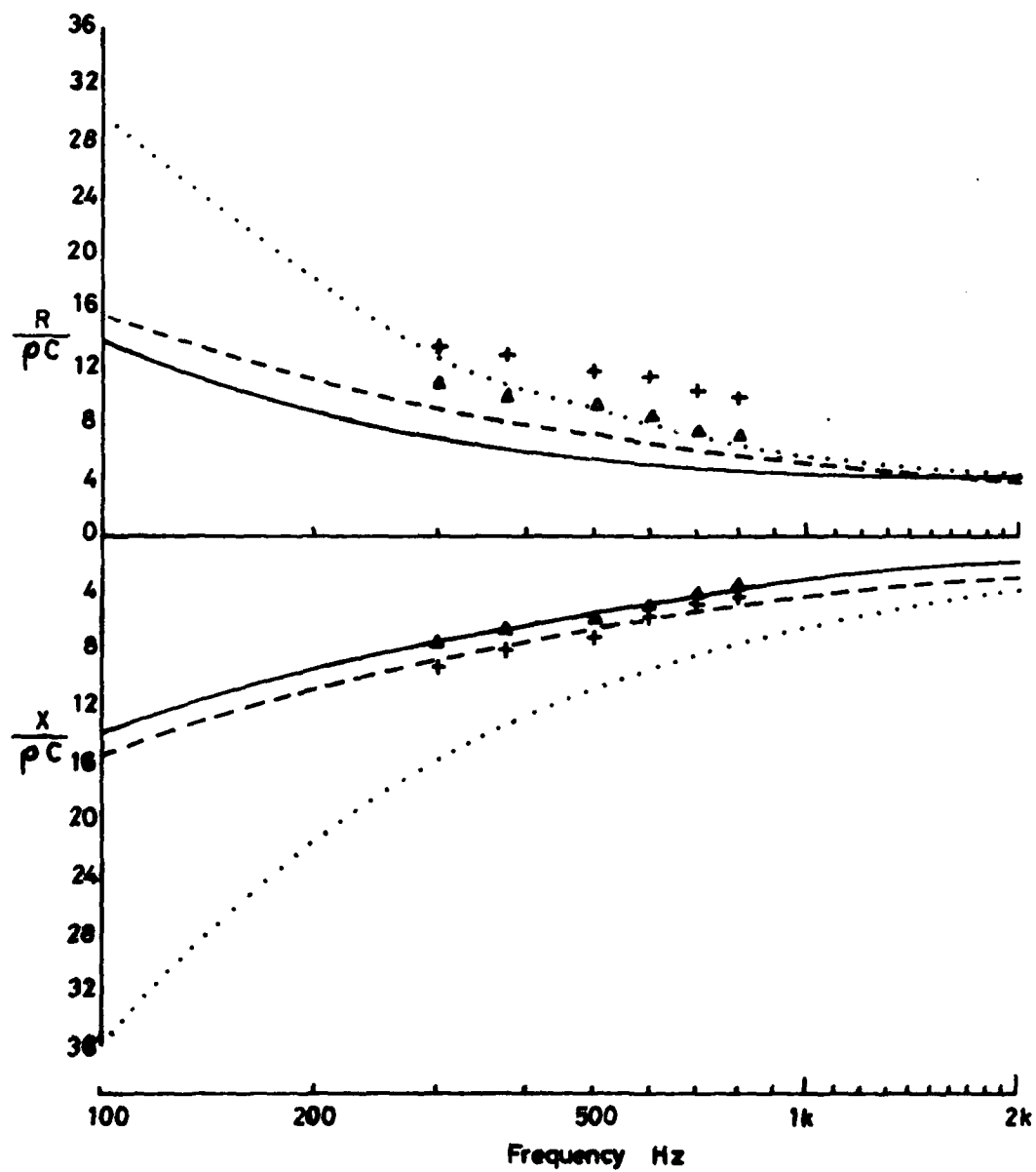
Figure 4.4   Comparison of measured data of the characteristic impedance (R + iX) of sands with predictions. Key as in Figure 4.3

4.8 Comparison with transmission measurements

4.8.1 Soils and sands

The difference in sound pressure levels between a microphone at the
surface and a probe microphone (Figure 4.5) at various depths in several
soils and sands has been measured [4.17]. Assuming that the ground medium
is locally reacting then this difference should be given by

$$\text{attenuation in dB} = 20 \ Im(k) \ D/\log_e 10$$

$Im(k)$ refers to the imaginary part of k, i.e. the attenuation constant,
and D is the depth of the probe. Figures 4.6 to 4.9 show the
comparison between the measured data and the predictions obtained
through (i) equation (4.19) (ii) measured values of flow resistivity,
using an apparatus described elsewhere [4.18]; and (iii) measured
values of porosity, deduced by weighing samples of known volume.

4.8.2 Fibreglass

Using the apparatus described in Chapter 3, measurements have been
made of the penetration of sound from an air-jet source into fibreglass
50 cm. thick. The probe receiver Microphone was at 1,4 and 7 cm.
beneath the surface. The comparison between measured one-third octave
averaged data and predictions based upon measured flow resistivity
(using apparatus conforming to ASTM) and the assumptions that

$$\Omega = q = n/\sqrt{s} = 1.$$

are shown in Figures 4.10 and 4.11. Note that the results on pulse
penetration (Figure 3.17) are consistent with the air-jet results and
with prediction. In the case of the loudspeaker generated narrow-band pulses
predictions of both the real and imaginary part of the transfer function
between surface and buried receivers (see sections 2.3 and chapter 3) are in
good agreement with measurement (Figures 4.12 to 4.14).
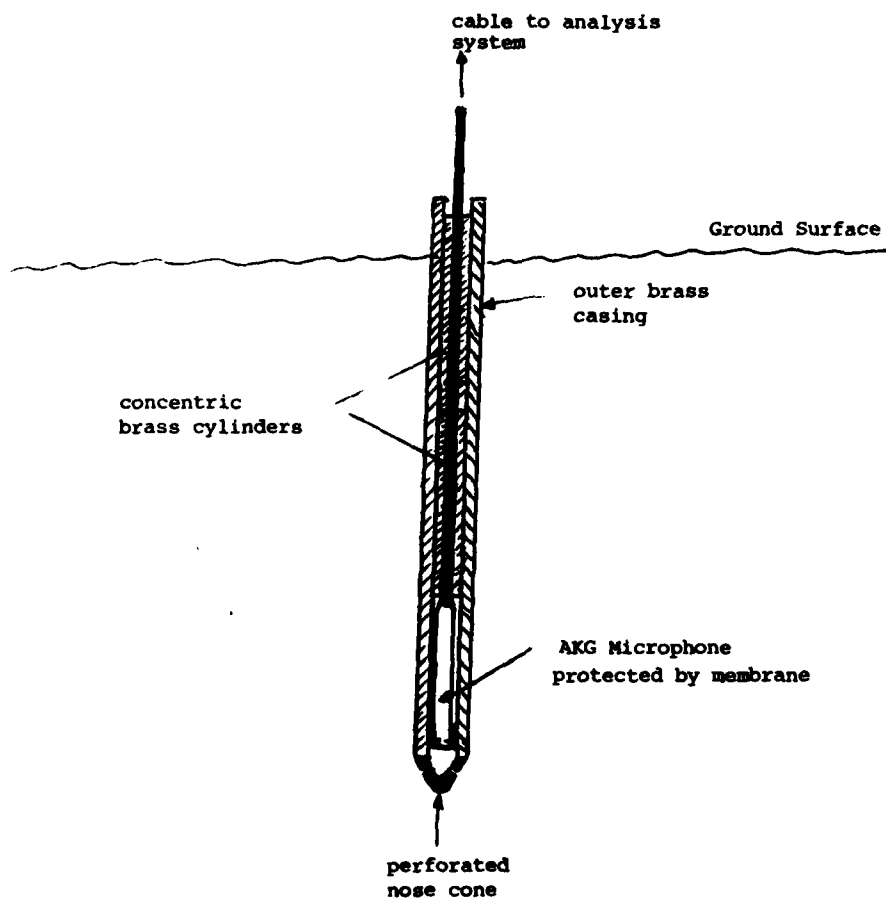
Figure 4.5   Microphone Probe System for soils and sands
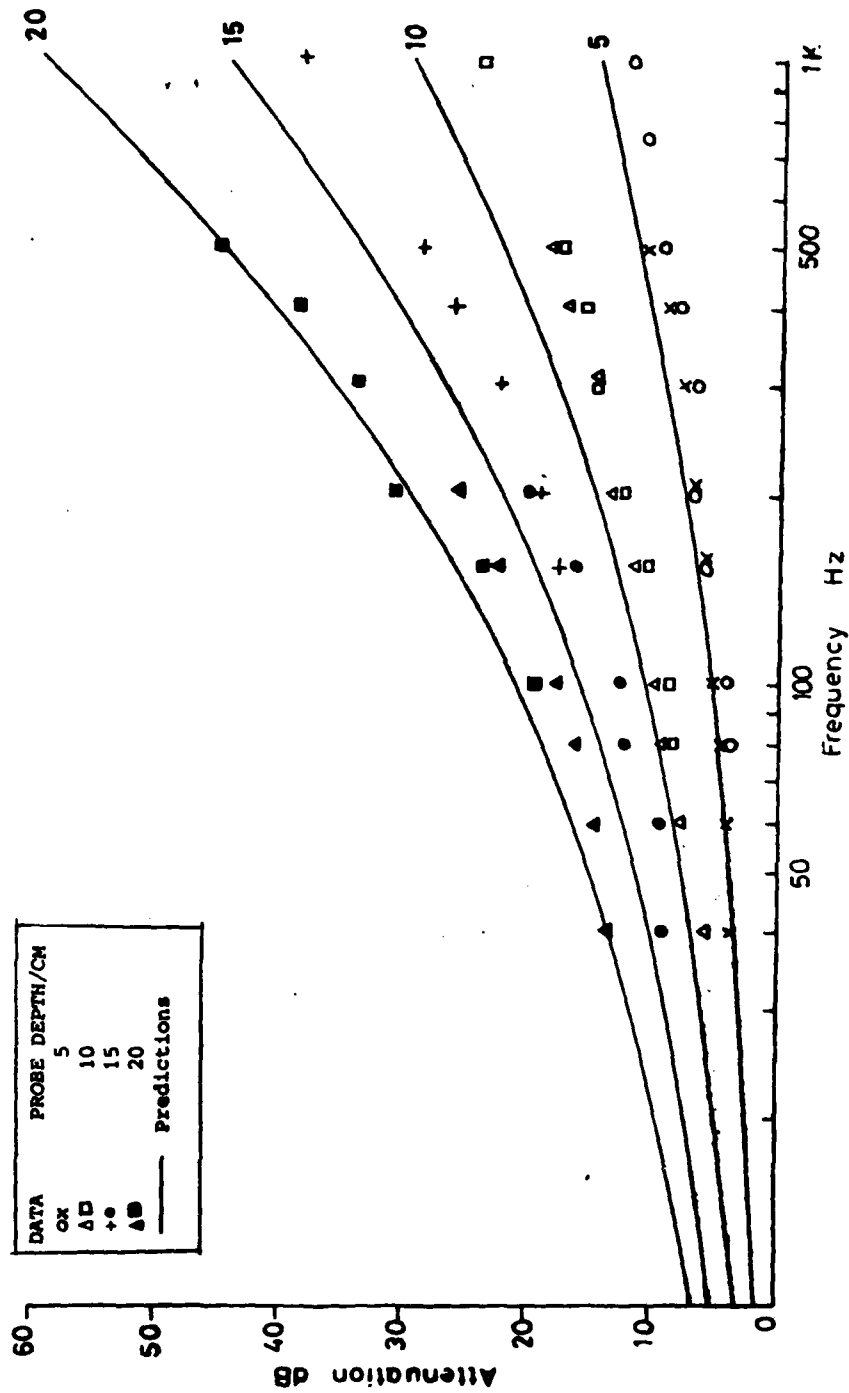
Figure 4.6   Measured attenuation in washed sand, σ = 210,000 MKS Units, = 0.4 (dry).
Predictions use these values, together with n' = 0.5, n/√s = 0.75

Figure 4.6   Measured attenuation in washed sand, σ = 210,000 MKS Units, = 0.4 (dry).
Predictions use these values, together with n' = 0.5, n/√s = 0.75
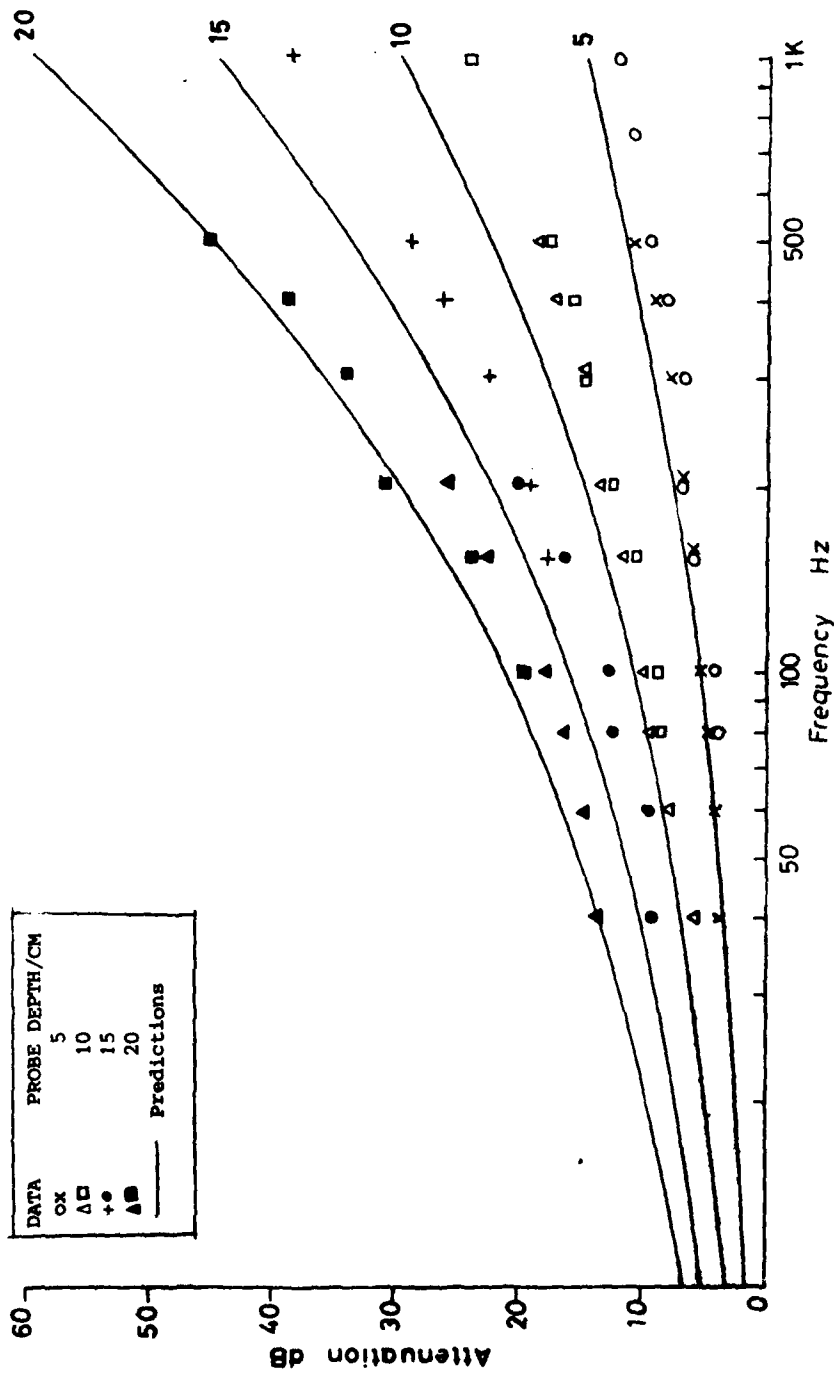
Figure 4.7   Measured attenuation in sand, σ = 450,000 MKS.   Predictions use this together with assumed = 0.4, n' = 0.5 and n'/s = 1.0
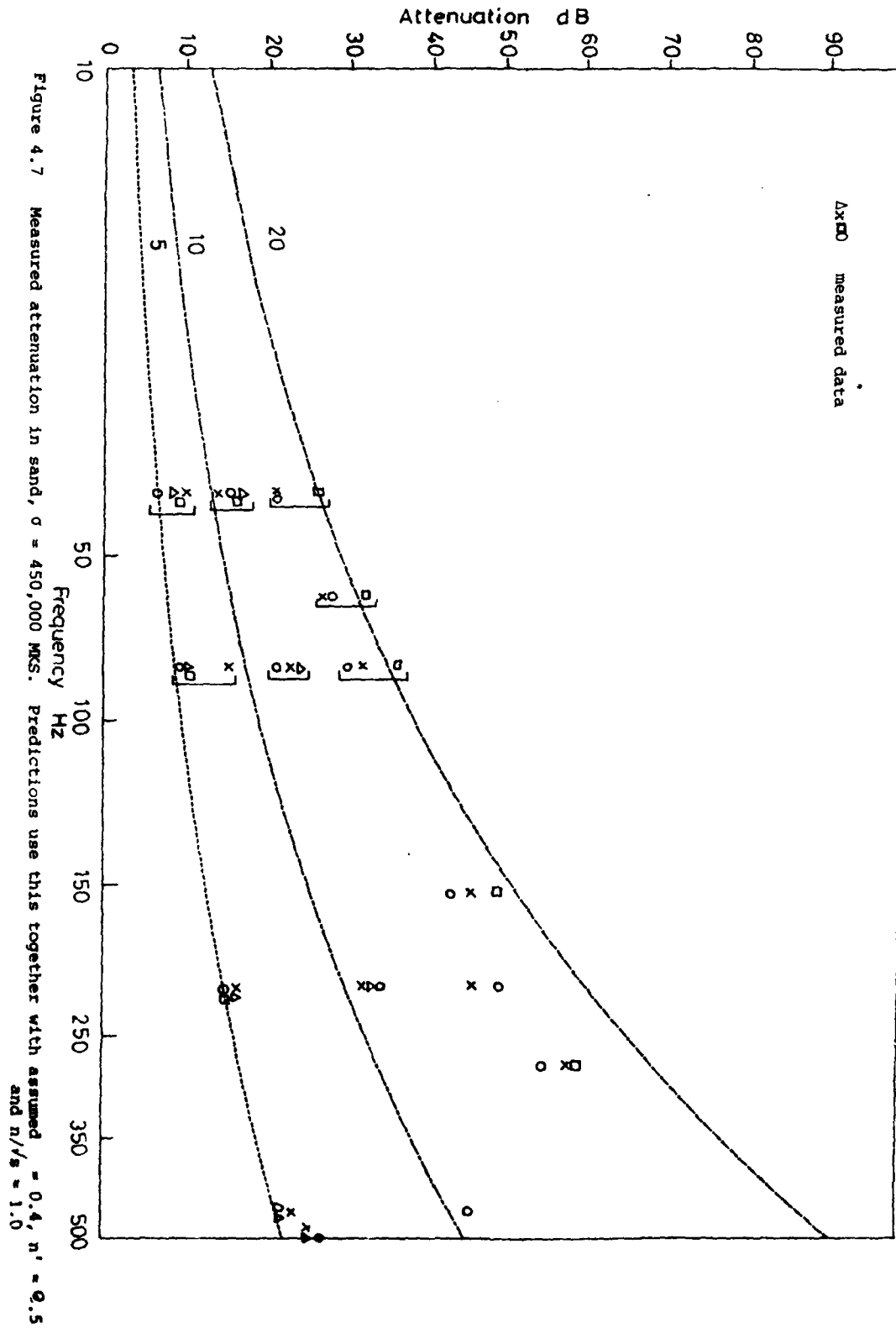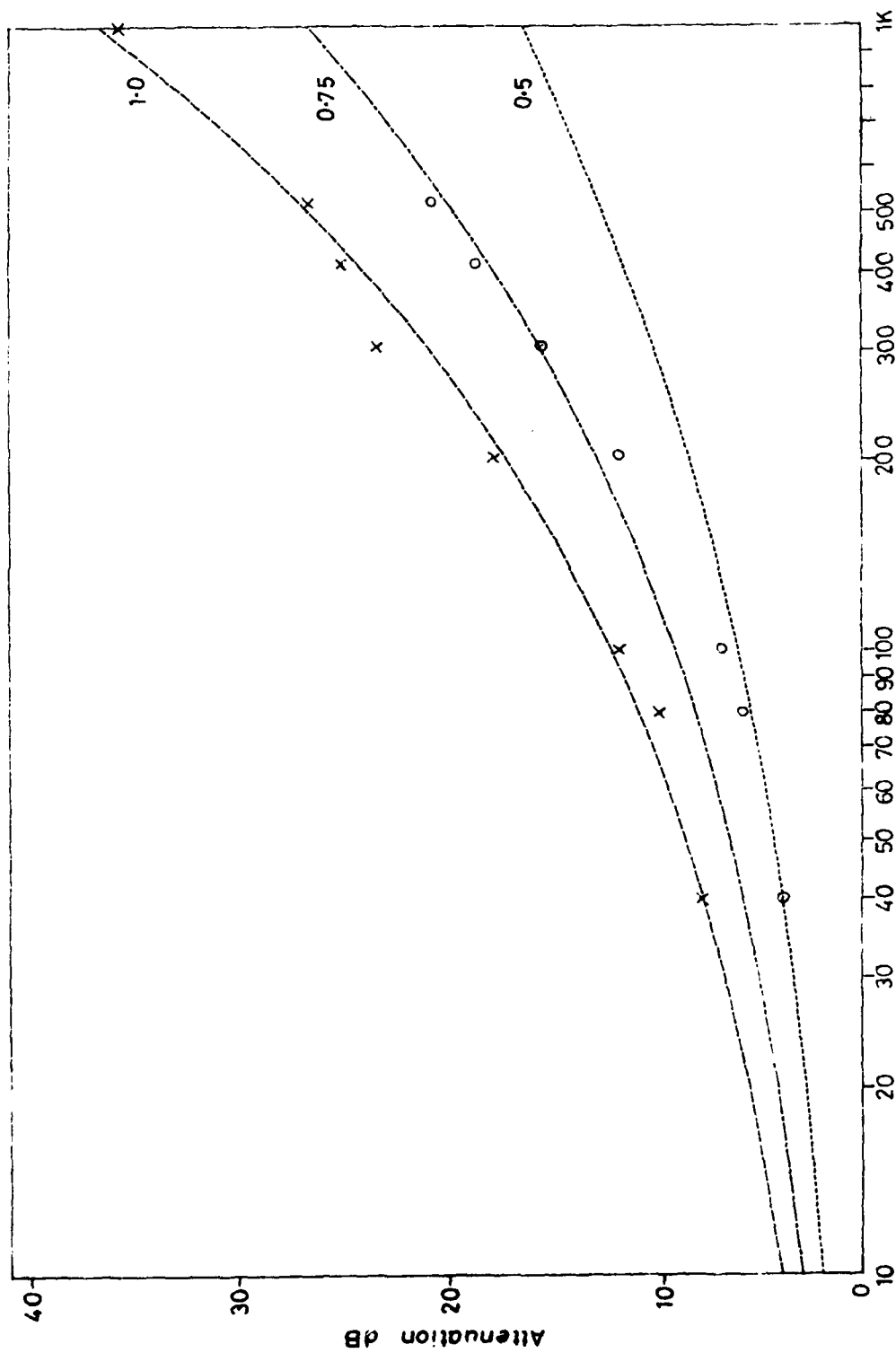
Figure 4.8   Measured attenuation in "institutional" soft $\sigma = 604,000$ MKS units.   Predictions use this value together with $\Omega = 0.4$, $n' = 1.0$ and labelled values of $n/\sqrt{s}$
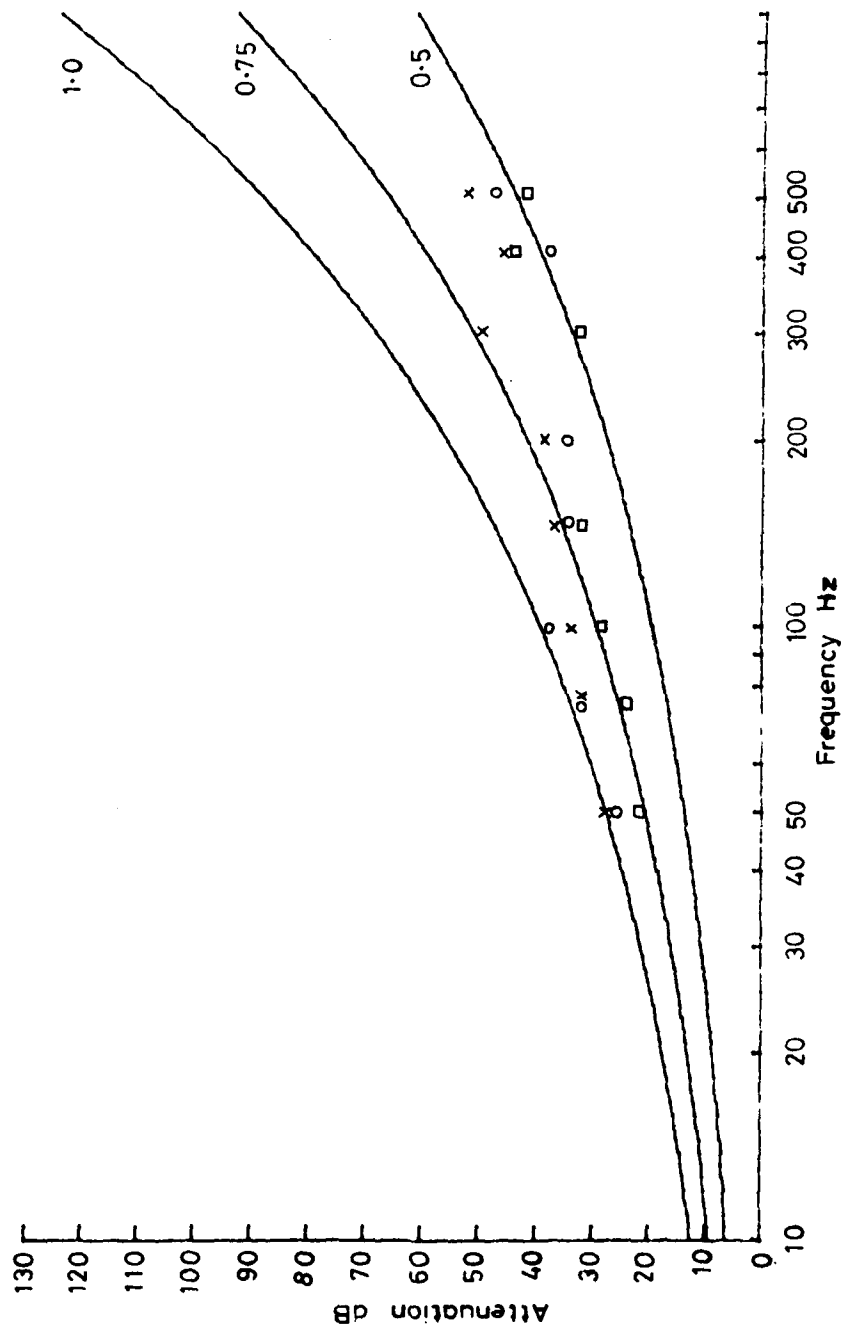
Figure 4.9 Measured attenuation in Loess, $\sigma = 650,000$ MKS units. Predictions use this value plus $\Omega = 0.4$, $n' = 1.0$ and labelled values of $n/\sqrt{s}$.

$$\frac{P(z_i)}{P(G)} \Big/ dB$$

Source height   0.1m

Separation   1m

Receiver depths 0.01,0.04,0.07m

Frequency HZ
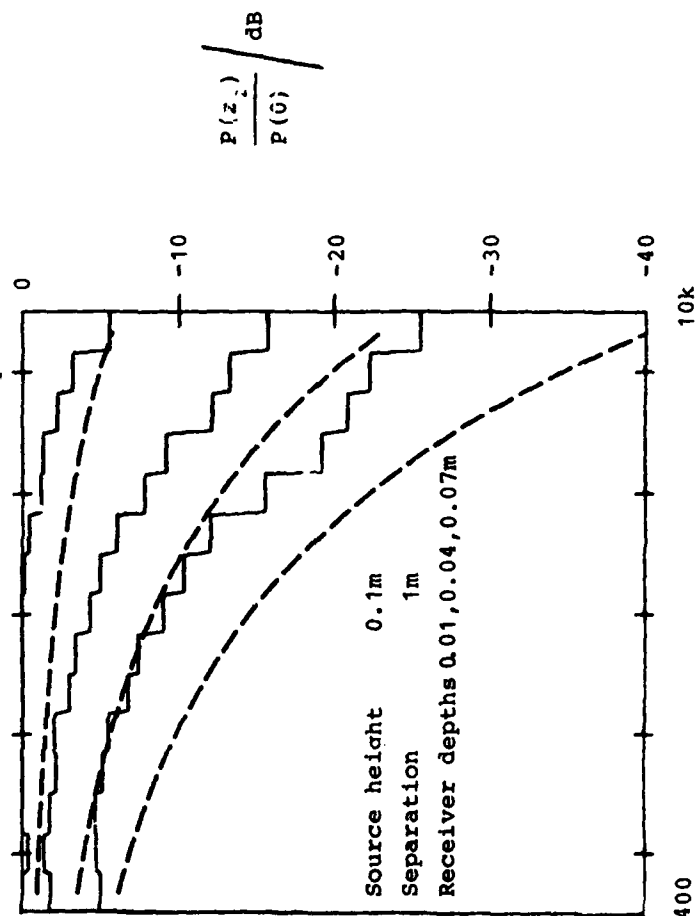
Figure 4.10   1/3 Octave Spectrum Ratio from Model measurements Fibreglass type:
Pilkington Crown 150 Fitted flow resistivity: 11460 (mks units)

Predictions are from empirical formulae
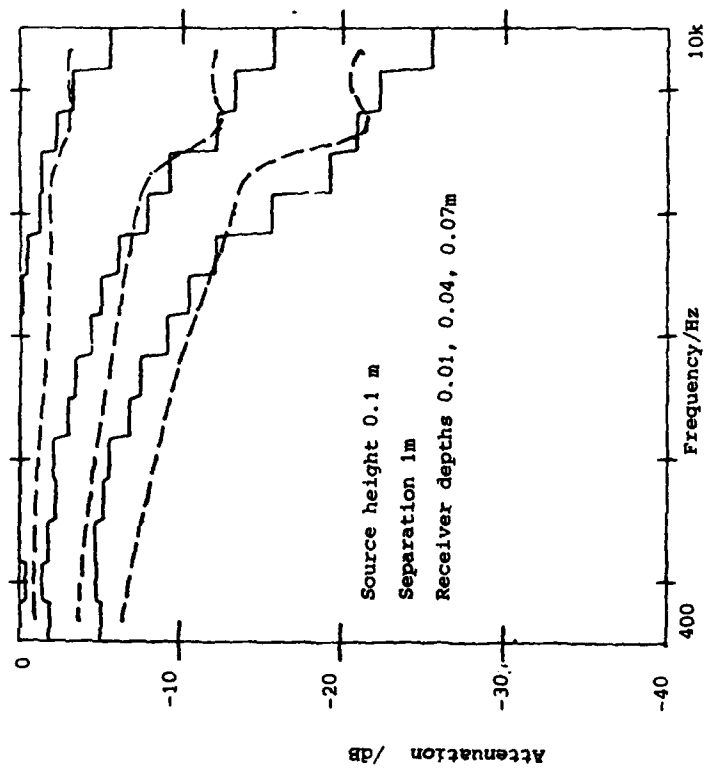
Figure 4.11 Measured $\frac{1}{3}$ octave attenuation in fibreglass of flow-resistivity

11,460 MKS units compared with predictions of rigid porous model $q = n/\sqrt{3} = 1$

Figure 4.12

COMPARISON OF MEASURED (———) AND PREDICTED (- - -) VARIATION WITH FREQUENCY OF THE TRANSFER FUNCTION BETWEEN 2 VERTICALLY SEPARATED MICROPHONES, ONE ON THE SURFACE AND ONE AT DEPTH 3 CM IN FIBRE GLASS.

PREDICTIONS BASED UPON FLOW RESISTIVITY = 11460 MKS RAYLS.m^{-1}, ASSUMED POROSITY = 1, TORTUOSITY = 1, SHAPE FACTOR = 1.

- 62 -
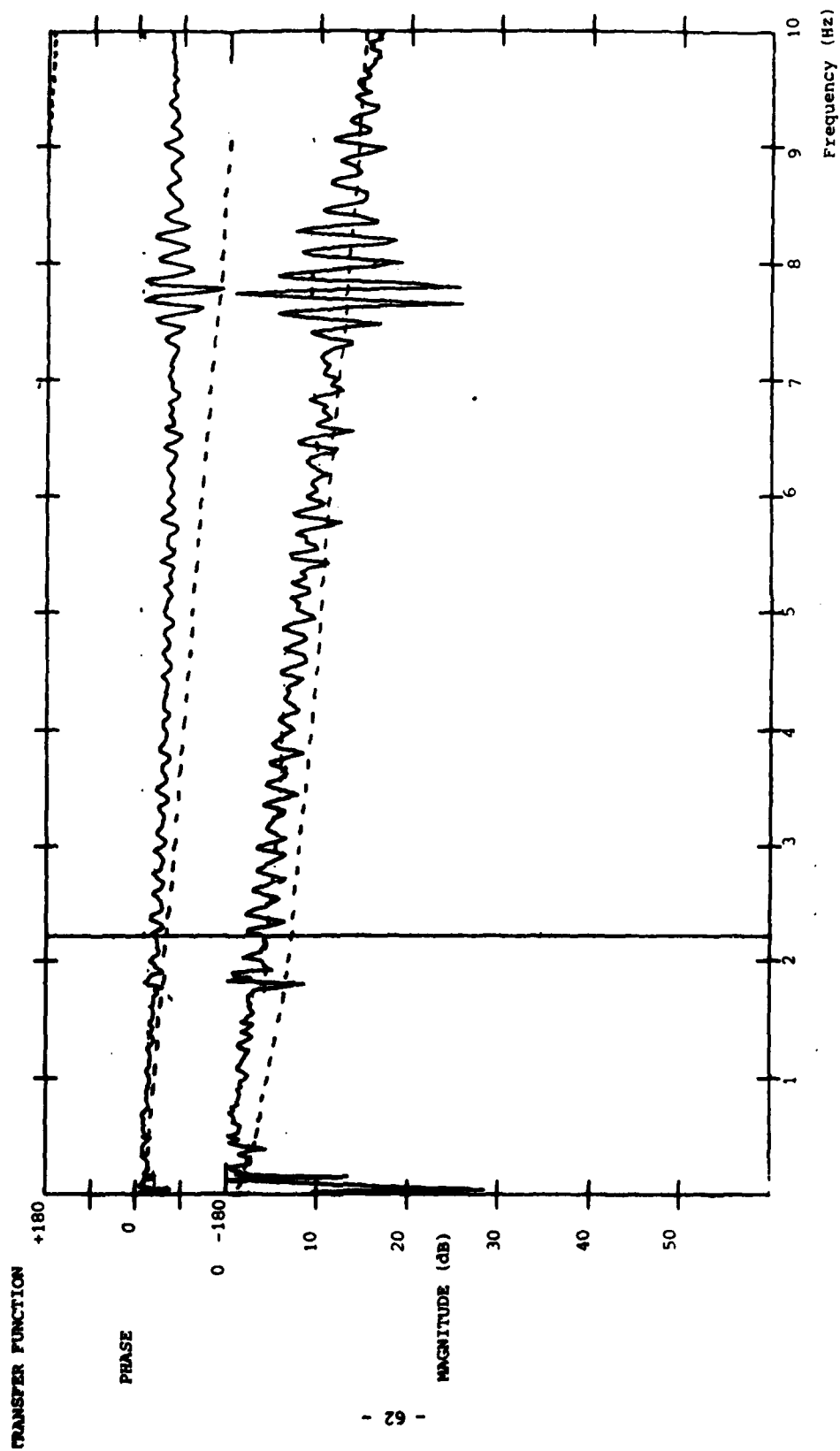
Figure 4.13

COMPARISON OF MEASURED (———) AND PREDICTED (— — —) VARIATION WITH FREQUENCY OF THE TRANSFER
FUNCTION BETWEEN 2 VERTICALLY SEPARATED MICROPHONES, ONE ON THE SURFACE AND ONE AT DEPTH 7CM
IN FIBRE GLASS. PREDICTIONS BASED UPON FLOW RESISTIVITY = 11,460 MKS RAYLS, ASSUMED POROSITY = 1,
TORTUOSITY = 1, AND SHAPE FACTOR RATIO = 1.
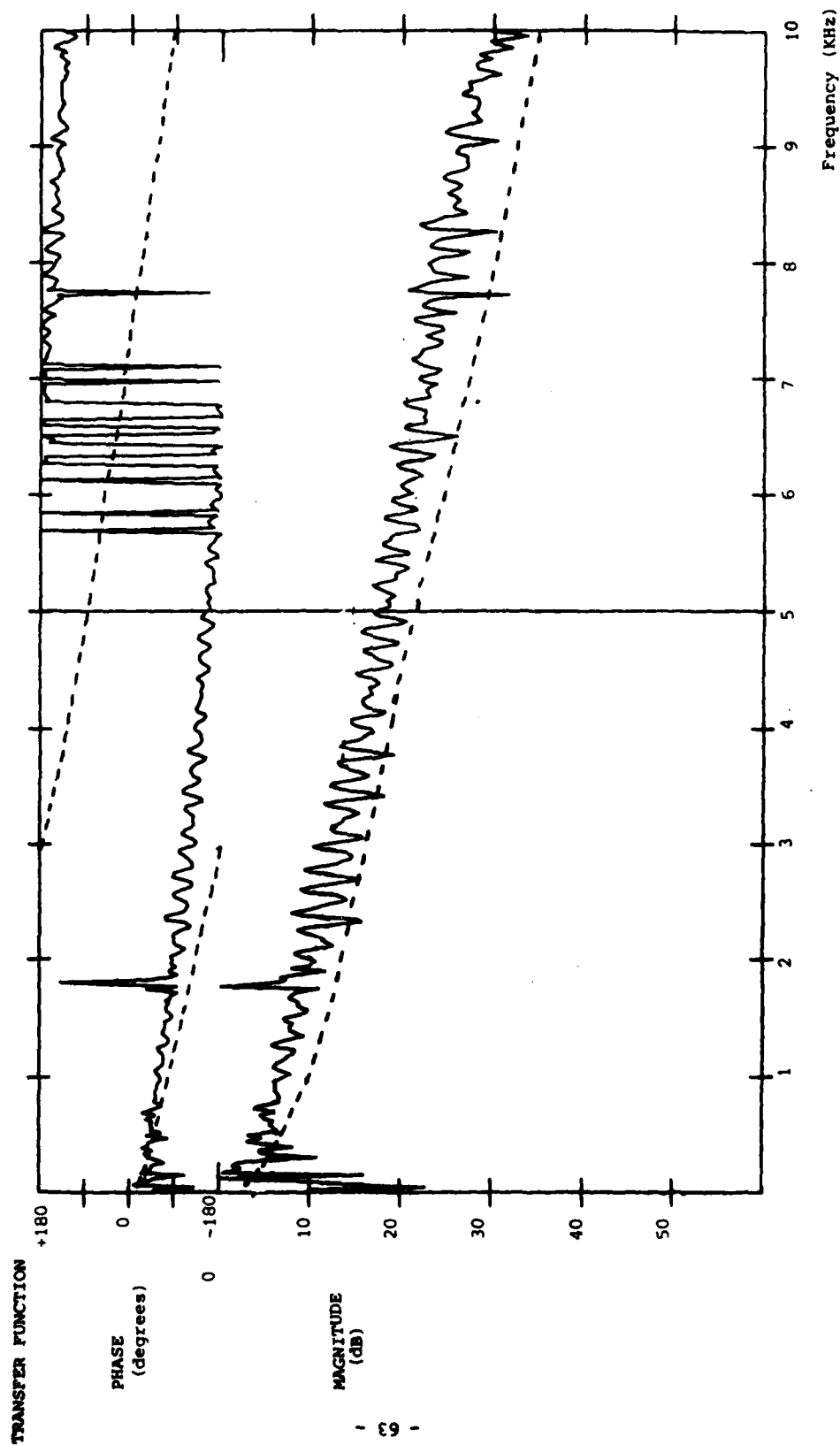
Figure 4.14

COMPARISON OF MEASURED (———) AND PREDICTED (— — —) VARIATION WITH FREQUENCY OF THE
TRANSFER FUNCTION BETWEEN 2VERTICALLY SEPARATED MICROPHONES, ONE ON THE SURFACE AND
ONE AT DEPTH 10CM, IN FIBRE GLASS. PREDICTIONS BASED UPON FLOW RESISTIVITY = 11460 MKS RAYLS.m^{-1},
ASSUMED POROSITY = 1, SHAPE FACTOR RATIO = 1 AND TORTUOSITY = 1.
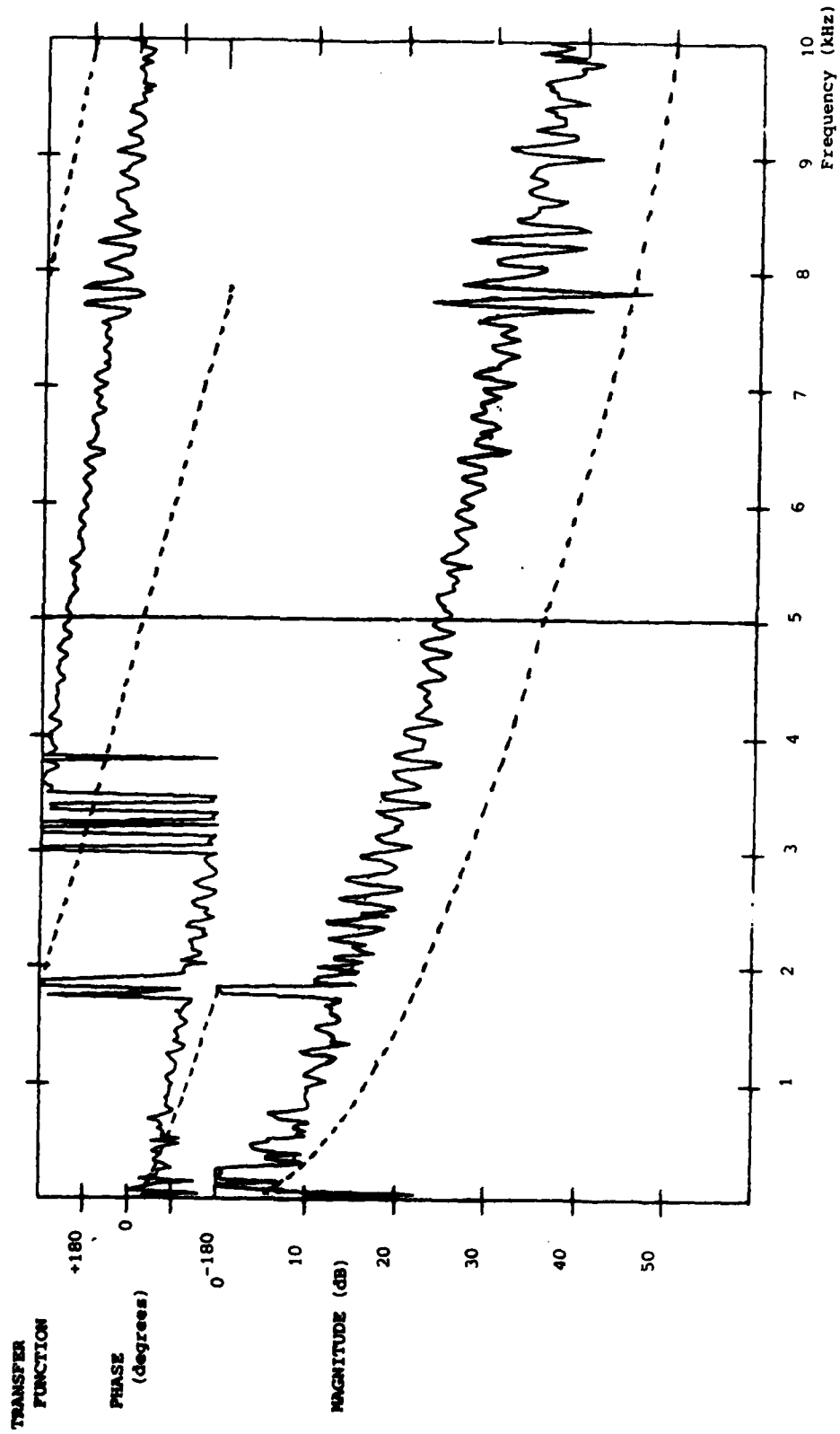
LITERATURE CITED

[4.1] R.A. Scott The Propagation of Sound in a Homogeneous
       Porous Medium Proc. Phys. Soc. London 58, 165 (1946)

[4.2] C. Zwikker and C.W. Kosten Sound Absorbing Materials
       (Elsevier, Amsterdam, 1949).

[4.3] T.F.W. Embleton, J.E. Piercy and N. Olson Propagation
       of sound in the Presence of a Finite Impedance Boundary
       J Acousr Soc. Am. 59 256-277 (1976)

[4.4] L.N. Bolen and H.E. Bass Effects of Ground Cover on the
       Propagation of Sound Through the Atmosphere   J Acoust.
       Soc. Am. 69 950-954 (1981)

[4.5] M.E. Delany and E.N. Bazley Acoustical Properties of
       Fibrous Materials Appl. Acoust. 3 105 (1970). See also
       NPL Aero Rept. AC71 (1971) by these authors

[4.6] J.E. Piercy and T.F.W. Embleton Excess Attenuation and
       Impedance of Common Ground Surfaces Characterised by Flow
       Resistance, paper presented at 50th ASA Meeting (June 1979)

[4.7] C.I. Chessell Meteorological and Ground Effects on the
       Propagation of Aircraft Noise Close to the Earth's Surface
       J. Sound Vib. 60 (2) 251-266 (1978)

[4.8]   K. Attenborough Acoustical Characteristics of Porous
        Materials Physics Reports 82, 3, 179-227 (1982)

[4.9]   K. Attenborough Acoustical Characteristics of rigid fibrous
        absorbents and granular materials 73 (3) 785-799 (1983)

[4.10] M.A. Biot Theory of Propagation of Elastic Waves in a
        Fluid-saturated Porous Solid J. Acoust. Soc. Am. 28 168-191(1956)

[4.11] A.R.P. Janse Sound Absorption at the Soil Surface (Centre for
        Agricultural Publishing and Documentation, Wageningen, The
        Netherlands, 1969) pp. 89-123

[4.12] P.G. Smith and R.A. Greenkorn Theory of Acoustical Wave
        Propagation in Porous Media J Acoust. Soc. Am. 52 247-253
        (1972)

[4.13] P.C. Carman Flow of Gases through Porous Media (Academic,
        New York, 1956)

[4.14] D.L. Johnson Equivalence between fourth sound in liquid
        He 11 at low temperatures and the Biot slow wave in
        consolidated porous media Applied Physics Letters 57 1065
        also D.L. Johnson; T.J. Plona; C. Scale, F. Fasierb and
        H. Kojima Tortuosity and Acoustic Slow Waves, Manuscript
        submitted to Phys. Rev. Lett.

[4.15] M.A. Ferrero and G.G. Sacerdote. Parameters of Sound Propagation
in Granular Absorbent Materials Acustica $\underline{1}$ 137-142 (1951)

[4.16] J.S. Pyett The acoustic impedance of a porous layer at
oblique incidence, Acustica $\underline{3}$ 375 (1953)

[4.17] K. Attenborough, H.E. Bass and L.N. Bolen Sound Transmission into
Plane Porous Ground Surfaces, Acoustics Letters $\underline{6}$ 6 87-90
(1982)

[4.18] H.E. Bass, L.N. Bolen, D. Cress, J. Lundien and M. Flohr
Coupling of Airborne Sound into the Earth: Frequency
Dependence J Acoust. Soc. Am. $\underline{67}$ 1502-1506 (1980).

5. GROUND AS A PORO-ELASTIC MEDIUM : RESPONSE TO PLANE WAVES

5.1 Biot theory and modification thereto

For a more complete description of ground response to an external acoustic disturbance it is necessary to model the ground as a poro-elastic medium.

We are concerned with the acoustic wave motion in ground, consisting of solid particles and air in the interconnected voids. The solid particles are assumed to be in firm contact with each other and thus constitute a homogeneous elastic frame. The theory of wave motion in such composite media, as derived by Biot [5.1], is widely applicable, and predicts two types of compressional waves and one shear wave.

In this section, we are interested in computing propagation constants for the above three types of body waves, suitable for numerical calculations and for parametric studies. For this purpose, it is convenient to express the equations of motion in terms of two scalar potentials ϕ_1 and ϕ_2 and two vector potentials $\underline{\psi_1}$ and $\underline{\psi_2}$. Let $\underline{u}$ and $\underline{U}$ describe the displacement of the skeletal frame and fluid respectively. Then displacement of the fluid relative to the frame is

$$\underline{w} = \Omega(\underline{u} - \underline{U})$$

Then we can express the two vectors as

$$\underline{u} = \nabla\phi_1 + \text{curl } \underline{\psi_1}$$

$$\underline{w} = \nabla\phi_2 + \text{curl } \underline{\psi_2}$$

The coupled equations of motion for the scalar potentials ϕ_1 and ϕ_2 are

$$H\nabla^2\phi_1 - C\nabla^2\phi_2 = \rho\ddot{\phi}_1 - \rho_f\ddot{\phi}_2$$

$$C\nabla^2\phi_1 - M\nabla^2\phi_2 = \rho_f\ddot{\phi}_1 - m\ddot{\phi}_2 - \frac{n}{k}\dot{\phi}_2 \qquad (5.1a)$$

and another pair of coupled equations of motion for the vector potentials $\underline{\psi}_1$ and $\underline{\psi}_2$

$$G_b\nabla^2\underline{\psi}_1 = \rho\ddot{\underline{\psi}}_1 - \rho_f\ddot{\underline{\psi}}_2$$

$$\frac{n}{k}\dot{\underline{\psi}}_2 = \rho_f\ddot{\underline{\psi}}_1 - m\ddot{\underline{\psi}}_2 \qquad (5.1b)$$

where H,C and M are elastic constants expressed in terms of elastic moduli of the grain-solid, fluid and frame.

$$H = (K_r - K_b)^2 / (D - K_b) + K_b + 4G_b/3$$

$$C = K_r (K_r - K_b) / (D - K_b)$$

$$M = K_r^2 / (D - K_b)$$

and

$$D = K_r [1 + \Omega(K_r/K_f - 1)] \qquad (5.2)$$

K_r is the bulk modulus of the individual grains, K_f is the bulk modulus of the pore fluid, G_b is the shear modulus and K_b is the bulk modulus of the assemblage of particles. In Eq. (5.1), ρ is the average mass density, ρ_f is the fluid density, n is the dynamic viscosity coefficient and k is the permeability of the porous frame with dimensions $[L]^2$.

The parameter m, related to the fluid motion, is sometimes called effective fluid density and is given by

$$m = q^2 \rho_f / \Omega$$

where Ω is porosity and q is tortuosity. The parameter q (> 1) accounts for the fact that the fluid flow is not in the direction of macroscopic pressure gradient. Experimentally measured values of q for soils and sand have been reported in literature [5.2]. However in the present study, we use q as a model parameter through the relation

$$q = \Omega^{-n'}$$

where n' is a grain shape factor obtained from studies of gas and solute diffusion.

In the high frequency range, where the visosity effects begin to be of important, we replace the ratio $\frac{\eta}{k}$ by $\eta \, F(\lambda)/k$ where $F(\lambda)$ is a complex viscosity correction factor, given by

$$F(\lambda) = (- 1/4) \frac{\lambda \sqrt{\iota} \; T(\lambda\sqrt{\iota})}{[1 - 2.0 \; T(\lambda\sqrt{\iota})/(\lambda\sqrt{\iota})]}$$

and

$$\lambda = (\sqrt{s}/n) \; \sqrt{8q^2 \Omega k \omega / \mu}$$

(5.3)

where μ is kinematic viscosity $(n/\sqrt{s})$ is identified as a single model

parameter, i.e. shape factor ratio. Note that , from equation (4.1),

the complex density of fluid in the pores of a rigid fluid-saturated porous

medium may be written

$$\rho(\lambda) = -4F(\lambda) \ / \ (\lambda\sqrt{i})\Gamma'(\lambda\sqrt{i})]$$

We seek solutions of the form

$$\phi_1 = A_1 \exp[i(\ell x - \omega t)]$$

and

$$\phi_2 = A_2 \exp[i(\ell x - \omega t)]$$

and Eqs. (5.1) provide a pair of simultaneous equations for A_1 and A_2.

For a non-zero solution, we require that the determinant should vanish

and hence we obtain

$$\begin{vmatrix} \rho\omega^2 - H\ell^2 & c\ell^2 - \rho_f\omega^2 \\ \\ \rho_f\omega^2 - C\ell^2 & M\ell^2 - m\omega^2 + i\omega F(\lambda)\eta/k \end{vmatrix} = 0$$

The above equation is quadratic in ℓ^2 and has two distinct roots

$$\ell^2 = [-B \pm \sqrt{B^2 - 4AC]} \ / \ 2A$$

as long as $B^2 - 4AC \neq 0.$

where

$$A = C^2 - HM$$

$$B = \omega^2 \{mH - 2C\rho_f + \rho M\} - i\omega F(\lambda)\eta H/k$$

$$C = \omega^4 \{\rho_f^2 - m\rho\} + \omega^2 \{i\rho\omega F(\lambda)\eta/k\} \qquad (5.6)$$

The two roots of ℓ^2 as given by (5.6) correspond to "fast" and "slow" types of compressional waves. The corresponding propagation constant for shear wave motion can be obtained by assuming

$$\psi_1 = B \exp[i(\ell x - \omega t)], \quad \psi_2 = B_2 \exp[i(\ell x - \omega t)] \qquad (5.7)$$

Then it follows from the equations of motion (5.1b)

$$\begin{vmatrix} \rho\omega^2 - G_b\ell^2 & \rho_f\omega^2 \\ \rho_f\omega^2 & m\omega^2 + i\omega F(\lambda)\eta/k \end{vmatrix} = 0 \qquad (5.8)$$

The phase velocity, ω' Re ℓ and attenuation, Im ℓ of three types of waves can be easily computed from (5.6) and (5.8). A FORTRAN program has been written to compute propagation constants for two dilatational waves and one shear wave. The complex frequency correction factor $F(\lambda)$ has been computed using Bessel functions of complex arguments where the calculations are performed in single precision.

The pore parameter λ as given in Eq.(5.3) enables us to consider the influence of various parameter on phase velocity and attenuation of fast and slow compressional wave modes. For the present, we restrict the sensitivity analysis only to the parameters relating to the micro structure and assume base values for the elastic constants of the frame which are typical of sand.

A few remarks concerning the microstructural parameters are in order. We have already note that the tortuosity is dependent on porosity and this gives us two independent parameters n' and Ω . Although permeability k and shape factor ratio are related, in the present study we treat them as another pair of independent parameters. Thus we choose the four parameters Ω, n', k and $n/\sqrt{s}$ to describe the microstructure of the ground. (For a more detailed discussions on this see references [5.3]).

5.2   Predictions of wave speeds and dispersion in air and water saturated sand.

The program described in previous section has been utilized to compute

phase velocity and attenuation in water filled saturated sediments [5.3]

where the values assumed for the various parameters used in the

computation are listed in Table 1. Here we present, in Figures 5.1 to

5.4 a sensitivity analysis of dispersion and frequency -dependent viscous

attenuation (fast wave) to porosity (0.3), grain shape factor (n' = 1.25)

permeability ($10^{-7}cm^2$) and shape factor ratio (0.6). The values given

in the brackets refer to base values.

The sensitivity of attenuation to permeability, shape factor ratio

and grain shape factor are similar to those obtained for variations

in permeability and pore size parameter and for structure factor

respectively by Stoll and Bryan [5.4]. Viscous attenuation appears to

be more sensitive to porosity as it affects tortuosity (structure factor).

TABLE 1

PARAMETER	VALUE	UNITS
ρ_r	2.65	g/cm^3
K_r	3.6×10^{11}	dyn/cm^2
ρ_f	1.0	g/cm^3
η	0.01	$dyn - sec/cm^2$
G_b	8.27×10^9	dyn/cm^2
K_b	1.38×10^{10}	dyn/cm^2

Attenuation (Nepers/m)

0.7

0.3

Frequency (Hz)

Phase Velocity (m/Sec)

0.7

0.6

0.5

0.4

0.3
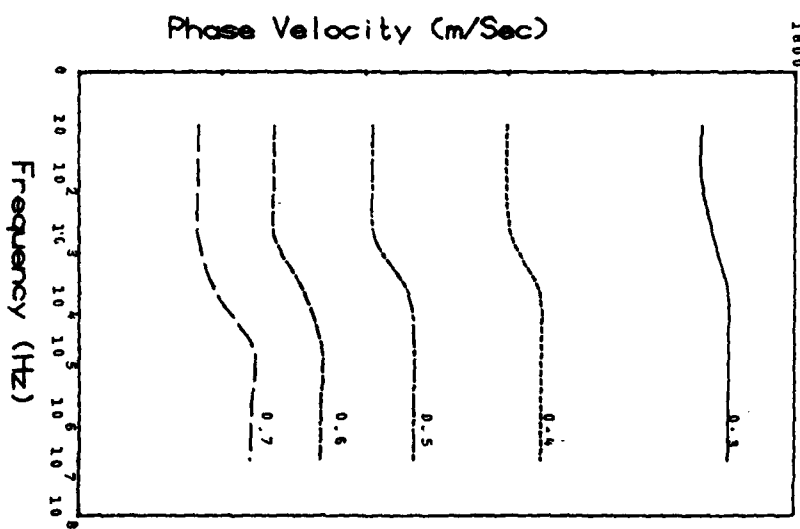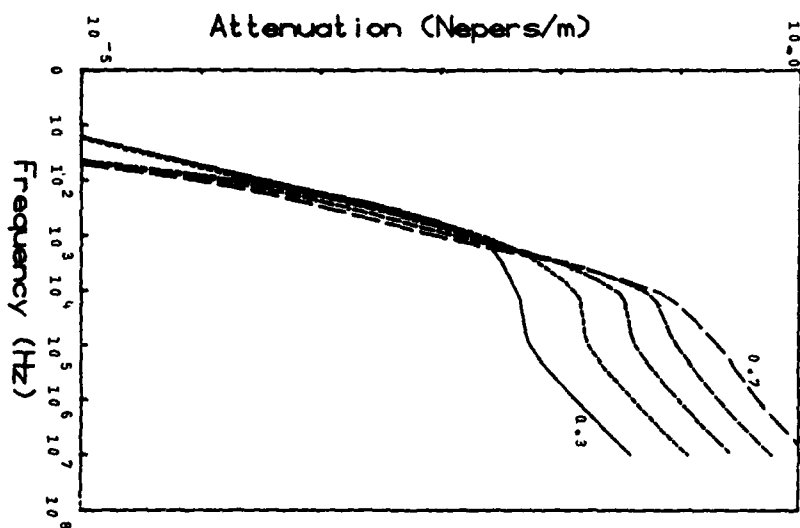
Frequency (Hz)

Figure 5.1 Sensitivity of predicted fast wave attenuation and phase velocity versus frequency characteristics in water-saturated sand to variation in porosity over the range $0.3 < n < 0.7$.

FAST WAVE

Attenuation (Nepers/m)

Phase Velocity (m/Sec)
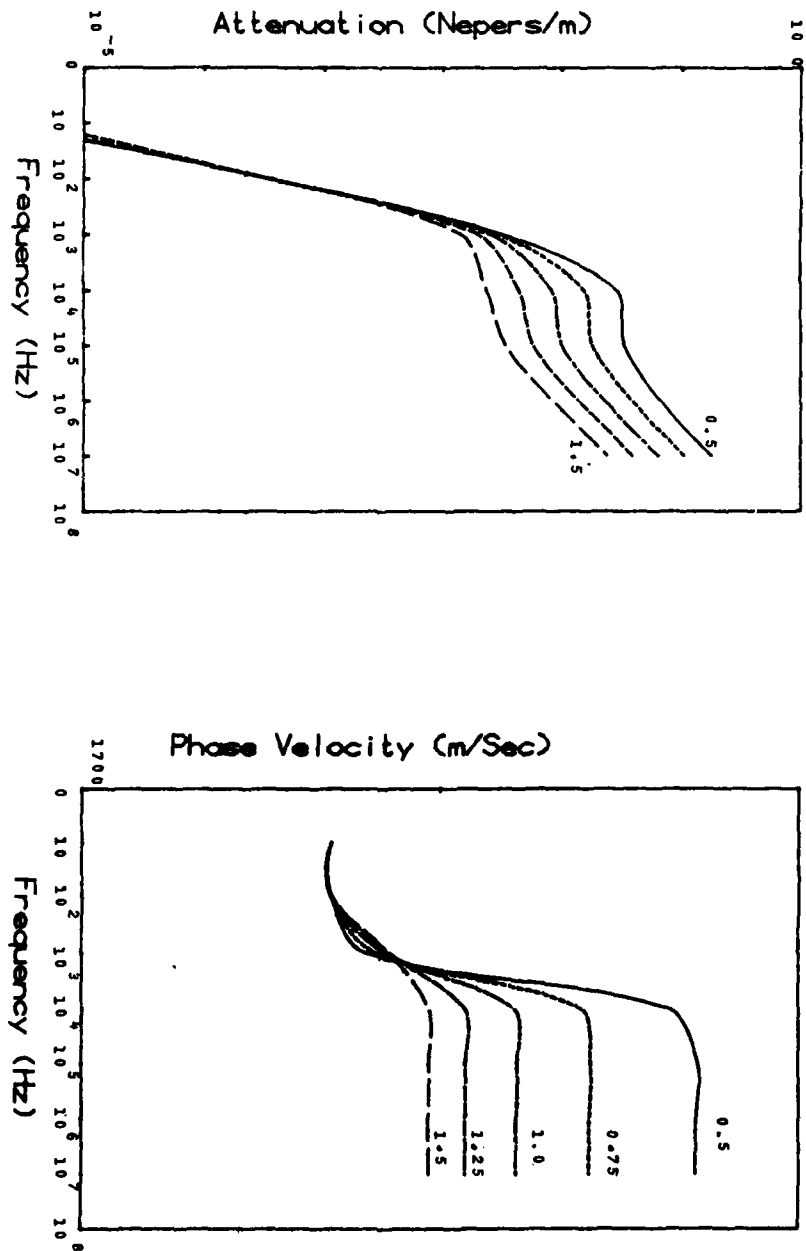
Figure 5.2   Sensitivity of predicted fast wave characteristics in water-saturated sand to variation in grain shape factor.
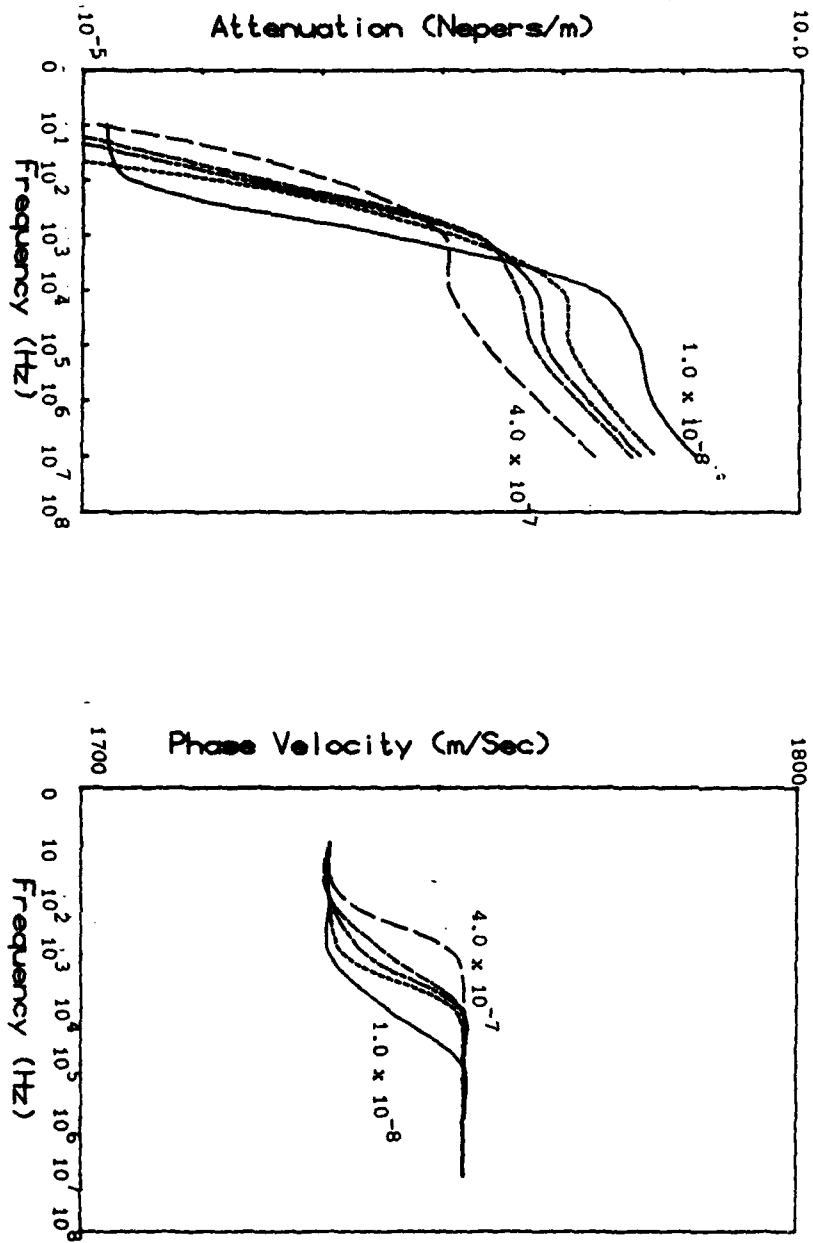
Figure 5.3   Sensitivity of predicted fast wave characteristics in water-saturated sand to variation in permeability.

Attenuation (Nepers/m)

Phase Velocity (m/Sec)
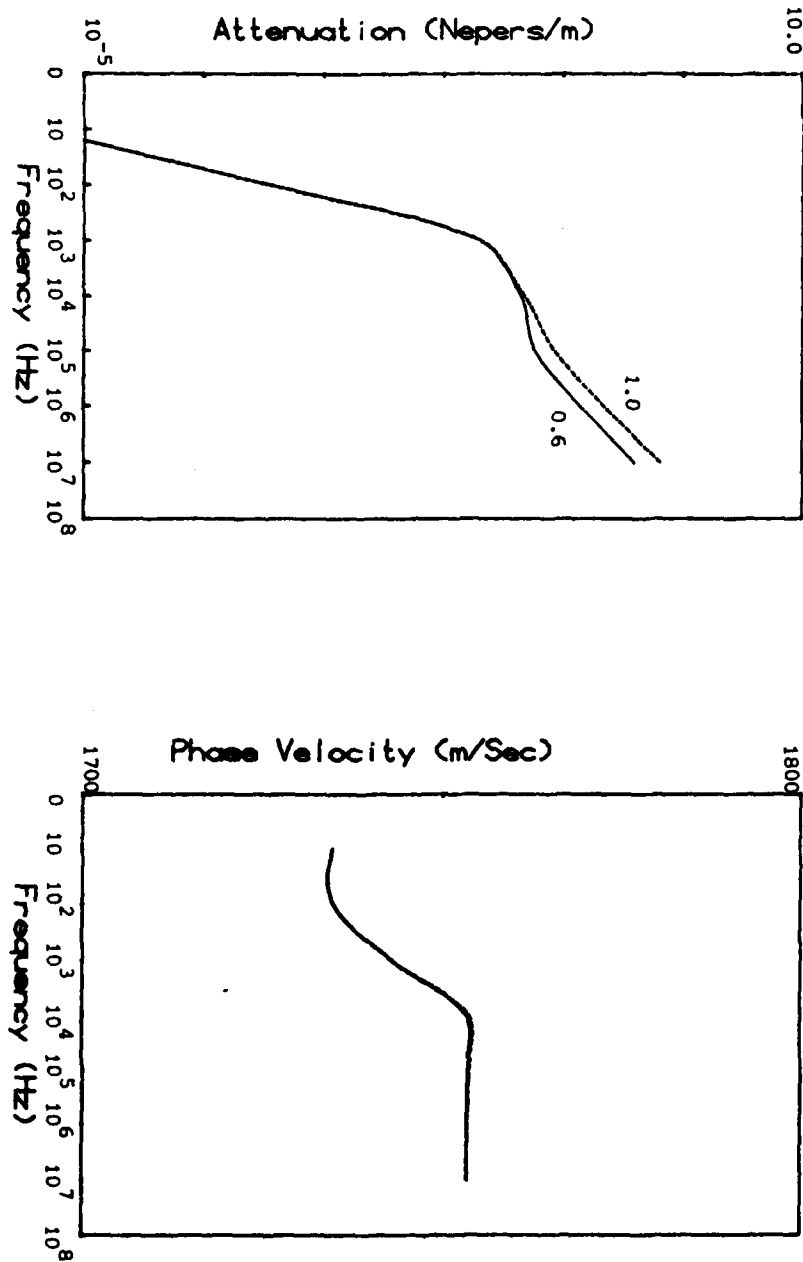
Figure 5.4   Sensitivity of fast wave characteristics in water-saturated sand to variation in shape factor ratio.

In Fig 5.5(a), the prediction for the frequency-dependent phase velocity and in Fig 5.5(b) the effect of variation in frame elasticity for the fast-wave in air-filled sand are shown. The predicted attenuation is less than 0.1dB/m in all cases. In Fig 5.6, we present real and imaginary parts of propagation constants for slow wave for the sake of comparison with those obtained using rigid-porous theory. This shows that the slow wave corresponds to that predicted in the modified fluid model of a rigid porous medium.

The range of values of oscillatory-flow pore-shape factor (see section 4.3) used in these calculations (equation (5.3)) differs from that quoted in Chapter 4 since it is derived from comparison the forms of $F(\lambda)$ for oscillatory flow in a cylindrical pore and parallel-sided slit rather than those of $\rho(\omega)$. The relevant parameter may be labelled n(viscous) where

$$0.75 \leqslant n(viscous) \leqslant 1$$

The bulk modulus of air, K_f, must be complex to account for thermal effects in air-filled porous media. The required complex value may be obtained from equation (4.6) where $K_f = 1/C(\omega)$ and the required value for oscillatory-flow pore shape-factor, n(thermal) is such that

$$0.5 \leqslant n(thermal) \leqslant 1$$

Relationships equivalent to (4.22) may be invoked between the various shape factors viz.

$$2n(viscous) = n(thermal) + 1$$
$$2n(viscous) = 3 - s$$

and

$$1 \leqslant s \leqslant 1.5$$

where s is the steady flow shape factor defined in section 4.4.

For the computations in Figures 5.5 and 5.6, we have used the base values n(thermal) = 0.5 and n(viscous) = 0.75. The remaining parameter values are given in Table II.

Note that a single value of oscillatory-flow pore-shape factor n(viscous) may be used if $C(\omega)$ is calculated from

$$C(\omega) = (\gamma P_o)^{-1} [2 - \gamma + 2(\gamma - 1)(N_{Pr}^{\frac{1}{2}}\lambda\sqrt{i}) \ T(N_{Pr}^{\frac{1}{2}}\lambda\sqrt{i})/F(N_{Pr}^{\frac{1}{2}}\lambda\sqrt{i})]$$

where γ is the ratio of specific heats, N_{Pr} is the Prandtl Number and P_o is atmospheric pressure.

TABLE II

Parameters Required By Biot Theory
(As Modified By Attenborough/Rayleigh)

Parameter	"Sand" Value
Grain Bulk Modulus	3.6×10^{11} dyn/cm^2
Grain Mass Density	2.68 g cm^{-3}
Frame Bulk Modulus	8.27×10^9 dyn/cm^2
Frame Rigidity Modulus	8.27×10^9 dyn/cm^2
Fluid Bulk Modulus (isothermal)	
Dynamic Viscosity of Fluid	.00184 dyn-sec/cm^2
Porosity	0.4
Permeability	3.76×10^{-6} cm^2
Grain shape factor	0.5
Shape factor ratio (n/$\sqrt{s}$)	0.6
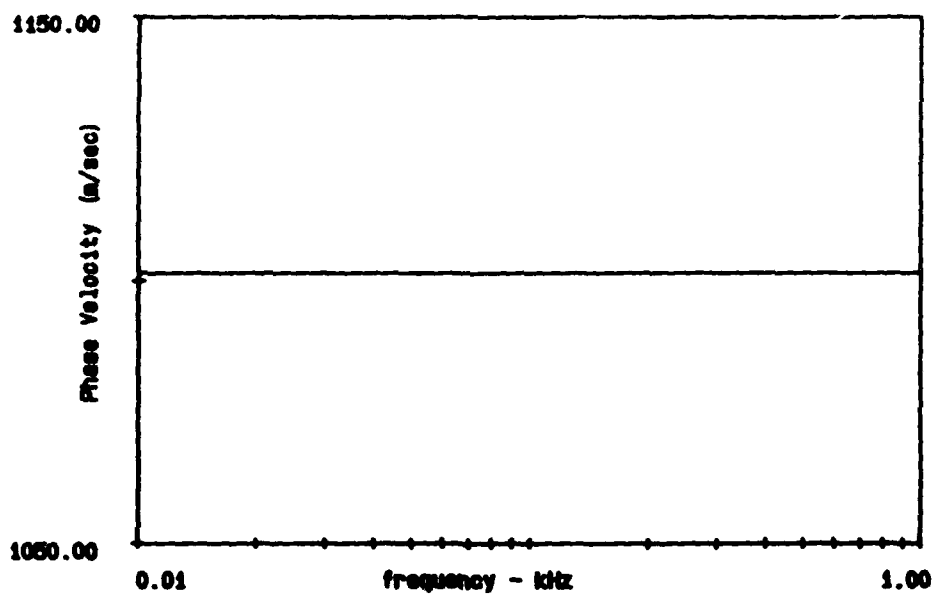
Figure 5.5(a) Predicted fast-wave phase velocity for air-filled
sand with characteristics given by Table II.
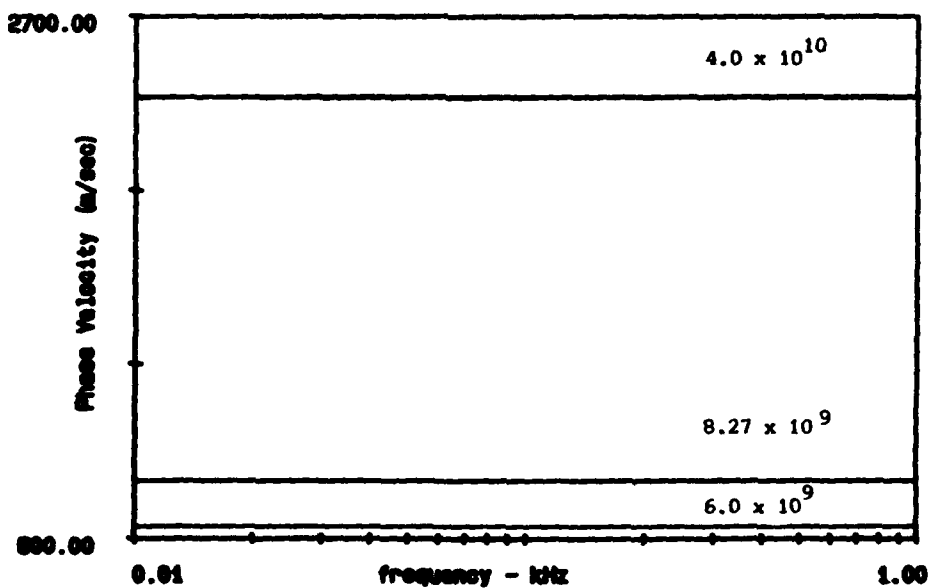
Figure 5.5(b) Variation of fast-wave speed characteristic in
air-filled sands with labelled values of frame
elastic constants
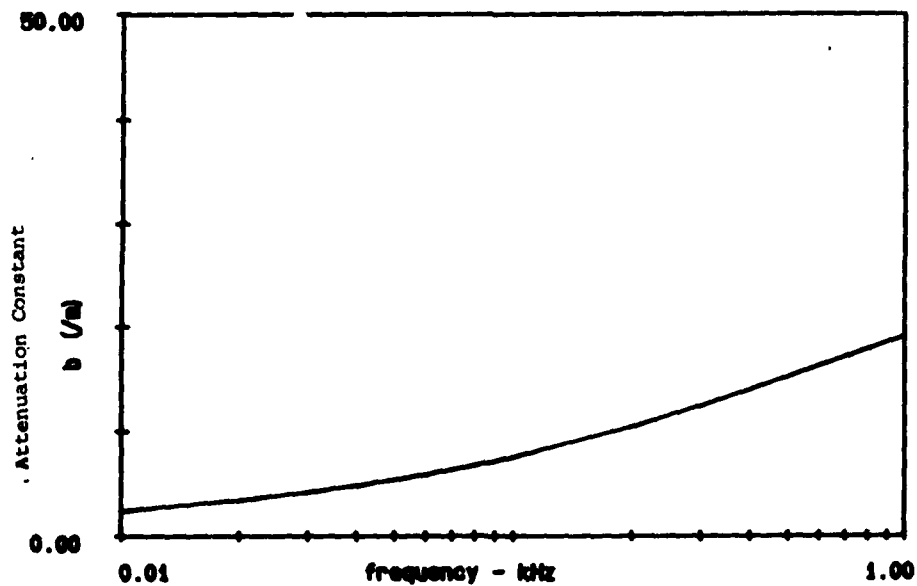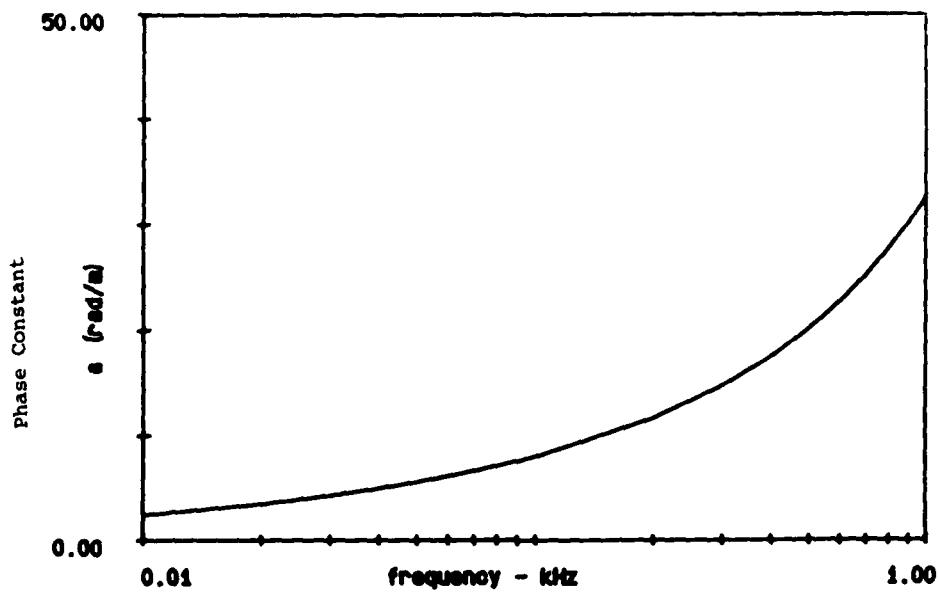
5.6 Predicted real and imaginary parts of slow-wave propagation
constant in air-filled sand with characteristics given in
Table II.

As has been shown, the values predicted for the fast wave propagation constant in air-saturated sand are very sensitive to the value taken by the frame rigidly (shear) modulus (assumed equal to the bulk modulus). The shear modulus for soils is affected by various soil parameters and the state of stress. The important parameters include [5.7] effective octahedral normal stress, void ratio, grain characteristics, shape, size, grading, mineralogy, amplitude strain, ambient stress history, secondary time-dependent effects, degree of water saturation, octahedral shear stress, frequency of vibration, soil structure and temperature. This complexity implies difficulty with selecting values typical of any given soil type. Consequently three values have been chosen which indicate a typical range and enable a study of the sensitivity of propagation characteristics to shear modulus in air-filled soils. The values chosen [5.8] are set out below:-

Soil type	Shear Modulus (G) dyn cm^{-2}
Santa Barbara clay	1.38×10^8
AGSCO No.2	5.17×10^8
Ottawa sand	1.86×10^9

Figures 5.7 to 5.10 show the relative speeds and attenuations of the three possible wave types predicted by assuming equal shear and bulk moduli and using the base values of other parameters given in Table II with the exceptions $n' - 1$ and shape factor ratio = 0.75. Figure 5.7 shows that, for a relatively high value of rigidity modulus, the 'slow' wave is clearly the slowest up to 1kHz, the fast wave having a frequency independent value somewhat greater than the velocity of sound in air and similar to the value predicted for dry sand. From Figures 5.7 and 5.8 it is clear that a small decrease in rigidity modulus causes the shear wave to become faster than the slow wave near 1kHz. Note that both of the rigidity modulus values assumed in generating Figures 5.7 and 5.8 produce fast wave speeds somewhat less than the speed of sound in air.

Further decrease in the rigidity modulus to the value assumed in Figure 5.10

produces the interesting situation where the 'slow' and 'fast' waves are

predicted to exchange roles above 100 Hz. It should be noted that still

lower values of rigidity modulus are possible for soils and these will

produce 'slow' and 'fast' wave exchange at still lower frequencies. Finally

addition of a complex component of the shear modulus is shown, in Figure 5.11,

to produce, as expected, much higher attenuations for the 'fast' and shear
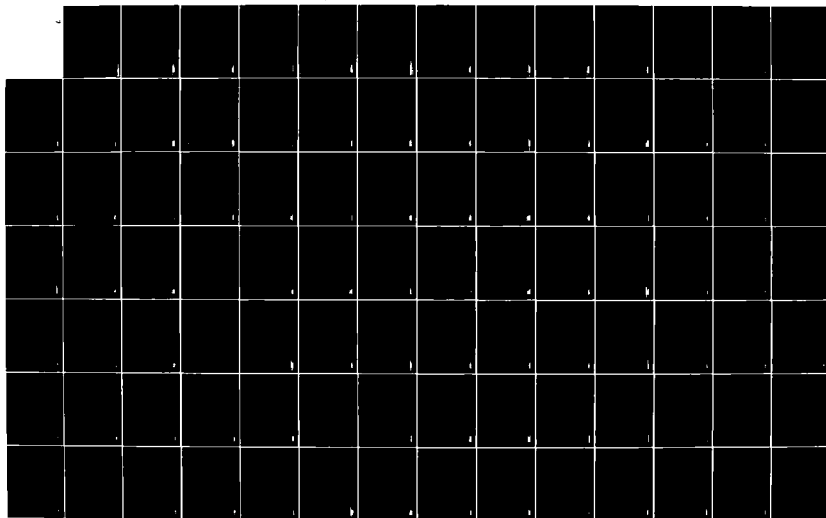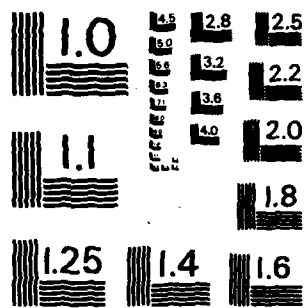
waves.

MICROCOPY RESOLUTION TEST CHART

NATIONAL BUREAU OF STANDARDS-1963-A
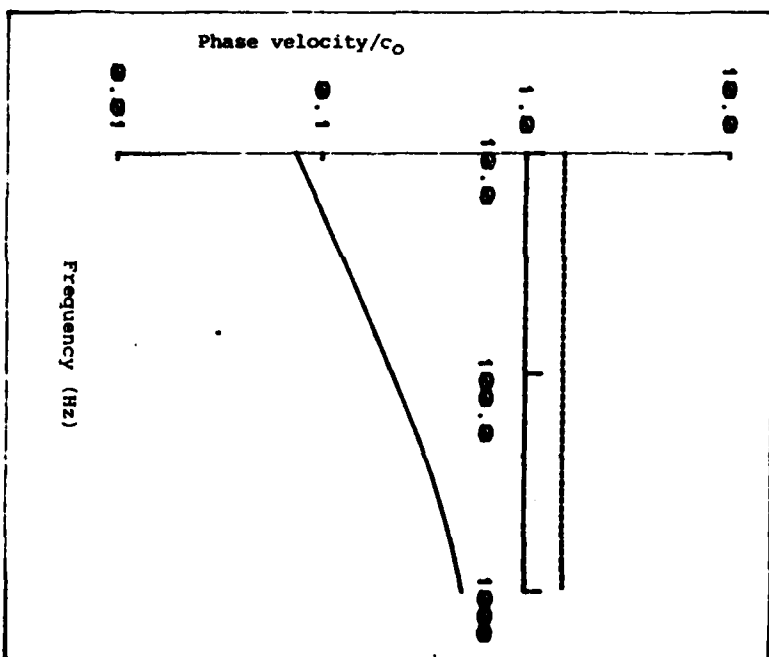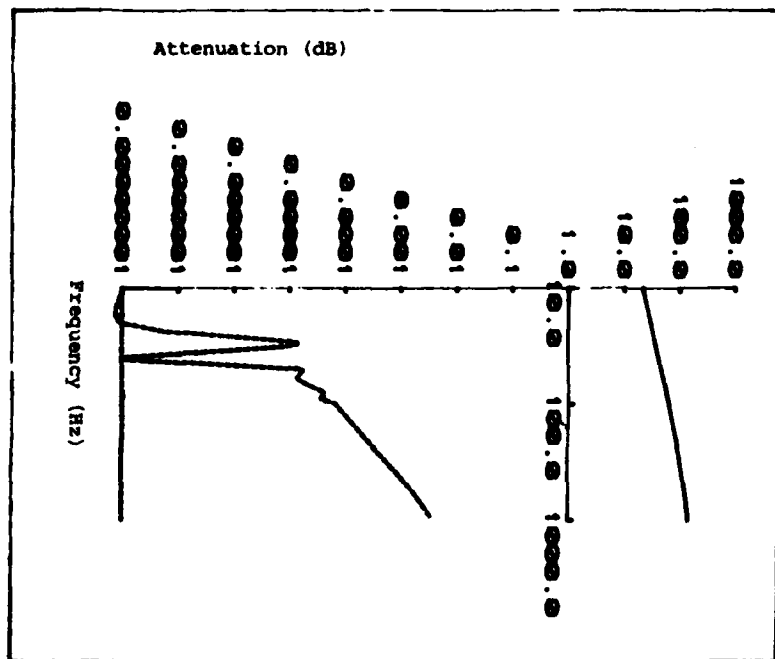
Figure 5.7 Predicted propagation constants for dry soil of rigidity modulus 1.86×10^9 dyn cm^{-2}

--- fast wave   —— slow wave   — — shear wave
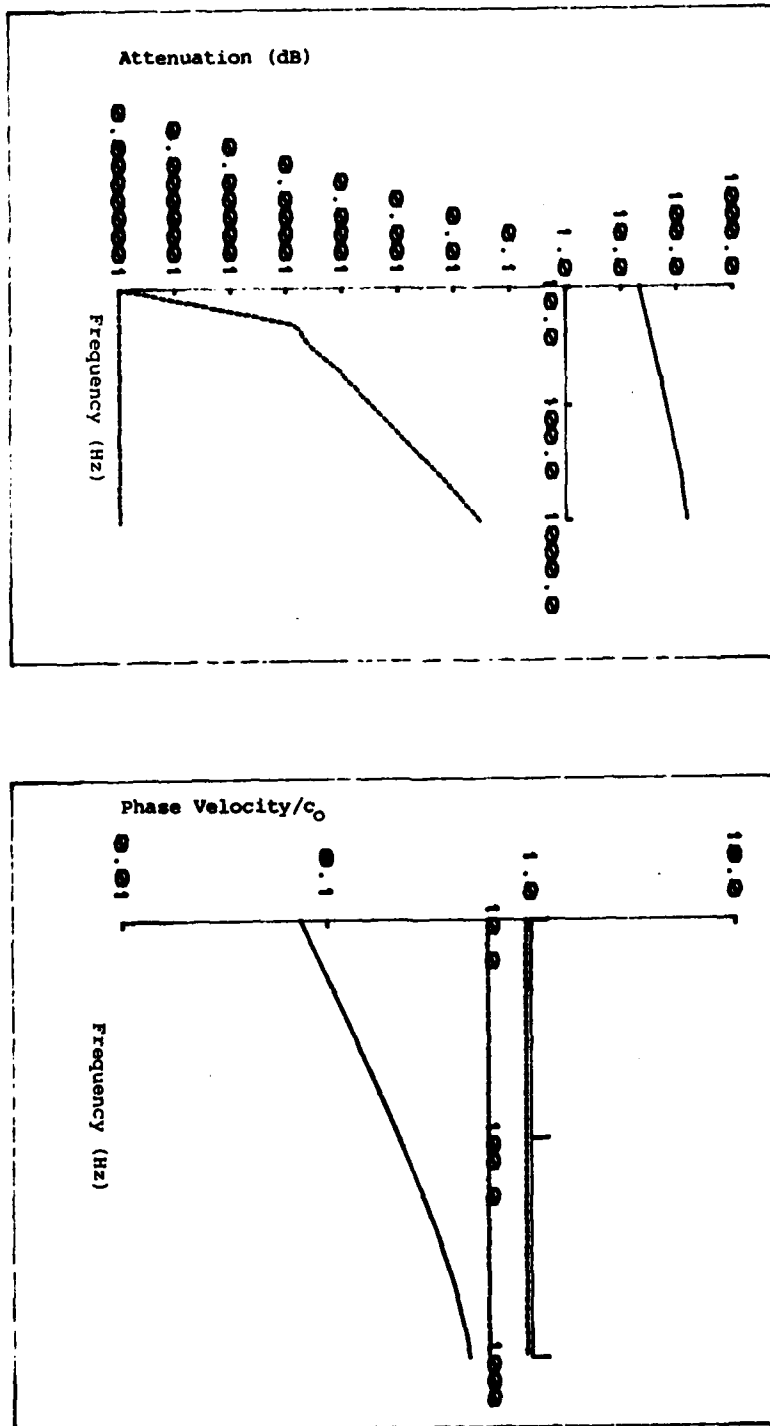
Figure 5.8 Predicted propagation constants for dry soil of rigidity modulus 7.03×10^8 dyn cm^{-2}

Attenuation (dB)

Frequency (Hz)

Phase velocity/c_o

Frequency (Hz)
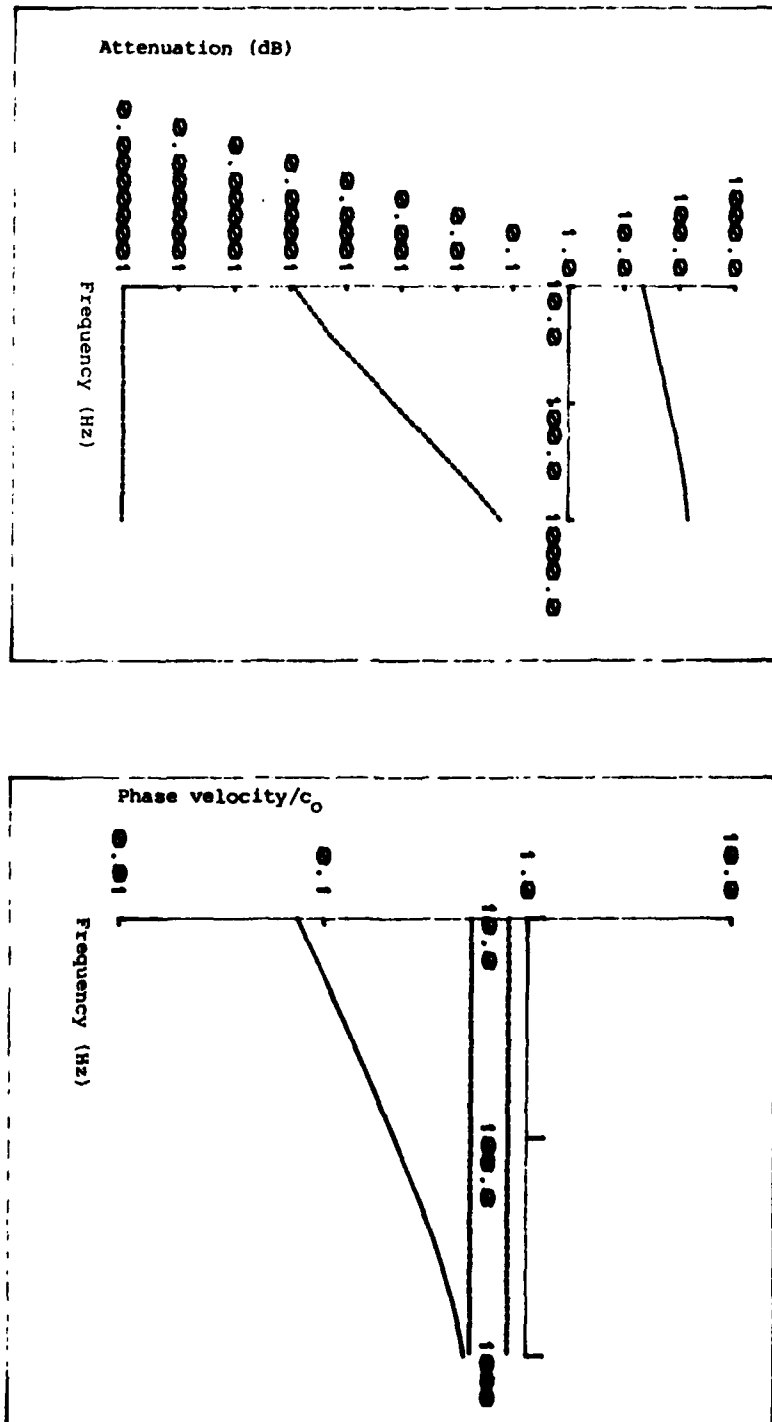
Figure 5.9 Predicted propagation constants for dry soil of rigidity modulus 5.17×10^8 dyn cm^{-2}
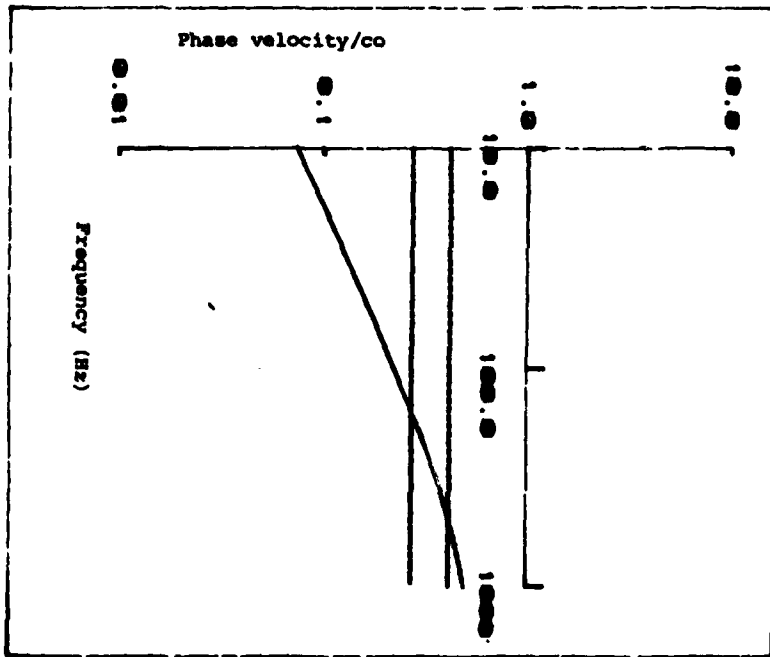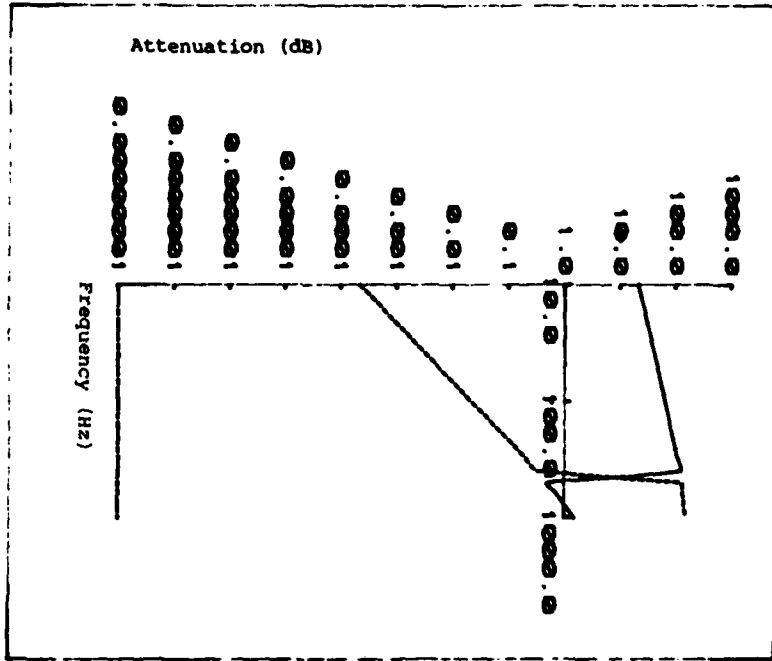
Figure 5.10 Predicted propagation constants for dry soil of rigidity modulus 1.38×10^8 dyn cm^{-2}
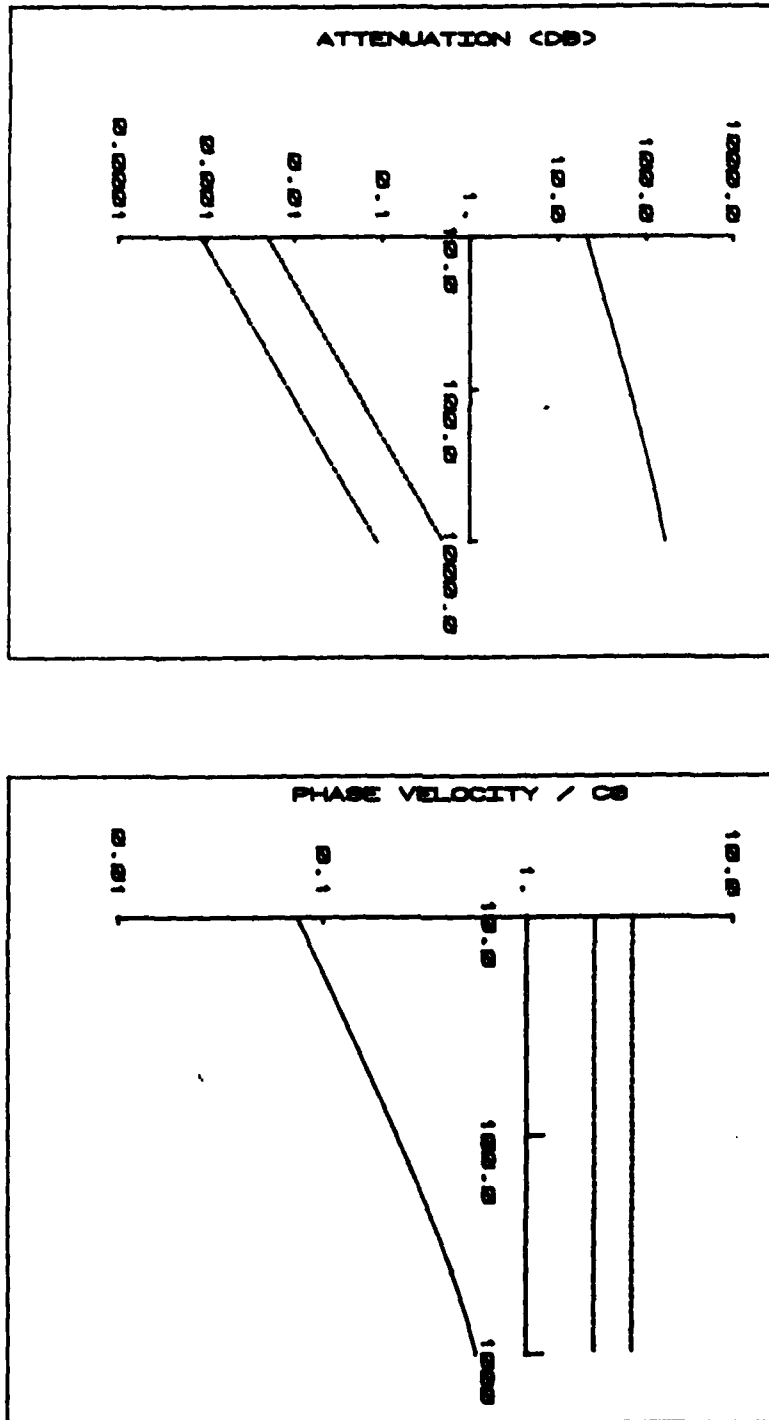
Figure 5.11   Predicted propagation constants for dry soil of complex rigidity modulus $8.77 \times 10^9 (1 + 10.02)$

5.3 Predictions of surface solid particle velocity resulting from plane wave incidence

The ratio of solid particle velocity to the pressure on the surface has been used to describe the ground response. To facilitate computations of this, we make use of a different but equivalent formulation to that presented in section 1. The present formulation enables us to express both solid and fluid displacement in terms of two scalar potentials ϕ_1 and ϕ_2 and two vector potentials $\underline{\psi}_1$ and $\underline{\psi}_2$. We write

$$\underline{u} = \text{grad } \phi_1 + \text{curl } \underline{\psi}_1$$

$$\underline{U} = \text{grad } \phi_2 + \text{curl } \underline{\psi}_2 \tag{5.9}$$

and they obey the following coupled differential equations

$$\nabla^2(P\phi_1 + Q\phi_2) = \frac{\partial^2}{\partial t^2}(\rho_1\phi_1) + bF(\lambda)\frac{\partial}{\partial t}(\phi_1 - \phi_2)$$

$$\nabla^2(Q\phi_1 + R\phi_2) = \frac{\partial^2}{\partial t^2}(\rho_2\phi_2) - bF(\lambda)\frac{\partial}{\partial t}(\phi_1 - \phi_2) \tag{5.10}$$

and

$$N\nabla^2\underline{\psi}_1 = \frac{\partial^2}{\partial t^2}(\rho_2\underline{\psi}_2) + bF(\lambda)\frac{\partial^2}{\partial t}(\underline{\psi}_1 - \underline{\psi}_2)$$

$$0 = \frac{\partial^2}{\partial t^2}(\rho_2\underline{\psi}_2) - bF(\lambda)\frac{\partial^2}{\partial t}(\underline{\psi}_1 - \underline{\psi}_2) \tag{5.11}$$

where $b = \eta/k$, ρ_1 and ρ_2 are densities of solid and fluid respectively. The elastic parameters P, Q, R can be related to K_r [5.5]. bulk modulus of grains, K_f (bulk modulus of fluid), K_b (bulk modulus of aggregate)

N is the shear modulus of the solid and composite

$$P = \frac{(1 - \Omega) \left[(1 - \Omega) - \frac{K_b}{K_r} \right] K_r + \Omega \frac{K_r}{K_f} K_b}{1 - \Omega - \frac{K_b}{K_r} + \Omega \frac{K_r}{K_f}} + \frac{4}{3}N$$

$$Q = \frac{\left[1 - \Omega - \frac{K_b}{K_r} \right] \Omega K_r}{\left[1 - \Omega - \frac{K_b}{K_r} + \frac{K_r}{K_f} \right]}$$

$$R = \frac{\Omega^2 K_r}{\left[1 - \Omega - \frac{K_b}{K_r} + \Omega \frac{K_r}{K_f} \right]} \tag{5.12}$$

From the computational point of view, the present formulation does not pose any additional problem as the previous program can be still used and Eqs. (5.12) provide for the translation between the two notations.

For comparison with measurements it is convenient to calculate
the square of the ratio of surface particle velocity to pressure
henceforth called the intensity ratio. These calculations are
described for obliquely-incident plane waves on a semi-infinite
poro-elastic medium and normal-incidence on a rigidly-backed
poro-elastic layer in Appendix 4.

Figures 5.12 and 5.13 show plots of normal-incidence intensity ratio
against frequency for the parameter values given in Table II.
These are expected to be representative of sand. It should
be noted that the number of layer resonances increases with
increasing depth.

The variation of intensity ratio with angle of incidence, on a
semi-infinite layer of dry sand, measured away from the normal
and with frequency is shown in Figure 5.14. The ratio decreases
with increasing angle of incidence and, for any given angle, the
ratio decreases with increasing frequency.
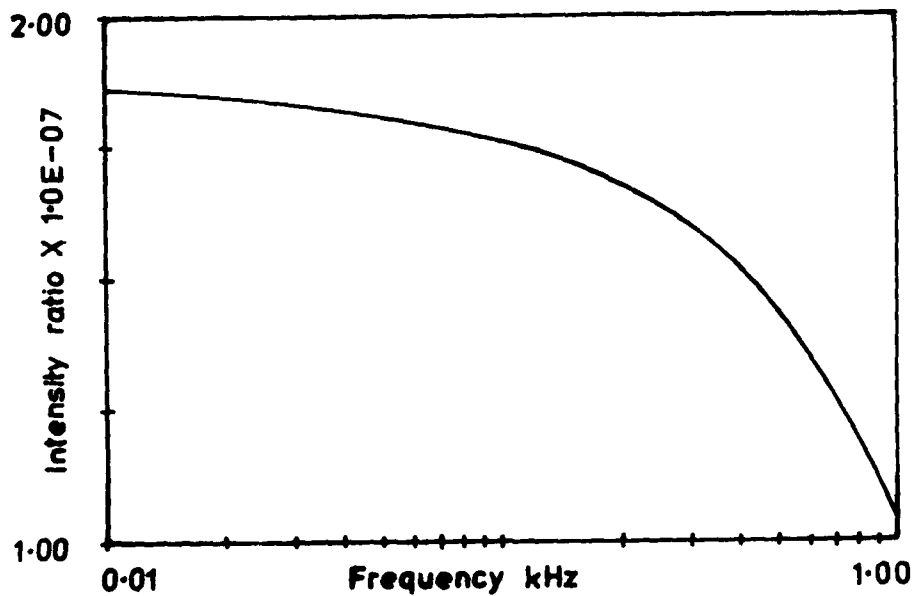
Figure 5.12 Predicted semi-infinite-sand surface intensity ratio for
normally-incident plane waves
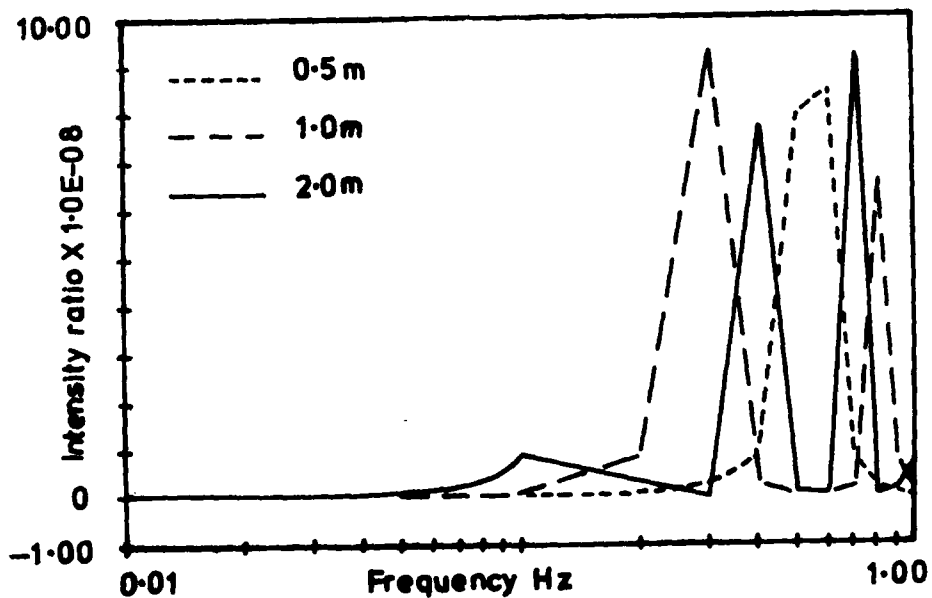
Figure 5.13 Predicted rigidly-backed sand layer surface intensity ratio for
normally-incident plane waves and layer depths between 0.5m and 2.0m.
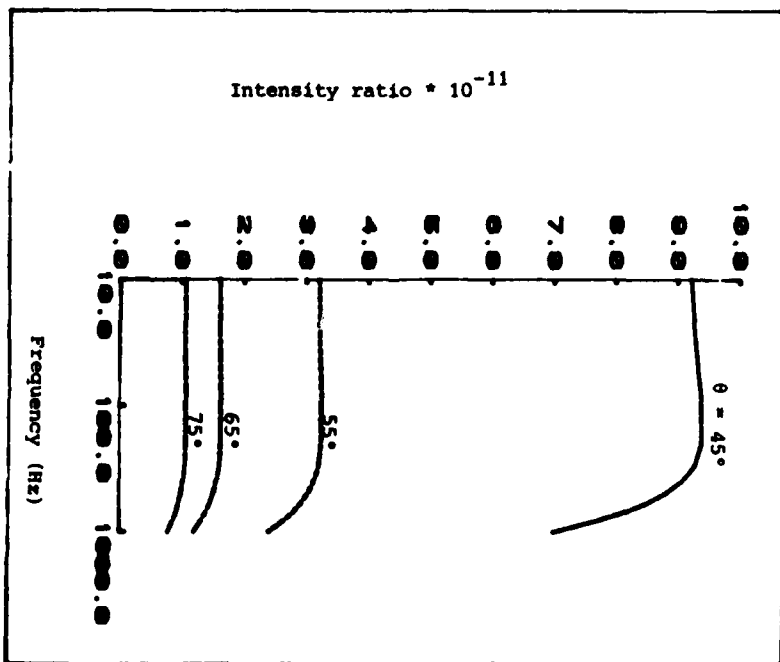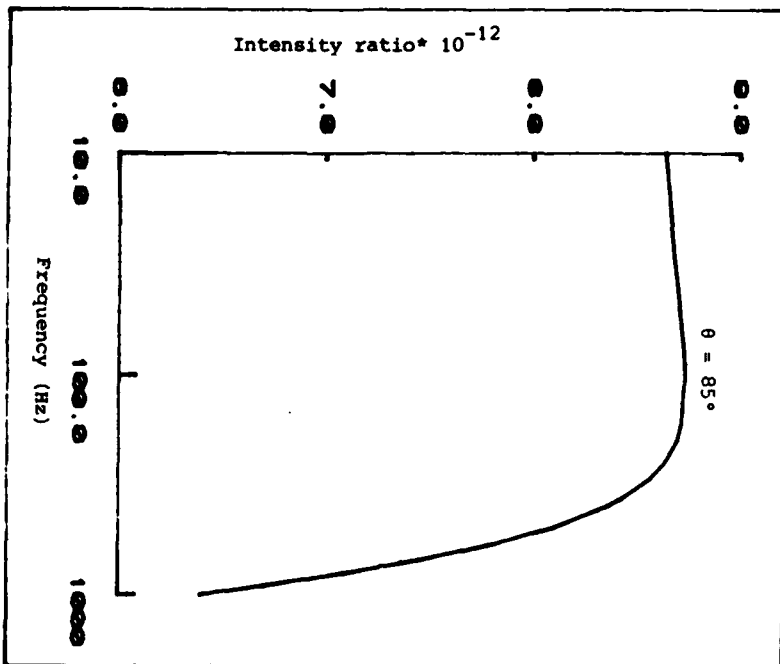
Figure 5.14   Surface intensity ratio predicted for oblique-incidence on a semi-infinite layer of dry sand. Angles of incidence are measured away from the normal.

References

[5.1]   Biot, M.A., "Theory of propagation of elastic waves in a
        fluid saturated porous solid I and II", J. Acoust, Sec
        Amer, 28(2), 168-178, 179-191 (1956).

[5.2]   Carman, P.C., Flow of gases through porous media, New York,
        Academic Press (1956).

[5.3]   Attenborough, K. Acoustical characteristics of rigid
        absorbents and granular media. J. Acoust. Sec. Amer 73 (3),
        785-799 (1983) and Attenborough, K. Influence of microstructure
        on viscous attenuation in unconsolidated sediments. Proc.
        Inst. of Acoustics meeting Acoustics and the Sea Bed ed. N.G. Pace
        Bath University Press, April 1983.

[5.4]   Stoll, R.D. and Bryan, G.M. Wave alternation in saturated
        sediments. J. Acoust. Sec. Amer, 47(5), 1440-1443, (1970)

[5.5]   Geertsma J. and Smit, D - C. "Some aspects of elastic wave
        propagation in fluid - saturated porous solids, Geophysics,
        26(2), 169 - 181 (1961).

[5.6]   Flohr, M.D. and Cress, D.H. Acoustic-to-seismic coupling
        properties and applications to seismic sensors. Technical
        Report EL-79-1 U.S. Army WES, February 1979.

[5.7]   Hardin, B.O. and Black, W.L. Vibration Modulus of normally
        consolidated clay J. Soil Mech. and Found Div. Proc. A.S.M.E.
        94 SM2 353-369 March 1968.

[5.8]   Richart, F.E. and Wylie, E.B.   Influence of dynamic soil properties
on response of soil masses.   Structural and Geotechnical Mechanics,
Prentice-Hall, Inc. Englewood Cliffs, New Jersey U.S.A. ed. W.J. Hall
141-162

6. THE SURFACE MOTION OF A PORO-ELASTIC HALF-SPACE DUE TO AN INCIDENT
SPHERICAL SOUND WAVE.

6.1 Introduction

While the treatment of the ground surface as a rigid porous medium
gives an adequate description of the reflected sound wave and the
transmitted slow wave (consisting of air motion within the pores),
any attempt to determine the seismic response must take into account
the finite rigidity and density of the solid medium.

Here we take account of frame elasticity by using the theory of
propagation in poroelastic media outlined in the previous chapter.
This has been developed extensively by Biot in a number of publications.
In these he does not always use the same scheme of notation, and we opt
for the system given by him in 1961 [6.1]. This gives the most
compact expressions in subsequent derivations, and many of the material
parameters are defined in such a way as to be identical to those of the
corresponding rigid porous material.

The problem of spherical wave incidence on a poro-elastic half space
is approached in the same manner as that for the more well-known
cases of fluid-fluid, fluid-solid and solid-solid interfaces, which
which are described by, for example, Ewing et al [6.2]. The
axisymmetric displacement potentials are expressed in terms of

inverse Hankel transforms, the transformed potentials being determined by the boundary conditions at the interface. In this case there are four potentials, corresponding to the reflected compressional wave in the upper medium, the transmitted slow and fast compressional waves, and the transmitted shear wave.

The complexity of the resulting integrals prohibits a thorough analysis using the saddle point method as in the fluid-fluid case used to model a rigid porous ground surface. However, a simpler, less rigorous approach enables us to obtain asymptotic expressions for the various wave types at grazing incidence, and it is also straight forward to identify the propagation paths and evaluate times of arrival for transient sources.

Some simplification is possible by considering the limiting case when the bulk modulus and density of the saturating fluid are much smaller than the elastic modulus and density of the solid. The propagation constants of the fast and shear wave are unaffected by the presence of the fluid, while that of the slow wave is the same as for the rigid porous case. This 'light fluid' limit should be applicable for air-filled ground surfaces.

Feng and Johnson [6.3, 6.4] have recently considered the problem of a fluid/porous solid interface. Their treatment, otherwise comprehensive, gives results for the high frequency limit when the propagation constants for the various wave types are all real and non-dispersive. This allows them to define 'true' surface waves with a velocity less than any of the body waves, and to implement the Cagniard method when evaluating the response to a pulsed source. However, the simplest possible treatment of ground surfaces must admit a complex slow wave propagation constant, and as a result we are forced to give a more general analysis of surface wave contributions.

6.2. Displacement potential in the upper medium

The vector of fluid displacement in the upper medium is defined in terms
of the potential ψ:

$$\underline{v} = \underline{\nabla}\psi \tag{6.1}$$

The acoustic pressure is given by

$$p = -K_a\underline{\nabla}.\underline{w} = -K_a\nabla^2\psi \tag{6.2}$$

where K_a is the bulk modulus

ψ obeys the wave equation

$$\nabla^2\psi = \frac{1}{c^2}\frac{\partial^2\psi}{\partial t^2} \tag{6.3}$$

everywhere in the upper medium except at the source.

6.3 *Displacement potentials in the lower medium*

If the displacement vector of the solid matrix is $\underline{u}$, then following Biot [6.1] we represent the displacement of fluid in the pores relative to the solid by the vector

$$\underline{w} = \Omega(\underline{U} - \underline{u}) \tag{6.4}$$

where Ω is the porosity and $\underline{U}$ is the actual average fluid displacement. Hence $\underline{w}$ is the relative volume displacement of the fluid over unit area of the bulk medium.

Because the solid can support shear stress the displacement are not in general irrotational. They can be detained in terms of scalar and vector potentials as follows:

$$\underline{w} = \underline{\nabla}\phi_2 + \underline{\nabla} \times \underline{\chi}_2 \tag{6.5}$$

$$\underline{u} = \underline{\nabla}\phi_3 + \underline{\nabla} \times \underline{\chi}_3 \tag{6.6}$$

The coupled equations of propagation for dilatational waves are

$$\nabla^2(H\phi_3 + \alpha M\phi_2) = \frac{\partial^2}{\partial t^2}(\rho\phi_3 + \rho_1\phi_2) \tag{6.7a}$$

$$\nabla^2(\alpha M\phi_3 + M\phi_2) = \frac{\partial^2}{\partial t^2}(\rho_1\phi_3 + m\phi_2) + \frac{\eta F}{k}\frac{\partial\phi_2}{\partial t} \tag{6.7b}$$

and *for shear waves*

$$\mu\nabla^2 \chi_3 = \frac{\partial^2}{\partial t^2} (\rho \chi_3 + \rho_1 \chi_3) \qquad (6.8a)$$

$$\frac{-\eta F}{k} \frac{\partial \chi_2}{\partial t} = \frac{\partial^2}{\partial t^2} (\rho_1 \chi_3 + m \chi_2) \qquad (6.8b)$$

where H, μ are elastic moduli of the medium with sealed pores,

$\quad$ M $\quad$ is the effective bulk modulus of the fluid in the pores,

$\quad$ ρ_1 $\quad$ is the density of the fluid,

$\quad$ ρ $\quad$ is the average density of the porous medium (including fluid and solid),

$\quad$ m $\quad$ is the effective inertial density of the fluid in the pores,

$\quad$ η $\quad$ is the fluid viscosity,

$\quad$ k $\quad$ is the permeability of the porous medium,

$\quad$ F $\quad$ is a complex frequency dependent function which corrects for departures from Poiseuille flow,

and α $\quad$ is a parameter which relates changes in pore volume to overall changes in volume.

6.4 Boundary conditions at the interface.

The definitions of fluid and solid displacement used here lead to particularly simple expressions for the boundary conditions.

Assuming open pores at the interface, the boundary condition for continuity of fluid displacement is

$$\underline{n}. \; (\underline{u} + \underline{w}) = \underline{n}.\underline{\nabla}\psi$$

where $\underline{n}$ is a unit vector in the vertical direction. In terms of the displacement potentials this becomes

$$\underline{n}.\underline{\nabla} \; (\phi_2 + \phi_3) + \underline{n}.\underline{\nabla} \times (\underline{\chi}_2 + \underline{\chi}_3) = \underline{n}.\underline{\nabla}\psi \tag{6.9}$$

Biot's notion of 'effective stress' is particularly appropriate for the application of stress boundary conditions. The effective stress, t'_{ij}, is that part of the total stress within the porous medium (acting on both fluid and solid) in excess of the local fluid pressure. The components of effective stress acting in the plane of the interface must therefore be equal to zero. Follwoing Biot's definitions and using Cartesian coordinates x,y,z with the z axis in the vertical normal direction, we have

$$t'_{zz} = 2\mu e_z + (H - 2\mu - \alpha M)e + M(1 - \alpha) \zeta$$
$$= 0 \tag{6.10}$$

$$t'_{yz} = \mu \left(\frac{\partial u_y}{\partial z} + \frac{\partial u_z}{\partial y} \right) \qquad = 0 \qquad\qquad (6.11)$$

$$t'_{xz} = \mu \left(\frac{\partial u_z}{\partial x} + \frac{\partial u_x}{\partial z} \right) \qquad = 0 \qquad\qquad (6.12)$$

where $\quad e_z = \dfrac{\partial u_z}{\partial z}$

$$e = \nabla \cdot \underline{u}$$

$$\zeta = -\nabla \cdot \underline{w}$$

Finally, the pressure in the pores must be equated to that in the upper medium, giving

$$p + \alpha M e - M \zeta = 0 \qquad\qquad (6.13)$$

We later express the stress boundary conditions in terms of the potentials when transforming to axisymmetric coordinates.

6.5 Time dependence

We subsequently assume that all displacements and potentials vary as $e^{-i\omega t}$, so that

$$\underline{u} \rightarrow \underline{u}\, e^{-i\omega t} \quad \text{etc.}$$

$$\psi \rightarrow \psi\, e^{-i\omega t} \quad \text{etc}$$

In the wave equations we also have

$$\frac{\partial}{\partial t} \rightarrow -i\omega$$

$$\frac{\partial^2}{\partial t^2} \rightarrow -\omega^2$$

Equation (6.3) becomes

$$\nabla^2 \psi + k_1^2 \psi = 0 \tag{6.14}$$

where $k_1 = \dfrac{\omega}{c}$

Equations (6.7a), (6.7b) become

$$\nabla^2 (H\phi_3 + \alpha M\phi_2) + \omega^2 (\rho\phi_3 + \rho_1\phi_2) = 0 \tag{6.15a}$$

$$\nabla^2 (\alpha M\phi_3 + M\phi_2) + \omega^2 (\rho_1\phi_3 + \rho_2\phi_2) = 0 \tag{6.15b}$$

where $\rho_2 = m + \dfrac{i\eta F}{\omega k}$

The complex density ρ_2 is identical to that for the equivalent rigid porous material. The reduction to this case can be achieved simply by setting the solid displacement potential ϕ_3 equal to zero in equation (6.15b). This gives

$$\nabla^2 \phi_2 + \frac{\omega^2 M}{\rho_2} \phi_2 = 0$$

From equation (4.16) we can deduce the complex density for a rigid porous material and we have

$$\rho_2 = (q^2/\Omega)\rho(\omega), \quad m = (q^2/\Omega)\rho_1$$

From the associated wave equation (4.17) we can now also deduce that

$$\frac{1}{M} = \Omega C(\omega)$$

For the shear wave motion, equations (6.8a), (6.8b) become

$$\mu\nabla^2 \underline{X}_3 + \omega^2(\rho\underline{X}_3 + \rho_1\underline{X}_2) = 0 \tag{6.16a}$$

$$\rho_1\underline{X}_3 + \rho_2\underline{X}_2 = 0 \tag{6.16b}$$

6.6. The axisymmetric case

In cylindrical coordinates we have, typically,

$$\underline{v}(x,y,z) \rightarrow \underline{v}(r, \theta, z)$$

and in the axisymmetric case

$$u_\theta = 0$$

$$w_\theta = 0$$

$$v_\theta = 0$$

and $\partial/\partial\theta = 0$

Equations (6.5) and (6.6) can now be written

$$w_r = \frac{\partial\phi_2}{\partial r} + \frac{\rho_1}{\rho_2} \frac{\partial^2\phi_4}{\partial r\partial z} \qquad\qquad \left.\begin{matrix} \\ \\ \\ \\ \\ \\ \\ \\ \end{matrix}\right\} \quad (6.17)$$

$$w_z = \frac{\partial\phi_2}{\partial z} - \frac{\rho_1}{\rho_2} \frac{1}{r} \frac{\partial}{\partial r}\left(r \frac{\partial\phi_4}{\partial r}\right)$$

$$u_r = \frac{\partial\phi_1}{\partial r} - \frac{\partial^2\phi_4}{\partial r\partial z} \qquad\qquad \left.\begin{matrix} \\ \\ \\ \\ \\ \\ \\ \\ \end{matrix}\right\} \quad (6.18)$$

$$u_z = \frac{\partial\phi_1}{\partial z} + \frac{1}{r} \frac{\partial}{\partial r}\left(r \frac{\partial\phi_4}{\partial r}\right)$$

The scalar potentials ψ, ϕ_2, ϕ_3 depend on r and z only, and X_2, X_3 are now defined in terms of the single axisymmetric scalar ϕ_4 with

$$X_3 = \left\{0\right\}\underline{a}_r + \left\{\frac{\partial\phi_4}{\partial r}\right\}\underline{a}_\theta + \left\{0\right\}\underline{a}_z$$

and by noting that from equation (6.16b)

$$\frac{X_2}{} = \frac{-\rho_1}{\rho_2} \frac{X_3}{}$$

The shear wave motion governed by the vector equations (6.16a),(6.16b) may now be described by a single scalar equation:

$$\nabla^2 \phi_4 + k_4^2 \phi_4 = 0 \tag{6.19}$$

where $\quad k_4^2 = \dfrac{\omega^2 \rho}{\mu} (1 - \dfrac{\rho_1^2}{\rho\rho_2})$ \hfill (6.20)

6.7 Axisymmetric boundary conditions

Using the definitions of the axisymmetric potentials already given and
the usual vector differential operators appropriate for cylindrical
coordinates, equation (6.9) becomes

$$\frac{\partial}{\partial z}(\phi_2 + \phi_3) + (1 - \frac{\rho_1}{\rho_2})\frac{1}{r}\frac{\partial}{\partial r}(r\frac{\partial \phi_4}{\partial r}) - \frac{\partial \psi}{\partial z} = 0$$

or, since $\qquad \frac{1}{r}\frac{\partial}{\partial r}(r\frac{\partial}{\partial r}) \equiv (\nabla^2 - \frac{\partial^2}{\partial z^2})$ for axisymmetric cases

$$\frac{\partial}{\partial z}(\phi_2 + \phi_3) + (1 - \frac{\rho_1}{\rho_2})(\nabla^2\phi_4 - \frac{\partial^2\phi_4}{\partial z^2}) - \frac{\partial \psi}{\partial z} = 0 \qquad (6.21)$$

Equation (6.10) becomes

$$2\mu\frac{\partial}{\partial z}\left[\frac{\partial\phi_3}{\partial z} + \nabla^2\phi_4 - \frac{\partial^2\phi_4}{\partial z^2}\right] + (H - 2\mu - \alpha M)\nabla^2\phi_3 - M(1 - \alpha)\nabla^2\phi_2 = 0 \qquad (6.22)$$

Equations (6.11) and (6.12) are satisfied in the axisymmetric case if

$$\frac{\partial u_r}{\partial z} + \frac{\partial u_z}{\partial r} = 0$$

or, in terms of potentials,

$$\frac{\partial}{\partial r}\left[2\frac{\partial\phi_3}{\partial z} - 2\frac{\partial^2\phi_4}{\partial z^2} + \nabla^2\phi_4\right] = 0$$

Since the bracketted term must approach zero as $r \to \infty$, this boundary condition means that it must be zero everywhere, that is

$$2\frac{\partial \phi_3}{\partial z} - 2\frac{\partial^2 \phi_4}{\partial z^2} + \nabla^2 \phi_4 = 0 \qquad (6.23)$$

After substituting the appropriate potentials, equation (6.13) becomes

$$M\nabla^2 \phi_2 + \alpha M \nabla^2 \phi_3 - K_a \nabla^2 \psi = 0 \qquad (6.24)$$

We shall ultimately use the four boundary conditions (6.21) - (6.24) to determine the four potentials ψ, ϕ_2, ϕ_3, ϕ_4.

6.8 General solutions

Assuming a point source of sound at a height z_0 above the interface, the solution to (6.14) may be written

$$\psi = \frac{e^{ik_1 R}}{R} + \phi_1(r,z)$$

where $R^2 = r^2 + (z - z_0)^2$, and ϕ_1 represents the wave reflected from the interface.

The general solution in axisymmetric coordinates may be written as an inverse Hankel transform:

$$\phi_1(r,z) = \int_0^\infty \overline{\phi}_1(K)e^{-\nu_1 z} J_0(Kr)KdK \qquad (6.25)$$

where $\nu_1 = (K^2 - k_1^2)^{\frac{1}{2}}$, Re $\nu_1 > 0$, $z > 0$, Im$(k_1) \geqslant 0$. and $\overline{\phi}_1$ is the transformed potential for $z = 0$.

The total field above the interface, using the integral representation for the point source, is

$$\psi = \int_0^\infty \left[\frac{e^{-\nu_1 |z-z_0|}}{\nu_1} + \overline{\phi}_1 e^{-\nu_1 z} \right] J_0(Kr)KdK \qquad (6.26)$$

For the field below the surface, in equations (6.15a), (6.15b) we try solutions of the form

$$\phi_2 = \int_0^\infty \bar{\phi}_2(K) e^{\alpha z} J_o(Kr) K dK \qquad (6.27)$$

$$\phi_3 = \int_0^\infty \bar{\phi}_3(K) e^{\alpha z} J_o(Kr) K dK \qquad (6.28)$$

where $z < 0$ and α is as yet unspecified. Substitution of these leads to two linear equations for the transformed potentials:

$$a^2(H\bar{\phi}_3 + \alpha M \bar{\phi}_2) - \omega^2(\rho\bar{\phi}_3 + \rho_1\bar{\phi}_2) = 0 \qquad (6.29)$$

$$a^2(\alpha M \bar{\phi}_3 + M\bar{\phi}_2) - \omega^2(\rho_1\bar{\phi}_3 + \rho_2\bar{\phi}_2) = 0 \qquad (6.30)$$

where $a^2 = K^2 - \gamma^2$. Equating the determinant of these equations to zero gives the non-zero solutions, and we obtain

$$(a^2 H - \omega^2\rho)(a^2 M - \omega^2\rho_2)$$

$$-(a^2\alpha M - \omega^2\rho_1)^2 = 0 \qquad (6.31)$$

This quadratic gives two allowed values of a^2, and we can rewrite it as

$$(a^2 - k_3^2)(a^2 - k_2^2) - \frac{1}{HM}(a^2\alpha M - \omega^2\rho_1)^2 = 0 \qquad (6.32)$$

where $\quad k_2'^2 \;=\; \dfrac{\omega^2 \rho_2}{M}$ (6.33)

and $\quad k_3'^2 \;=\; \dfrac{\omega^2 \rho}{H}$ (6.34)

k_2' is the propagation constant for the equivalent rigid porous material, and k_3' is the propagation constant for compressional waves in the bulk medium assuming that relative motion between fluid and solid is constrained in some way.

Equation (6.32) is a quadratic which may be solved in the usual way to give two possible values of a.

If the second term in (6.32) is negligible then we must have

$$a^2 \;=\; \frac{(k_2'^2 + k_3'^2)}{2} \;\pm\; \frac{(k_3'^2 - k_2'^2)}{2}$$

$$=\; k_2'^2 \;\text{ or }\; k_3'^2 \tag{6.35}$$

For our application we do in fact expect that (6.32) will give two wavenumbers corresponding to distinct wave types, and also that $k_3' < k_2'$. Accordingly, we will call one solution k_2, and this is approximately equal to k_2' and associated primarily with motion of air in the pores known as the 'slow wave'. The second solution we call k_1, and this is the wavenumber of the compressional 'fast wave' determined chiefly by the properties of the solid part of the medium.

In equations (6.29) and (6.30) the two potentials must be in a fixed proportion for each allowed wavenumber. When $a = k_2$ we use (6.29) to obtain

$$a_{32} = \frac{\bar{\phi}_3}{\bar{\phi}_2} = \frac{\omega^2 \rho_3 - k_2^2 \alpha M}{H(k_2^2 - k_3'^2)} \qquad (6.36)$$

and when $a = k_3$ substitution into (6.30) gives

$$a_{23} = \frac{\bar{\phi}_2}{\bar{\phi}_3} = \frac{k_3^2 \alpha M - \omega^2 \rho_1}{M(k_3'^2 - k_3^2)} \qquad (6.37)$$

Equations (6.15a), (6.15b) therefore have two independent solutions. For the slow wave

$$\left. \begin{array}{l} \phi_2 = \displaystyle\int_0^\infty \bar{\phi}_2'(k) e^{\nu_2 Z} J_0(Kr) K dK \\[4mm] \phi_3 = a_{32} \phi_2 \end{array} \right\} \qquad (6.38)$$

and for the fast wave

$$\left. \begin{array}{l} \phi_3 = \displaystyle\int_0^\infty \bar{\phi}_3'(K) e^{\nu_3 Z} J_0(Kr) K dK \\[4mm] \phi_2 = a_{23} \phi_3 \end{array} \right\} \qquad (6.39)$$

where $\nu_2 = (K^2 - k_2^2)^{\frac{1}{2}}$

and $\nu_3 = (K^2 - k_3^2)^{\frac{1}{2}}$

$\bar{\phi}_2^{\,\prime}$ is that part of the transformed potential $\bar{\phi}_2$ associated purely with the slow wave. Similarly $\bar{\phi}_3^{\,\prime}$ is the part of $\bar{\phi}_3$ associated with the fast wave.

In general we may write

$$\phi_2 = \int_0^\infty (\bar{\phi}_2^{\,\prime} e^{\nu_2 z} + a_{23}\bar{\phi}_3^{\,\prime} e^{\nu_3 z})\, J_o(Kr)KdK \tag{6.40}$$

$$\phi_3 = \int_0^\infty (\bar{\phi}_3^{\,\prime} e^{\nu_3 z} + a_{32}\bar{\phi}_2^{\,\prime} e^{\nu_2 z})\, J_o(Kr)Kdk \tag{6.41}$$

Finally, the general axisymmetric solution for the shear wave motion described by equations (6.19) is

$$\phi_4 = \int_0^\infty \bar{\phi}(K) e^{\nu_4 z}\, J_o(kr)KdK \tag{6.42}$$

where $z<0$, $\nu_4 = (K^2 - k_4^2)^{\frac{1}{2}}$

6.9   Simultaneous equations for the transformed potentials

The general solution given by equations (6.26), (6.40) - (6.42)

for $z = 0$ are now substituted into the boundary conditions

(6.21) - (6.24). This leads to four linear equations in the

transformed potentials which, when satisfied, also satisfy the

boundary conditions.

Equation (6.21) is satisfied if

$$\nu_1 \bar{\phi}_1 + \nu_2 (1 + a_{32}) \bar{\phi}_2' + \nu_3 (1 + a_{33}) \bar{\phi}_3' - K^2 (1 - \frac{\rho_1}{\rho_2}) \bar{\phi}_4$$
$$= e^{-\nu_1 z_0} \qquad (6.43)$$

Equation (6.22) is satisfied if

$$\{2\mu a_{32} \nu_2^2 - k_2^2 \left[a_{32} (H - 2\mu - \alpha M) - M(1 - \alpha)\right]\} \bar{\phi}_2'$$

$$+ \{2\mu \nu_3^2 - k_3^2 \left[H - 2\mu - \alpha M - a_{33} M(1 - \alpha)\right]\} \bar{\phi}_3'$$

$$- 2\mu \nu_4 K^2 \bar{\phi}_4 = 0 \qquad (6.44)$$

Equation (6.23) is satisfied if

$$2a_{32} \nu_2 \bar{\phi}_2' + 2\nu_3 \bar{\phi}_3' - (2K^2 - k_4^2) \bar{\phi} = 0 \qquad (6.45)$$

EQUATION (6.47)

$$
\begin{bmatrix}
\nu_1 & \nu_2 & a_{32}\nu_3 & \dfrac{\rho_1}{\rho_2}\kappa^2 - \tfrac{1}{2}k_4^2 \\[2ex]
-\rho_1\omega^2 & k_3^2 M(1 + \alpha a_{32}) & k_3^2 M(\alpha + a_{23}) & 0 \\[2ex]
\rho_1\omega^2 & \begin{array}{c} a_{32}(2\mu\kappa^2 - k_3^2 H) \\ -k_2^2 \alpha M \end{array} & \begin{array}{c} 2\mu\kappa^2 - k_3^2 H \\ -a_{23}k_2^2 \alpha M \end{array} & -2\mu\nu_4\kappa^2 \\[2ex]
0 & a_{32}\nu_2 & \nu_3 & -\kappa^2 + \tfrac{1}{2}k_4^2
\end{bmatrix}
\begin{bmatrix}
\bar\phi_1 \\[2ex] \bar\phi_2' \\[2ex] \bar\phi_3' \\[2ex] \bar\phi_4
\end{bmatrix}
= \dfrac{e^{-\nu_1 z_0}}{\nu_1}
\begin{bmatrix}
\nu_1 \\[2ex] \rho_1\omega^2 \\[2ex] -\rho_1\omega^2 \\[2ex] 0
\end{bmatrix}
$$

Equation (6.24) is satisfied if

$$-\rho_1 \omega^2 \bar{\phi}_1 + k_2^2 M(1 + \alpha a_{1\,2}) \bar{\phi}_2' + k_3^2 M(\alpha + a_{2\,3}) \bar{\phi}_3'$$

$$= \frac{e^{-\nu_1 z_0}}{\nu_1} \tag{6.46}$$

where we have used $k^2 K_a = \omega^2 \rho_1$

With some rearrangement we now write equations (6.43) - (6.46) in matrix form:

$$[A] \{\bar{\phi}\} = \frac{e^{-\nu_1 z_0}}{\nu_1} \{S\}$$

This is shown in full in equation (6.47)
Using Cramer's rule the transformed potentials are

$$\bar{\phi}_1 = \frac{\Delta_1}{\Delta_0} \frac{e^{-\nu_1 z_0}}{\nu_1} \tag{6.48}$$

$$\bar{\phi}_2' = \frac{\Delta_2}{\Delta_0} \frac{e^{-\nu_1 z_0}}{\nu_1} \tag{6.49}$$

$$\bar{\phi}_3' = \frac{\Delta_3}{\Delta_0} \frac{e^{-\nu_1 z_0}}{\nu_1} \tag{6.50}$$

$$\bar{\phi}_4 = \frac{\Delta_4}{\Delta} \frac{e^{-\nu_1 z_0}}{\nu_1} \tag{6.51}$$

where Δ_0 is the determinant of the matrix $[A]$, and Δ_1, Δ_2, etc are the determinants formed by replacing the appropriate column with the vector S .

6.10   Solutions in integral form

Substitution of the transformed potentials into the general solutions

(6.25), (6.40) - (6.42) gives

$$\phi_1 = \int_0^\infty \frac{\Delta_1}{\Delta_0} \frac{e^{-\nu_1(z + z_0)}}{\nu_1} J_0(Kr) K dK \tag{6.52}$$

$$\phi_2 = \int_0^\infty \frac{\Delta_2}{\Delta_0} \frac{e^{-\nu_1 z_0 + \nu_2 z}}{\nu_1} J_0(Kr) K dK$$

$$+ a_{2,3} \int_0^\infty \frac{\Delta_3}{\Delta_0} \frac{e^{-\nu_1 z_0 + \nu_3 z}}{\nu_1} J_0(Kr) K dK \tag{6.53}$$

$$\phi_3 = \int_0^\infty \frac{\Delta_3}{\Delta_0} \frac{e^{-\nu_1 z_0 + \nu_3 z}}{\nu_1} J_0(Kr) K dK$$

$$+ a_{3,2} \int_0^\infty \frac{\Delta_2}{\Delta_0} \frac{e^{-\nu_1 z_0 + \nu_2 z}}{\nu_1} J_0(Kr) K dK \tag{6.54}$$

$$\phi_4 = \int_0^\infty \frac{\Delta_4}{\Delta_0} \frac{e^{-\nu_1 z_0 + \nu_4 z}}{\nu_1} J_0(Kr) K dK \tag{6.55}$$

where $z > 0$ for ϕ_1 and $z < 0$ for the other potentials.

These integrals are typical of those found in other two-media problems,

and we may consider them qualitatively in terms of saddle - point

integrals, branch cut integrals and poles in the complex k plane.

The saddle points occur at the stationary points of the oscillating

integrand, and for large Kr some of these correspond to the ray paths

governed by the laws of reflection and refraction. The remainder
consist of inhomogeneous waves (see Brekhovskikh [6.5]) for which
there is no definite path, but which can be interpreted in terms of
Snell's law by considering complex angles of incidence and refraction.

The branch cut integrals correspond to rays which are in part tied to
the interface. Some of the remaining parts of these paths are indefinite
since they consist of inhomogeneous waves, but again interpretation
is possible by allowing complex, as well as real, critical angles.

When a pole of the integrand lies between the contour of integration and
the real axis there will be a surface wave contribution. Nearby poles may
also affect the saddle-point integrals as in the rigid porous case.

The eventual contour of integration may not always consist of all
possible saddle-point and branch cut integrals. If the source and/or
receiver are sufficiently distant from the interface, a single saddle
path may enclose more than one branch point, thereby excluding any
separate contributions from the associated branch cut integrals.
Physically, this appears to eliminate any path which consists partly of
inhomogeneous waves and whose time of travel is less than the
corresponding wholly homogeneous path. At grazing angles, however,
each saddle path encloses a single branch point, and all possible
arrivals have to be considered.
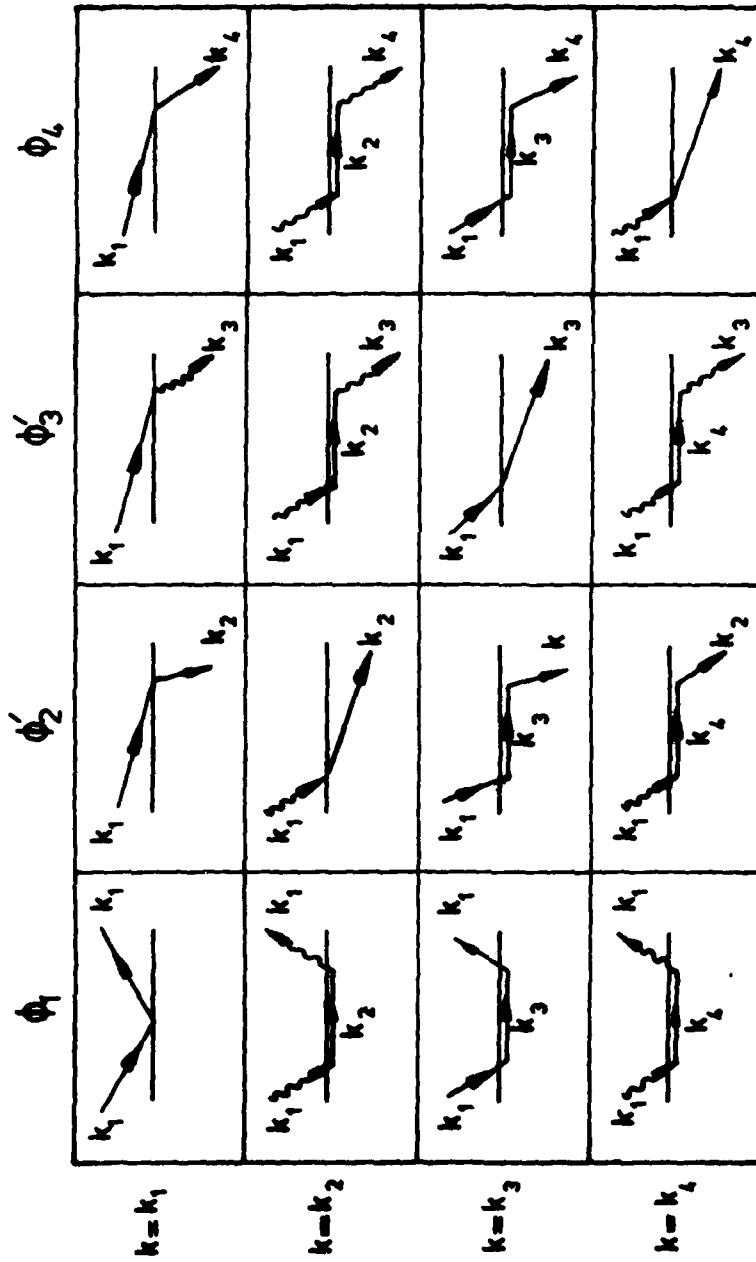
Figure 6.1 Ray-paths for wave-types possible at a fluid-poro-elastic solid interface

These considerations are summarised diagramatically in Fig.(6.1) in a manner closely following that given by Ewing et al [6.2] for a solid-solid interface. For this example we assume $k_2 > k_4 > k_1 > k_3$. The wavy lines denote inhomogeneous waves, and in general two-part paths from branch cut integrals. The potential ϕ_2' is associated purely with the slow wave and the potential ϕ_3' with the fast wave, so that in equations (6.53),(6.54) we could write

$$\phi_2 = \phi_2' + a_{23}\phi_3', \quad \phi_3 = \phi_3' + a_{23}\phi_2'$$

In addition to these arrivals, of course, there may be surface wave contributions.

It can be seen from the diagram that when the receiver is on the interface, the four paths for each branch point associated with the four different wave potentials coalesce into a single path. This reduces the total number of paths, excluding surface waves, from sixteen to four, and this is a useful simplification when we consider motion of the ground surface. Expressions for this are derived in Appendix 5.

LITERATURE CITED

[6.1]   M. A. Biot.   Mechanics of Deformation and Acoustic Propagation
        in Porous Media. J. of Applied Physics 1961 33(4).

[6.2]   W.M. Ewing, W.S. Jardetsky and F. Press.
        Elastic Waves in Layered Media 1957 McGraw-Hill

[6.3]   S. Feng and D. L. Johnson
        High Frequency Acoustic Properties of a Fluid/Porous Solid
        Interface.   I. New Surface Mode
        J. Acoust. Soc. Amer. $\underline{74}$ (3)   906-914 (1983).

[6.4]   S. Feng and D. L. Johnson.   High Frequency Acoustic Properties
        of a Fluid/Porous Solid Interface.   II The 2D Reflection Green's
        Function.   J. Acoust. Soc. Amer. $\underline{74}$ (3) 915-924 (1983)

[6.5]   L. M. Brekhovskikh.   Waves in Layered Media 1980 Academic Press.

CHAPTER 7

CONCLUDING REMARKS

7.1 Although we have been able to predict qualitative features of
     some existing data on acoustic-to-seismic coupling, in particular,
     that used to compute intensity ratios (Chapter 5), the requirement
     for design of unattended seismic and acoustic sensor logic remains
     that good quantitative agreement with these ratios should be obtained
     and that there should be theoretical agreement with other data on
     acoustic-to-seismic coupling [7.1]. These data include the results
     of tests using impulsive acoustic sources above and below the surface
     and sensors at depths of up to 1.5 m.

7.2 The main obstacles to such requirements at this stage are lack of
     information on the frame elastic constants required to characterise
     poro-elastic soils (Chapter 5) and the complex-layered and possibly
     anistropic structure of real grounds.

7.3 The analysis has shown that surface particle velocity prediction
     is particularly sensitive to the value chosen for the frame rigidity
     modulus.

7.4 The model developed in this work has been brought to the stage where
     numerical predictions of coupling from above-ground point acoustic
     sources to sub-surface geophones are possible in certain well-defined
     situations viz. near-surface sources and air-saturated, isotropic,
     porous ground of infinite depth. Alternatively, if the acoustic
     source is sufficiently far removed from the ground surface for the
     incident sound waves to be treated as plane, then not only can
     predictions be made of the coupling to the surface of semi-infinite
     ground but also to ground in the form of a hard-backed porous layer.

7.5 Extension of this model to allow for anistropy and for more complicated ground structures and continuous sources will be straight forward albeit sufficiently algebraically cumbersome to warrant a semi-numerical approach, such as that adopted by the Fast Field Program and its successors in Underwater Acoustics.

7.6 Further extension of the model to allow for impulsive rather than continuous sources, should also be possible using a numerical approach as suggested recently by Feng and Johnson [7.2].

7.7 The model may also be extended to include the effects of partial water-saturation of poro-elastic soils along the lines suggested by Brutsaert [7.3].

7.8 Finally, it should be noted that the theories developed in this report are applicable to seismic disturbance of poro-elastic ground by direct mechanical contact. Consequently it is possible to envisage prediction and analysis of seismic refraction results in a way that differs from established methods. Furthermore the possibility arises of the prediction of ground vibration due to road and rail vehicles in terms of basic fundamental attributes of intervening terrain.

REFERENCES

[7.1]   K. Attenborough   Draft chapter on Acoustic-to-Seismic coupling
for NATO A/C Panel III RSG-II   Final Report (1983)

[7.2]   S. Feng and D.L. Johnson   High Frequency Acoustic Properties
of a Fluid/Porous Solid Interface II. The 2D Green's Function
J. Acoust.Soc.Am.   74(3) 915-924. September 1983.

[7.3]   W. Brutsaert   The Propagation of Elastic Waves in Unconsolidated
Unsaturated Granular Mediums   J. Geophys.Res. 69 (2)   243-257
(1964)

APPENDIX 1

WEYL - VAN DER POL FORMULA -- CONFIRMATION

The method of steepest descents has been employed extensively to obtain
a computationally feasible solution for the field from a point source
of sound in air above a locally reacting ground plane. Various
mathematical approaches which arrive at the above solution under various
approximations are listed in reference [1].

The important case of near grazing incidence requires   additional care while
handling the steepest descent integrals and this is chiefly achieved by a
method known in the literature [2] as subtraction of the pole. This method
often leads to laborious calculations. A simple alternative solution can
be obtained by an appropriate application of the method of stationery phase. In
general, the method of stationary phase yields useful approximation as long
as the integrand is a slowly varying function of irtegration variables in the
neighbourhood of the stationary point. After a suitable choice of integration
variables, the integrals are approximated in the usual way and the final results
for the reflected field confirm those obtained previously.

The physical problem under consideration can be formulated in terms of the following
boundary value problem. For convenience, we choose a cartesian coordinate system
The acoustic velocity potential satisfies Helmholtz wave equation in both the
media ($z < 0$ and < 0) which are characterised by their densities ρ_1 and ρ_2
and propagation constants κ_1 and κ_2, respectively. Thus we have,

$$(\nabla^2 + \kappa_1{}^2)\psi = \delta(x)\ \delta(y)\ \delta(z-z_0)\quad,\quad z>0 \tag{A1.1}$$

$$(\nabla^2 + \kappa_2{}^2)\psi = 0 \quad\quad\quad,\quad z<0$$

where $\kappa_1 = k_1 + is_1$ and $\kappa_2 = k_2 + is_2$ and the source term is symbolically represented by Dirac delta function. The time dependence of exp $(-i\omega t)$ is suppressed throughout. The boundary conditions under consideration are continuity of pressure and normal velocity across the interface $z = 0$ i.e.

$$\rho_1\psi(x,y,0-) = \rho_2\psi(x,y,0+) \tag{A1.2}$$

and

$$\frac{\partial}{\partial z}\psi(x,y,0-) = \frac{\partial}{\partial z}\psi(x,y,0+)$$

By making use of two dimensional Fourier transform in space variables x and y we obtain the following for the reflected field $z > 0$.

$$\psi = \frac{e^{-ik_1R_1}}{4\pi R_1} + \frac{1}{4\pi^2}\int_{-\infty}^{\infty}e^{i\alpha x}\,d\alpha\int_{-\infty}^{\infty}\frac{1}{2i\chi_1}\frac{\rho_2\chi_1 - \rho_1\chi_2}{\rho_2\chi_1 + \rho_1\chi_2}$$

$$\times\ e^{-i\chi_1(z + z_o)\ +i\beta y}\,d\beta$$

where α and β are transform variables and $\chi_{1,2} = \sqrt{\kappa_{1,2}^2 - \alpha^2 - \beta^2}$. $\quad$ (A1.3)

The square root functions are defined in such a way that

$\chi_{1,2} = \sqrt{\kappa_{1,2}^2 - \alpha^2}$ when $\beta = 0$ and $\kappa_{1,2}$ when $\alpha = 0$. The integral in (2.3) can be approximately evaluated for large source - receiver

distances by the method of stationary phase and we obtain

$$\int \quad = \quad \frac{R(\theta)}{4\pi} \; \frac{e^{-ik_1 R_2}}{R_2}$$

where

$$R_2^2 \quad = \quad x^2 + y^2 + (z + z\,)^2$$

$$R(\theta) \quad = \quad \frac{\cos\theta - M\sqrt{n^2 - \sin^2\theta}}{\cos\theta + M\sqrt{n^2 - \sin^2\theta}}$$

and $M = \rho_1/\rho_2$ and $n = \kappa_2/\kappa_1$. The above asymptotic approximation
is of limited use and breaks down when θ is near $\pi/2$ and this is
due to the fact that the integrand in (A1.3) no longer remains a
slowly varying function, but will oscillate rapidly between -1 to $+1$
In this case, $(\theta = \pi/2)$, the contribution from the stationary point
has to be considered more carefully. In order to facilitate this
computation, we rewrite the integral in (A1.3) as

$$\frac{e^{-ik_1 R_2}}{4\pi R_2} \; + \; \psi^{(1)}$$

where

$$\psi^{(1)} = \frac{1}{4\pi^2} \int_{-\infty}^{\infty} e^{i\alpha x}\,d\alpha \int_{-\infty}^{\infty} \frac{\rho_1 X_2}{X_1(\rho_2 X_1 + \rho_1 X_2)} \, e^{-iX_1(z-z_o)+i\beta y} \, d\beta$$

$$(A1.4)$$

The integration is performed successively, first with respect to
(from now on abreviated as w.r.t.) β and then w.r.t. α. The integral
w.r.t. β is evaluated after deforming the contour into the complex β
plane and then approximating the resulting integral by the method of
stationary phase.

This is accomplished by first observing the branch point and pole
singularities of the integrand in the complex β plane. In the
present case the integrand has branch points at

$$\beta = \pm \sqrt{\kappa_2^2 - \alpha^2} \quad \text{and simple poles at } \beta = \pm \sqrt{\frac{(1-M^2 n^2)}{(1-M^2)} \kappa_1^2 - \alpha^2}$$

The integrand is made single valued by introducing the branch cuts
as shown in Fig. A1.1.
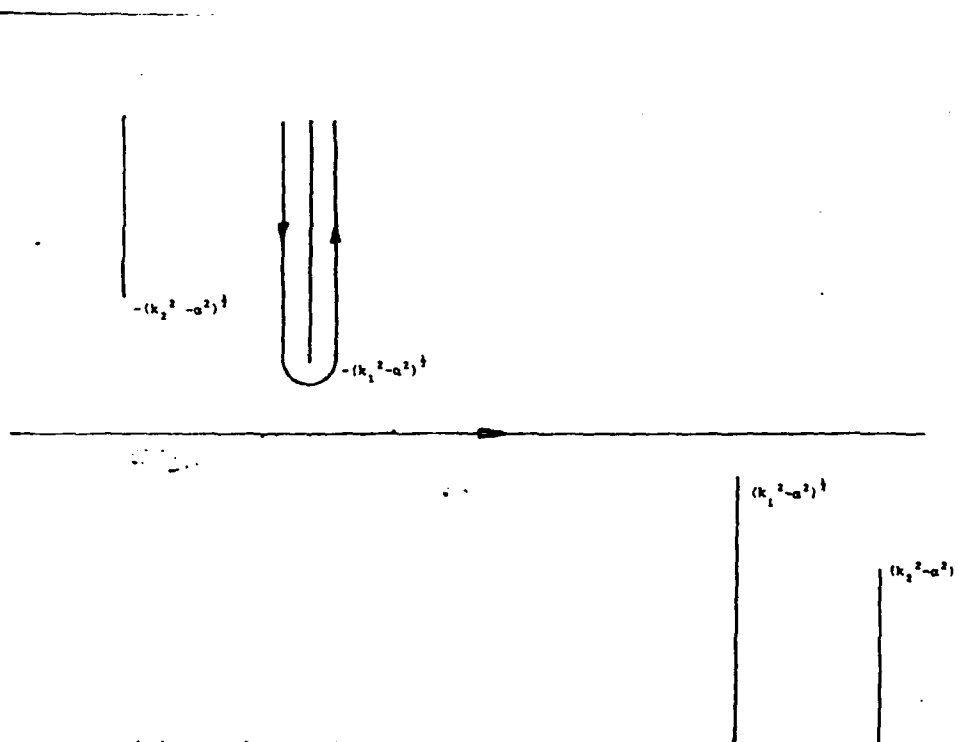
FIGURE A1.1 Branch cuts in the complex-β plane

The deformed contour consists of two circular arcs of large
radius going round the branch cuts. The contribution from the
circular arcs is zero. The contribution from the branch point
$-(\kappa_2^2 - \alpha^2)^{\frac{1}{2}}$ can be shown to be

$$O\left[\exp\{-i(\kappa_1^2 - \alpha^2)^{\frac{1}{2}} (z+z_0) - i (\kappa_2^2 - \alpha^2)^{\frac{1}{2}} y\}\right]$$

and will be neglected. Thus we are left with the following integral

$$\int_C \frac{\rho_1 X_2}{X_1 (\rho_2 \kappa_1 + \rho_1 X_2)} e^{-iX_1 \nu_1 \cos\theta_1 + i \beta\nu_1 \sin\theta_1} d\beta$$

$$(A1.5)$$

where we have let $y = r_1 \sin\theta_1$, $z + z_0 = r_1 \cos\theta_1$ in A1.5 and
C is the contour round the branch point $- (\kappa_1^2 - \alpha^2)^{\frac{1}{2}}$. This
integral is approximately evaluated by the method of stationary
phase. The exponent in A1.5 has a stationary point at
$\beta = - \sqrt{\kappa_1^2 - \alpha^2} \sin\theta_1$. When $\theta \sim \pi/2$, the situation we are
interested in, we observe that the stationary point is in close
proximity of the branch point $- \sqrt{\kappa_1^2 - \alpha^2}$.

Now the main contribution to the integral arises from the neighbourhood
of stationary point, in that part of the integrand which is slowly
varying. The case where the integrand is not slowly varying has to
be considered separately. In order to do this, we first rewrite (A1.5) as

$$-\tfrac{1}{2} \{R_\nu(\alpha,\theta_1) - 1\} \{\sqrt{\kappa_1^2 - \alpha^2} \cos\theta_1 + \kappa_1 A\} \, x$$

$$x \int_c \frac{e^{-i X_1 (z+z_0)+i\beta y}}{X_1 (X_1+\kappa_1 A)} \, d\beta \qquad (A1.6)$$

where $A = M \sqrt{\dfrac{n^2-1}{1-M^2}}$ and

$$R_v(\alpha,\theta_1) = \frac{\rho_2 X_1 - \rho_1 X_2}{\rho_2 X_1 + \rho_1 X_2} \Bigg| \quad \text{at } \beta = -\sqrt{\kappa_1^2 - \alpha^2} \sin \theta_1$$

Now we write

$$X_1 = \sqrt{\kappa_1^2 - \alpha^2 - \beta^2} \quad = \quad \left(\sqrt{\kappa_1^2 - \alpha^2} + \beta\right)^{\frac{1}{2}} \left(\sqrt{\kappa_1^2 - \alpha^2} - \beta\right)^{\frac{1}{2}}$$

In the neighbourhood of the stationary point, the second factor is slowly varying and we put $\beta = -\sqrt{\kappa_1^2 - \alpha^2}$ (as $\theta_1 \sim \pi/2$).
On the remaining integrand, we put

$$\left\{ \sqrt{\kappa_1^2 - \alpha^2} + \beta \right\}^{\frac{1}{2}} = \sqrt{2} \, e^{i\pi/4} \, \tau$$

where τ is a real parameter and varies from $-\infty$ to $+\infty$ on C.

After some algebra, we have from (A1.6)

$$\left(R_v(\alpha,\theta_1) - 1 \right) \left(\cos \theta_1 + \kappa_1 (\kappa_1^2 - \alpha^2)^{-\frac{1}{2}} A \right)$$

$$x \exp \{ - iy_1 \sqrt{\kappa_1^2 - \alpha^2} \ (1 + \tfrac{1}{2} \cot^2 \theta_1] \ \} \quad x \ I \ (2r_1 \sin \theta_1) \qquad \text{(A1.7)}$$

where

$$I(u) = \int_{-\infty}^{\infty} \frac{e^{-t^2 u}}{t + b} \, dt$$

and

$$b = \tfrac{1}{2} e^{-i\pi/4} \ \{ (\kappa_1^2 - \alpha^2)^{\tfrac{1}{2}} \cot \theta_1 + \kappa_1 A \ (\kappa_1^2 - \alpha^2)^{-\tfrac{1}{2}} \} \qquad \text{(A1.8)}$$

The integral defined by I(u) can be expressed in closed form involving error function complement and we can write it as

$$I(u) = - \sqrt{8\pi} \exp (-i\pi/4) \, . \, F(b \exp (i \, \pi/4) \, \sqrt{u})$$

Thus we have from (A1.4) and (A1.7),

$$\psi^{(1)} \simeq \frac{i}{4\pi^2} \int_{-\Psi}^{\Psi} e^{i\alpha x - iy \sqrt{\kappa_1^2 - \alpha^2} (1 + \tfrac{1}{2} \cot^2 \theta_1)}$$

$$x \ (\cos \theta_1 + \kappa_1 (\kappa_1^2 - \alpha^2)^{-\tfrac{1}{2}} A) \ I (2r_1 \sin \theta_1] \, d\alpha \qquad \text{(A1.9)}$$

In the present case of interest $y(1 + \frac{1}{2} \cot^2 \theta_1) \approx y \approx r_1$ since $\cos \theta_1$ is small. The final evaluation of $\psi^{(1)}$ is carried out by a further application of method of stationery phase. Now the integral $I(2r_1 \sin\theta_1)$ does not contribute to the exponential and the stationary point of $\alpha x - r_1 \sqrt{\kappa_1^2 - \alpha^2}$ occurs at $\alpha = -\kappa_1 x/(x^2 + r_1^2)^{\frac{1}{2}}$. The relevant terms at this point are given by

$$\sqrt{\kappa_1^2 - \alpha^2} = \frac{\kappa_1 r_1}{R} = \frac{\kappa_1 \cos \theta}{\cos \theta_1} = \frac{\kappa_1 y}{R \sin \theta_1}$$

since $\sin \theta_1 \approx 1$

$$b = 0.5 \exp(-i \pi/4) \{A + \cos \theta\} \sqrt{\frac{\kappa_1 R}{r_1}}$$

From (A1.3), (A1.4) and (A1.9), we finally obtain for the reflected field in $z > 0$ as

$$\psi = \frac{e^{-i\kappa_1 R_1}}{4\pi R_1} + \frac{e^{-i\kappa_1 R_2}}{4\pi R_2} \{ 1 + 2i\gamma (R(\theta) -1) F(\gamma) \} \qquad (A1.10)$$

where $\gamma = \sqrt{\frac{1}{2}\kappa_1 R_2} (A + \cos \theta)$

$$A = M \sqrt{\frac{n^2 - 1}{1 - M^2}} \approx \beta \quad \text{when } |\eta|^2 \gg 1 \text{ and } |M|^2 \ll 1$$

and $F(a) = \exp(ia^2) \int_a^\infty \exp(-it^2) \, dt$

After some simple algebra the above solution for the reflected field is easily shown to be equivalent to those previously obtained.

LITERATURE CITED

[A1.1]   K. ATTENBOROUGH. S.I. HAYEK and J. M. LAWTHER.

         "Propagation of sound above a porous half space."

         J. Acoust. Soc. Amer. 68, 1493-1501 (1980).

[A1.2]   A. BANOS. Dipole radiation in the presence of a conducting

         half space. Pergamon Press. Oxford (1966).

[A1.3]   C.F. CHIEN and W.W. SOROKA, "Sound propagation over an

         impedance plane". J. Sound and Vib. 43.9-20 (1975).

[A1.4]   B. FRIEDMAN. Principles and Tehcniques of applied mathematics.

         John Wiley. New York (1956).

[A1.5]   A. E. HEINS and H. FESHBACH. "On the Coupling of two

         half planes". Proc. of Symposium in Applied Math.V

         McGraw-Hill (1954). p.75-87.

APPENDIX 2

ON THE ACOUSTIC SURFACE WAVE NEAR A RIGID POROUS BOUNDARY

A spherical wave incident upon an interface of two media, in particular,
air and porous ground gives rise to reflected and refracted waves subjected
to Snell's law. Under certain circumstances, the interface can support
a wave which is exponentially damped in the normal direction and whose
amplitude decays as $r^{-\frac{1}{2}}$. This wave is termed as a surface wave.

In this section, we clarify certain mathematical details which are necessary
for the existence of a surface wave. We also provide an alternative
interpretation for the acoustic surface wave in terms of discrete spectrum
of a suitable partial differential operator.

We consider an incident spherical sound wave

$$\frac{e^{iR_1 R_1}}{4\pi \ R_1}$$

with time dependence of the form exp $(-i\omega t)$, incident upon a locally
reacting boundary. For the above case, surface waves are conveniently
analysed by expressing the reflected field as a Fourier integral.
The pole(s) of the reflection coefficient (in Fourier domain) are
closely related to surface wave(s). The computation of the reflected
field crucially depends upon the evaluation of the following integral

$$\phi(H,r) = \frac{\rho_2}{2\pi} \int_{\infty}^{\infty} \frac{e^{-\nu_1 H}}{\rho_2 \nu_1 + \rho_1 \nu_2} J_0(Kr) K \, dK \qquad (A2.1)$$

where $\nu_{1,2} = \sqrt{K^2 - k^2}$ and $\rho_{1,2}$ are densities of the media $z > 0$ and $z < 0$ respectively and $H = z + z_0$. The square root functions are defined in such a way that $\sqrt{K^2 - k_{1,2}^2} = i\, k_{1,2}$ as $K \to 0$.*

Due to the presence of branch point singularities in the integrand of (A2.1) it is important to define the branch cuts before analysing the existence of poles. The choice of branch cuts is arbitrary as long as $\text{Re } \nu_{1,2} > 0$ to ensure the convergence of the integral in (A2.1). Essentially two types of branch cuts are used in the literature viz, vertical and hyperbolic [1] branch cuts. Here we consider the case of vertical branch cuts and the analysis for hyperbolic branch cuts follows on similar lines.

The vertical branch cuts are defined by $\text{Re } K = \pm \text{ Re } k_1$, $\text{Im } K > 0$ and $\text{Re } K = \pm k_2$, $\text{Im } K > 0$. Corresponding to each square root function, there are two choices for the sign of $\text{Re } \nu_1$ and these are shown in table A2.1.

TABLE A2.1

	Re ν_1	Re ν_2
I	+	+
II	−	+
III	+	−
IV	−	−

*$k_{1,2}$ are complex constants with non zero imaginary points

We write $\nu_i = |\nu_i| \exp [i \arg(\nu_i)]$, for $i = 1,2$ and the sign of Re ν_i depends on the variations in arg (ν_i). We consider these variations by considering a small neighbourhood around the branch points k_1 and k_2

TABLE A2.2

θ	Arg $\nu_1(K)$	θ	Arg $\nu_2(K)$
$-3\pi/2$	$-3\pi/4 + \chi_1/2$	$-3\pi/2$	$-3\pi/4 + \chi_2$
$-\pi - \chi_1$	$-\pi/2$	$-\pi - \chi_2$	$-\pi/2$
$-\pi + \chi_1$	$-\pi/2 + \chi_1$	$-\pi + \chi_2$	$-\pi/2 + \chi_2$
$-\chi_1$	0	$-\chi_2$	0
χ_1	χ_1	χ_2	χ_2
$\pi/2$	$\pi/4 + \chi_1$	$\pi/2$	$\pi/4 + \chi_2$

where χ_1 is arg k_1 which is small as k_1 is essentially real and χ_2 is arg k . Clearly on sheet I,

$$-\pi/2 + \chi_1 < \arg \nu_1(K) < \pi/4 + \chi_1$$

and

$$-\pi/2 + \chi_2 < \arg \nu_2(K) < \pi/4 + \chi_2.$$

Now we consider the possible existence of poles on the upper Riemann sheet. It is easily seen that the poles of the integrand in (A2.1) are given by the equation

$$\rho_2 \nu_1 + \rho_2 \nu_2 = 0$$

i.e.

$$K = \pm k_1 [(1 - M^2 n^2) / (1 - M^2)]^{\frac{1}{2}} \qquad (A.2.2)$$

where $M = \rho_1/\rho_2$ and $n = k_2/k_1$. In order to locate these poles in the first quadrant, we define the complex number

$$K_0 = k_1 [(1 - M^2 n^2) / (1 - M^2)]^{\frac{1}{2}}$$

For most of the grounds of practical interest $|M^2| \ll 1$ and we approximate $(1 - M^2)^{\frac{1}{2}} \simeq 1$. Hence $K_0 = k_1 (1 - M^2 n^2)^{\frac{1}{2}}$

We also write the complex number $nM = |nM| \exp (i\psi)$. It is readily shown that

$$K_0 = k_1 [1 + |nM|^4 - 2 |nM|^2 \cos 2\psi]^{\frac{1}{4}} \qquad (A2.3)$$

and

$$\arg(K_0) = \arg(k_1) + \tfrac{1}{2}\arg (1 - n^2 M^2)$$

$$= \chi_1 + \tfrac{1}{2}\tan^{-1} \frac{|nM|^2 \sin 2\psi}{|nM|^2 \cos 2\psi - 1} \qquad (A2.4)$$

Since $\chi_1 > 0$ and $K_0 > |k_1|$, the pole lies to the right of the branch point k_1 as shown on Fig A2.1. In order to verify that the equation for the pole is really satisfied at K_0, we compute $\nu_1(K)$ and $\nu_2(K)$ at K_0.

$$\nu_1(K_0) = \pm i\chi_1 nM \quad \text{and}$$

$$\arg\{\nu_1(K_0)\} = \pm \pi/2 + \arg (k_1) + \arg (nM)$$

where the choice of sign is fixed depending on the Riemann sheet. Now $\arg (k_1)$ is a small positive quantity and $\arg (nM) \simeq -\pi/4$ for a porous material at low frequencies and for K_0 situated as shown in Fig. A2.1.

$$\chi_1 \le \arg \nu_1(K_0) \le \pi/4 + \chi_1$$

on the upper Riemann sheet and hence $\nu_1(K_0) = + ik_1 nM$.

Similarly,

$$\nu_2(K_0) = \pm ik_1 n$$

where $|n|^2$ is assumed large; and

$$\arg \nu_2(K_0) = \pm \pi/2 + \arg (k_1) + \arg (n)$$

Now, for K_0 lying to the left of the branch point k_2, we have

$$-\pi/2 + \chi_2 < \arg \nu_2(K_0) < 0$$

Since $\arg (k_2) > \arg (k_1)$, we have on sheet I,

$$\nu_2(K_0) = - ik_1 n$$

Thus it is evident that on sheet I, the equation for the pole is satisfied and hence K_0 is a *real* pole on sheet I.
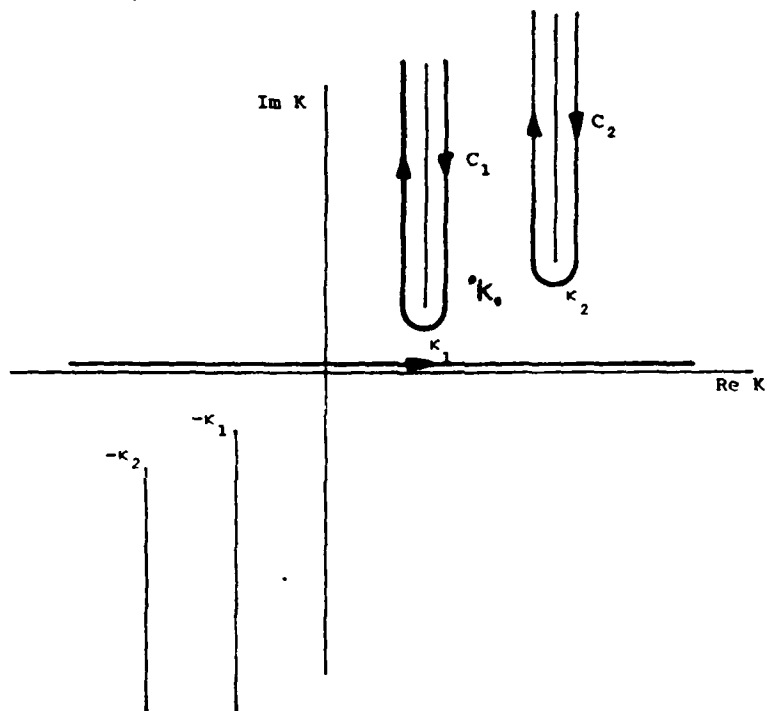
Fig A2.1.

Fig. A2.2 Location of pole and branch cuts

Now the evaluation of the integral is accomplished by first extending the range of integration from 0 to ∞ to $-\infty$ to $+\infty$, and deforming the contour into upper half plane of cut K - plane which encloses the pole at K_o. The branch cut integrals are approximated using the saddle point method and the residue term represents the surface wave

$$\text{residue at } K_o = \frac{Aik_1 \exp(-ik_1 HA)}{(1-M^2)\ 4\pi}\ H_o^{(1)}(k_1 r \sqrt{1-A^2}\ )$$

where

$$A = M[(n^2 - 1) / (1 - M^2)]^{\frac{1}{2}}$$

For the sake of completeness we quote the final expression for the reflection field in $z > 0$.

$$\phi_{ref} \quad \frac{e^{ik_1 R_1}}{4\pi R_1} + \frac{e^{ik_2 R_2}}{4\pi\ R_2}\left\{ R\ (\theta_o) + \frac{2i(1 + \beta\ \cos\theta_o)}{k_1 R_2(\beta + \cos\theta_o)^3} - \frac{iN}{k_1 R_2} + 0(R_2^{-2}\ ; \right\}$$

$$+ \text{ residue at the pole.}$$

where

$$N = \frac{1}{2}[R''\ (\theta_o) + R'\ (\theta_o)\ \cot\ \theta_o\ ]$$

$$R(\theta_o) = (\cos\theta_o - \beta) / (\cos\ \theta_o + \beta\ )$$

$$\beta = Mn$$

At this stage it is worth mentioning that the above solution is of limited practical use. For a solution which is uniformly valid for all angles of incidence a modified solution is used as described in previous section (see Eq.(A1.10)), or by a similiar method [A1.1]. In this case, the surface wave term appears implicitly through error function complement, which can be seen more clearly for large arguments of the function (see Eq. 52 in [A1.1]).

A simple interpretation for the surface wave can be given in terms of the discrete spectrum of a suitable partial differential operator. In the present case it suffices to consider a two dimensional model for ease óf illustration, where x and z coordinates denote the horizontal seperation and vertical distance from the origin respectively.

We are required to find a function $\phi(x,z)$ such that

$$\phi_{xx} + (k^2 - L)\phi = \delta(x)\,\delta(z - z_o) \tag{A2.5}$$

where $L\phi = -\phi_{zz}$, over the half plane $-\infty < x < \infty$, $0 < z < \infty$, such that

$$\phi_z(x,0) + \alpha\phi(x,0) = 0 \tag{A2.6}$$

where α is a paramenter related to impedance and $\mathrm{Re}\,\alpha > 0$. Also we require the field to be outgoing at infinity.

The solution for A2.5 can be written symolically as

$$\phi(x,z) = \frac{\exp\left(i\sqrt{k^2 - L}\,\,|x|\right)}{2i\sqrt{k^2 - L}}\,\delta(z - z_o) \tag{A2.7}$$

This operator espression can be evaluated, once we know the spectral representation for L under the above boundary condition . This can be obtained easily by the well known methods [A.4] and we have

$$\delta(z - z_o) = 2\alpha\,\exp(-\alpha(z + z_o))\,[1 - H(\mathrm{Re}\,\alpha)]$$

$$-\frac{i}{\pi}\int_{-\infty}^{\infty}\frac{\exp\left[i\rho(z - z_o) + i\sqrt{k^2 - \rho^2}\,|x|\right]}{\sqrt{k^2 - \rho^2}}\,d\rho$$

$$-\frac{i}{\pi}\int_{-\infty}^{\infty}\frac{\exp\left[i\rho(z + z_o) + i\sqrt{k^2 - \rho^2}\,|x|\right]}{\sqrt{k^2 - \rho^2}}\,\frac{\rho - i\alpha}{\rho + i\alpha}\,d\rho \tag{A2.8}$$

Now from A2.7 and A2.8

$$-\phi(x,z) = \frac{-i\,\alpha\,\exp\left(i\sqrt{k^2 + \alpha^2}\,|x|\right)\,\exp[-\alpha(z + z_o)]}{\sqrt{k^2 + \alpha^2}}$$

$$-\frac{i}{\Pi}\int_{-\infty}^{\infty}\exp\left(i\rho(z - z_o) + i\sqrt{k^2 - \rho^2}\,|x|\right)\frac{d\rho}{\sqrt{k^2 - \rho^2}}$$

$$-\frac{i}{\Pi}\int_{-\infty}^{\infty}\exp\left(i\rho(z + z_o) + i\sqrt{k^2 - \rho^2}\,|x|\right)\frac{\rho - i\alpha}{\rho + i\alpha}\frac{d\rho}{\sqrt{k^2 - \rho^2}} \qquad (A2.9)$$

In Eq. the first term arises from a pole of the Green's function and in the literature, is referred to as constituting the discrete spectrum of the operator L. The remaining two integrals, after some algebra, can be easily seen to be contributing to the continuous spectrum. In fact, they can be shown to be direct (first integral in $(A2.9)$) and reflected (second integral in A2.9 waves. In other words we notice that the branch point singularities of Green's function give rise to space waves, while pole singularities give rise to surface wave(s).

APPENDIX 3

THE ACOUSTIC MODELLING FACILITY

Introduction

This Appendix introduces the basic rules of acoustic modelling
and discusses the essential requirements of the modelling
instrumentation. It concludes with a description of a series
of model experiments, conducted in a small anechoic chamber,
to measure the amplitude ratio of the direct and transmitted
sound fields above a porous half-space and the delay between
the arrival of the direct and transmitted sound waves.

A3.1 Basic modelling rules

In order to model an acoustic sound path, two conditions must
be fulfilled. The first is that of geometric similarity and
the second kinematic similarity. Geometric similarity ensures
that the ratio of the wavelength of the sound source to the
dimensions of any bodies or reflecting surfaces remains constant
and hence diffraction effects will be replicated in the model.

Kinematic similarity is required due to the fact that air is
used as the propagation medium in both the full scale and model
environments and hence the velocity of sound is a constant. This
imposes a time scale factor, as can be shown by considering the
dimensionless quantity characterising reference times (the
Thomson Number) as follows:

$$\frac{T_m \cdot V_m}{L_m} = \frac{T_o \cdot V_o}{L_o}$$

where T,V and L are time, velocity and length respectively and
the subscripts m and o refer to the original and model propagation
paths. Since $V_m = V_o$ then

$$\frac{T_m}{T_o} = \frac{L_m}{L_o}$$

and the time scale factor equals the length scale factor. Thus
maintaining a constant sound velocity requires that the model
frequencies be increased with respect to those of the original
and that all time periods be scaled downward.

In general the scale factor derived for the condition of geometric
similarity must also be applied to the acoustic properties of
the materials used to reconstruct the surfaces and obstructions
in the model; so that the impedance at the model frequencies
equals that at the full scale frequencies.

The prime objective of the model experiments conducted during
this study was to evaluate theoretical predictions of the
coupling between the airborne and seismic waves, rather than to
obtain quantitative data of a precise ground surface. In view
of this it was felt unnecessary to employ 'scaled' models and so no
attempt was made to scale the acoustic properties of the model
ground surface.

A3.2 Requirements of a model receiver

The basic requirements of a model receiver are small size, high
sensitivity and wideband frequency response. Size is important
for two reasons (a) because directivity is related to the ratio
of diaphragm diameter to wavelength and hence a small microphone
better approximates an omni-directional receiver and (b) because
the reduction in diaphragm mass improves the high frequency response
of the microphone. The major disadvantage of a small diameter is
that the reduction in surface area reduces the microphone's
sensitivity.

The receivers used for the model experiments were commercial
1/4 inch diameter condenser microphones manufactured by Bruel
and Kjaer (B & K) of Denmark. The sensitivity and bandwidth
of typical microphones are shown in Table A3.1

Table A3.1 Microphone sensitivity and bandwidth

Microphone type	Nominal diameter	Sensensitivity mV/Pa	Bandwidth kHz
B & K 4136	1/4"	4	70
B & K 4138	1/8"	1	140

Figures A3.1 - A3.4 show the directivity of these microphones at
various frequencies, measured both with and without a protection
grid [A3.1]. Although the 1/8" displays a wider bandwidth and
superior directivity, its low sensitivity limited the maximum
length of the model propagation path to less than 1 metre.

In view of this the 1/4" microphone was adopted as the standard
receiver and the 1/8" microphone was used primarily to test
the performance of the 1/4" at short separation distances. The
1/8" microphone was also used to measure the directivity of the
sound sources.

A3.3   Requirements of a model sound source

The sound source should be omni-directional, have a wideband frequency
response and generate adequate signal power.

Model sound sources fall into two categories, continuous and
impulsive. The impulsive source, such as an electrical spark,
generates a short energy pulse of high acoustic intensity and
wide bandwidth which propagates along an infinite number of paths.
Each path can be identified by the time delay between the energy
discharge and the arrival of the pulse at the receiver, hence there
is no need for special anechoic measurement environments.

The major limitation of the impulsive source is the possibility
of non-linear acoustic propagation near the vicinity of the
source, which imposes a minimum length of propagation path.
Furthermore, they require sophisticated measurement and analysis
systems to cope with the problems of direct and reflected pulse
overlap [A3.2].

Continuous sources can be handled with relatively simple measurement
systems, but since the energy is radiated continuously, it is not
possible to identify individual propagation paths. This means that
all measurements must be conducted within an anechoic environment.

A3.4   Model sound sources

Two sources were selected for the model experiments. The first
was the air jet described by Delany et al [A3.3] and shown in
Figure A3.5. Measurements of the directivity in both the vertical
and horizontal planes indicate that this design is a good
approximation to an omni-directional source at frequencies up to
100 kHz. One particularly important feature of this design is its
excellent long term stability, so that over a period of six
months the one third octave spectrum varied by less than 0.5 dB.

The useful bandwidth of this source is 1-100 kHz, as dictated
by the signal to noise ratio of the measurement system and the
low frequency performance of the anechoic chamber. Figure A3.6
shows the free-field spectrum measured at a distance of 100 cm.

The second model sound source was a spark discharge device designed
at the Open University. (A complete description of the design
and operating characteristics is given in reference A3.2)

The spark operates at very low energy levels and so non-linear
propagation effects are virtually eliminated. A further
advantage of the low energy is the fact that electromagnetic
radiation is kept below levels that can be detected by the
condenser microphones. A typical spark source spectrum is
shown in Figure A3.7.

A3.5   Modelling instrumentation

A3.5.1   Dynamic range

Acoustic modelling is very demanding of instrumentation systems.
The low sensitivity of small microphones requires that pre-amplifiers
and main amplifiers have very low electrical noise floors over a very
wide frequency range.

A typical microphone amplifier chain consists of a pre-amplifier,
to convert the high output impedance of the microphone to a
low impedance suitable for driving long cables, and a measuring
amplifier to provide the polarization voltage and the gain.

An estimate of the dynamic range of the instrumentation system can
be obtained by calculating the noise floor of the amplifiers
and subtracting this value from the input signal level. The
following figures are taken from the relevant manufacturers'
specifications.

(a)   Pre-amplifier noise
       The inherent noise of the pre-amplifier is determined by the
       capacitance of the microphone cartridge. For a 1/4"
       microphone the total noise over the range 20-20 000 Hz
       is quoted as less than 120 microvolts.

(b) Main amplifier noise

The noise floor of the main amplifier is determined by the thermal noise of the electronic components. The signal to noise ratio for a 100 mV input is stated to be better than 100 dB, which implies a noise floor of 1 microvolt over the range 20-20 000 Hz.

Assuming that the main amplifier noise can be neglected, compared to the pre-amplifier noise, then the equivalent sound pressure level of the noise floor is 63.5 dB.

If non-linear propagation effects are to be avoided, then the maximum source sound pressure level must be kept below 140 dB. Subtracting the noise level from the signal level gives a dynamic measurement range of approximately 75 dB.

A3.5.2 Atmospheric absorption

The source-receiver dynamic range is further degraded by atmospheric absorption. It is well known that high frequency sound is attenuated as it propagates through the air due to a combination of thermal, viscous and molecular relaxation effects. Delany [A3.4] has made an extensive study of the attenuation mechanisms and derived a set of equations that enable corrections to be made based upon measurements of the ambient temperature, air pressure and relative humidity.

The results of calculations for typical indoor values of these
parameters shows that the attenuation can exceed 5 dB/metre
at 100 kHz.

A3.5.3 Digital processing equipment

The majority of the signal processing tasks undertaken during this
study were executed on a commercial digital spectrum analyser,
a Nicolet 660B. This is a dual channel analyser performing
a Fourier Transform on 1024 data points to produce a 400 line
spectrum over a pre-determined measurement bandwidth. Alternatively,
the instrument can produce a one third-octave band analysis over its
full measurement bandwidth of 100 kHz.

The analyser has five basic operating modes, but the only one
used for this study, was the dual channel mode. If the two input
signals are represented by A and B respectively, then the analyser
will calculate the cross-spectrum from the expression

$$G(f)_{AB} = A(f) \cdot B(f)$$

and the transfer function from the expression

$$H(f) = G(f)_{AB}/A(f)$$

The Nicolet is also capable of calculating the coherence function,
which for linear systems can be interpreted as the fractional
proportion of the mean square value of the output signal B(f) which
is contributed by the input signal A(f). The coherence function, $g^2(f)$
can be defined in terms of the cross-spectrum as

$$g^2(f)_{AB} = \frac{|G(f)_{AB}|^2}{|A(f)| . |B(f)|}$$

Measurement of the coherence function proved a useful means of estimating the influence of near surface turbulence upon grazing incidence propagation.

- 153 -

Figure 3.1 Bandwidth and Directivity of 1/4" Microphone with protection grid.
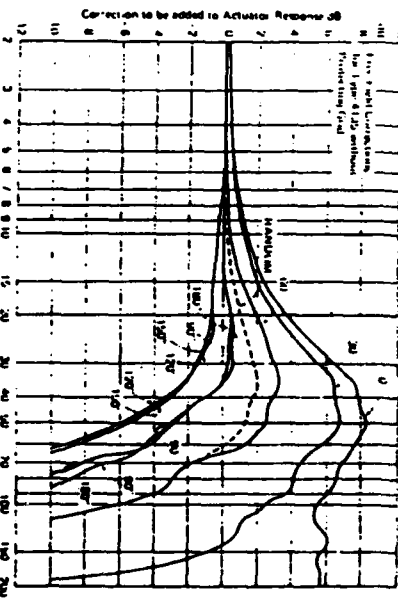
Figure 3.2 Bandwidth and Directivity of 1/4" Microphone without protection grid.
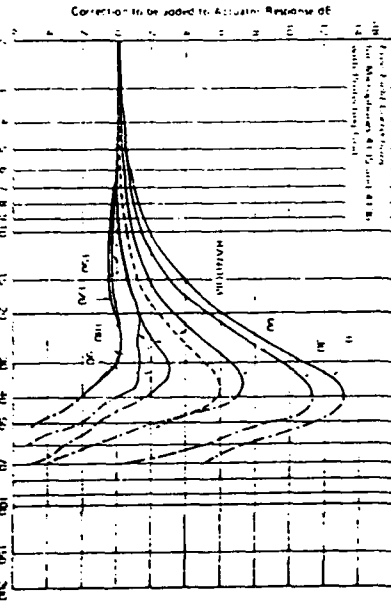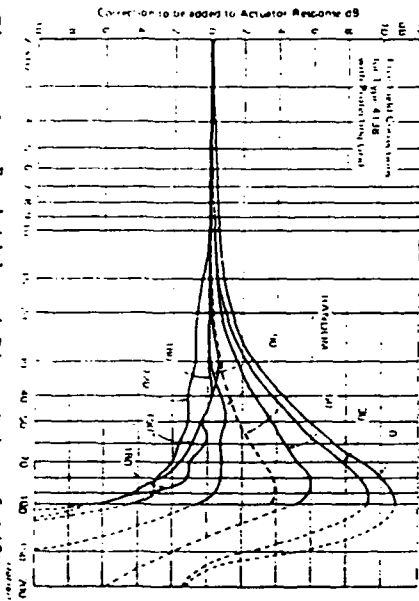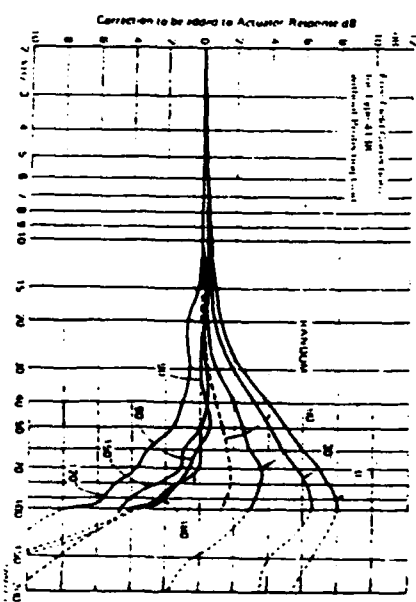

Figure A3.4 Bandwidth and Directivity of 1/8" Microphone with protection grid.

Figure A3.4 Bandwidth and Directivity of 1/8" Microphone without protection grid.

Thin Phosphor
Bronze Vanes

1.5 mm φ

40 lbs/in^2 air supply
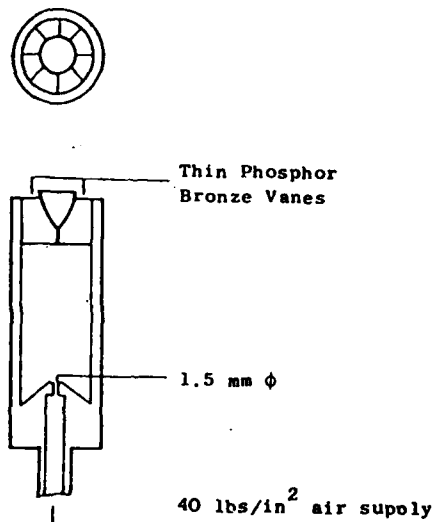
Figure A3.5 Air Jet Noise Source.
(After Delaney et al)
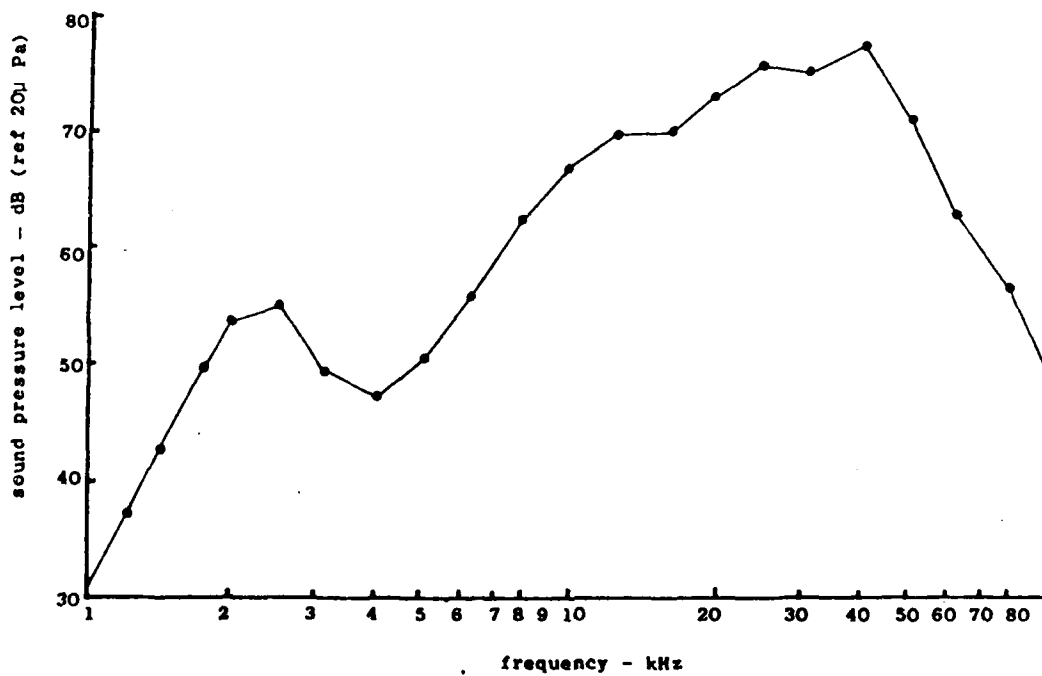
Figure A3.6 Air Jet Noise Source Spectrum at 100cm.
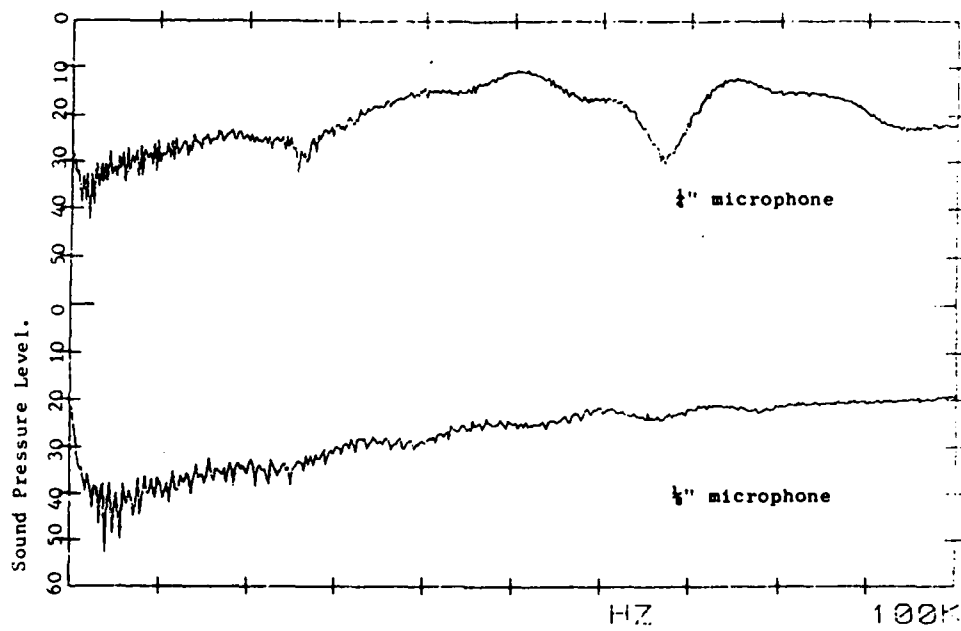
Figure A3.7 Spark Source Spectrum at 50cm.

- 156 -

LITERATURE CITED

A3.1   Bruel and Kjaer.: Microphones and Preamplifiers 1975

A3.2   Heap, N.W.: Sound Propagation Over Mixed Impedances.
        D.Phil Thesis, Open University 1982.

A3.3   Delaney, M.E. and Bazley.E.N.: Rennie, A.J. and Collins, K.M.:
        A scale Model Technique for Investigating Traffic Noise Propagation.
        J.S.V. (56) 325-340 1978

A3.4   Delaney, M.E. and Bazley, E.N.: Values of Air Attenuation for use
        in Free-Field Calibration of Microphones. NPL Airo Report, Ac45 1970.

APPENDIX 4

CALCULATION OF SURFACE INTENSITY RATIOS

A4.1   Semi-infinite medium

In this section we are interested in obtaining an expression for the square of the ratio, solid particle velocity to pressure at the surface, where the ground is considered to be of infinite depth. We consider a plane wave incident upon the interface at an angle θ_0 away from the normal.

We note that in a poro-elastic half space, there will in general be six types of waves. These consists of two dilatational and one shear wave in both the solid and fluid phases. In terms of scalar potentials, we write, for the solid phase

$$\phi_1' = a_s' \exp\left[-i\omega t - k'y \sin\theta' - k_1'x \cos\theta'\right]$$

$$\phi_1'' = a_s'' \exp\left[-i\omega t - k''y \sin\theta'' - k''x \cos\theta''\right]$$

$$\psi_1 = a_s^\gamma \exp\left[-i\omega t - k^\gamma y \sin\theta^\gamma - k^\gamma x \cos\theta\right] \tag{A4.1}$$

and for the fluid phase,

$$\phi_2' = \tau' \phi_1'$$

$$\phi_2'' = \tau'' \phi_2'$$

$$\phi_3 = \tau^\gamma \psi_r \tag{A4.2}$$

where k', k'' and k^γ are propogation constant as obtained in section 5.1 τ', τ'' and τ^γ are the following ratios of amplitudes

$$\tau' = a_f' / a_s'$$

$$\tau'' = a_f'' / a_s''$$

$$\tau^\gamma = a_f^r / a_s^r$$

and they can be obtained from the relation

$$\frac{a_f}{a_s} = \frac{\{-k^2 P + \rho_1 \omega^2 + i\omega k F(\omega)\}}{\{ k^2 Q + i\omega b F(\omega)\}} \tag{A4.3}$$

where k assumes the values k', k" and k^r respectively.

The solid and fluid displacements can be expressed in terms of the above potentials as

$$u_x = \frac{\partial \phi_1'}{\partial x} + \frac{\partial \phi_1''}{\partial x} + \frac{\partial \psi_1}{\partial y}$$

$$u_y = \frac{\partial \phi_1'}{\partial y} + \frac{\partial \phi_1''}{\partial y} - \frac{\partial \psi_1}{\partial x}$$

$$U_x = \frac{\partial \phi_2'}{\partial x} + \frac{\partial \phi_2''}{\partial x} + \frac{\partial \psi_2}{\partial y}$$

$$U_y = \frac{\partial \phi_2'}{\partial y} + \frac{\partial \phi_2''}{\partial y} - \frac{\partial \psi_2}{\partial x} \tag{A4.4}$$

and the relevant components of solid strain are

$$e_{xx} = \frac{\partial u_x}{\partial x}, \ e_{yy} = \frac{\partial u_y}{\partial y}, \ e_{xy} = \frac{1}{2}\left(\frac{\partial u_x}{\partial y} - \frac{\partial u_x}{\partial x}\right) \qquad (A4.5)$$

and finally the fluid dilatation

$$\varepsilon = \frac{\partial u_x}{\partial x} + \frac{\partial u_x}{\partial y} \qquad (A4.6)$$

We also have the stress-strain relations for an isotropic medium

$$\sigma_{ij} = (P - 2N)u_{kk}\delta_{ij} + 2N u_{ij} + Q U_{kk}\delta_{ij}$$

$$\sigma\delta_{ij} = - \Omega p_f \delta_{ij} = (Q u_{kk} + R U_{kk})\delta_{ij} \qquad (A4.7)$$

and implicit summation over repeated indices is assumed.

The normal solid particle velocity, V is given by

$$V_s = \frac{\partial u_x}{\partial t} \qquad (A4.8)$$

and from Eq (5.16), we have for V at the surface x = 0,

$$V_s = - i\omega \ [a_s' \ (i \ k' \cos \theta' + a_s'' \ (i \ k'' \cos \theta'')$$
$$+ \ a_s^r \ (i \ k^r \sin \theta \ r)]$$
$$x \exp \ [i \ k_o \sin \theta_o \ y \ - i \ \omega t] \qquad (A4.9)$$

Wherein, we have made use of the relation,

$$k_o \sin \theta_o = k' \sin \theta' = k'' \sin \theta^o = k^r \sin \theta^r \qquad (A4.10)$$

Also at the surface the normal stress in the frame must equal
stress in the fluid as both are acted upon by the outer air
presure p. Thus

$$\frac{\sigma_{xx}}{(1 - \Omega)} = \frac{\sigma}{\Omega} = -p$$

From the stress-strain relations (A4.7) we can express

$$p = -K_f \left[\left(\frac{1 - \Omega}{\Omega} \right) e + \epsilon \right]$$

and using (A4.5) and (A4.6), we get for the pressure of the surface

$$p = -K_f \left[-\left(\frac{1 - \Omega}{\Omega} \right) \left\{ -a_s'k'^2 - a_s''k''^2 \right\} + \left\{ \begin{array}{l} - a_s'\tau'k'^2 \\ - a_s'' k''^2 \tau'' \end{array} \right\} \right]$$
$$\times \exp[ik_o y \sin \theta_o - i\omega t] \qquad (A4.11)$$

From (A4.9) and (A4.11) we obtain the ratio of solid particle velocity
to the pressure at the surface i.e.

$$\frac{V_s}{p} = \frac{(1 - \Omega)\omega[\cos \theta' + \Gamma_1 \frac{k'}{k''} \cos \theta' + \Gamma_2 \frac{k'}{k^r} \sin \theta_x]}{K_f k' \left[\left(\frac{1 - \Omega}{\Omega} + \tau' \right) + \Gamma_1 \left(\frac{1 - \Omega}{\Omega} + \tau'' \right) \right]} \qquad (A4.12)$$

where

$$\Gamma_1 = \frac{a_s'' k''^2}{a_s' k'^2}$$

and

$$\Gamma_2 = \frac{a_s^r k^{r2}}{a_s' k'^2}$$

The constants Γ_1 and Γ_2 are as yet unknown and can be expressed in terms of known quantites with the help of the following conditions at the surface $x = 0$. These are:

i) vanishing of tangential stress at $x = 0$ i.e. $e_{xy} = 0$

ii) stress in the frame equals stress in the fluid i.e.

$$\frac{\sigma_{xx}}{1 - \Omega} = \frac{\sigma}{\Omega}$$

These two conditions provide two equations for Γ_1 and Γ_2 and after some algebra we have from (A4.5) and (A4.7),

$$\sin 2\, \theta'' \Gamma_1 - \cos 2\, \theta^r \Gamma_2 = - \sin 2\, \theta'$$

and

$$\{2\, N\Omega \cos^2\theta'' + [A\,\Omega - (1 - \Omega)Q]\}\, \Gamma_1 + N\Omega \sin 2\theta^r \Gamma_2$$
$$= 2\, N\Omega \cos^2 \theta^r - \{A\Omega - (1 - \Omega)Q\} \tag{A4.13}$$

which are solved to give

$$\Gamma_1 = \frac{-[N\Omega \tan 2\, \theta^r \sin 2\, \theta' + 2N\Omega \cos^2 \theta' + \{A\Omega - (1 - \Omega)Q\}]}{[N\Omega \tan 2\, \theta^r \sin 2\, \theta'' + 2N\Omega \cos^2 \theta'' + \{A\Omega - (1 - \Omega)Q\}]}$$

and

$$\Gamma_2 = \frac{\Gamma_1 \sin 2\, \theta'' + \sin 2\, \theta'}{\cos 2\, \theta^r} \tag{A4.14}$$

Now with the help of A4.14 and A4.12, the square of the ratio, solid particles velocity to the pressure at the surface can be readily computed once we know the propagation constants k', k'' and k^r.

In the case of normally incident ($\theta_o = 0$) plane wave, the ratio can be expressed in a compact form

$$\left| \frac{V_s}{p} \right|^2 = \frac{(1 - \Omega)^2 \, \omega^2 \left[\frac{1}{k'} - \frac{1}{k''} \right]^2}{k_f^2 \left[\tau' - \tau'' \right]^2}$$ (A4.15)

as $\Gamma_1 = -1$ and $\Gamma_2 = 0$

This result differs substantially from that obtained by Flohr and Cress [A4.1] wherein the ground has been considered as an elastic continuum. The present result is frequency dependent which is qualitatively consistent with their measurements.

A4.2 Rigidly-backed layer

The effect of inhomogeneity in the ground on the wave propagation
can be described by considering it as consisting of several layers
of differing properties. One such simple model is to consider
a finite depth of poro-elastic layer supported by a rigid semi-
infinite medium.

In this section, we derive an analogous expression to that of
Eq A4.15 for normally-incident plane waves. When such a plane
wave is incident upon the layered medium, inside the poro elastic
layer of depth say, d, there will in general be twelve possible
waves. As before, they can be represented as follows:

In the solid phase

$$\phi_1' = a_s' \exp(-i\omega t) \{ e^{+ik'n} + T'e^{-ik'x} \}$$

$$\phi_1'' = a_s'' \exp(-i\omega t) \{ e^{+ik''x} + T''e^{-ik''x} \}$$

$$\psi_1 = a_s^r \exp(-i\omega t) \{ e^{+ik^r x} + T^r e^{-ik^r n} \}$$

(A4.16)

In the fluid phase

$$\phi_2' = \tau' \, p_1'$$

$$\phi_2'' = \tau'' \, p_2''$$

$$\psi_2 = \tau^r \, p_1$$

The unknown quantities T', T'' and T^r denote the relative amplitudes
of backward travelling waves to the waves generated at the surface.

Now at the rigid backing (at $x = d$) the tangential stress (σ_{xy}) will be
zero, which in turn from stress-strain relations A4.7 implies that

$e_{xy} = 0$. Furthermore as the backing is hard the normal particle velocity is zero at the backing i.e.,

$$v_s = v_f = 0 \qquad \text{at } x = d$$

Also at the surface $n = 0$, the tangential stress, $e_{xy} = 0$.

Using the above conditions, after lengthy algebra, we obtain the following for the square of the ratio of solid particle velocity to pressure at the surface

$$\left[\frac{v_s}{P}\right]^2 = \frac{(1 - \Omega)^2 \, \omega^2 \left[\frac{1}{k'}\left(\frac{1 - e^{2\alpha}}{1 + e^{2\alpha}}\right) - \frac{1}{k''}\left(\frac{1 - e^{2\delta}}{1 + e^{2\delta}}\right) \right]^2}{K_f^2 \, (\tau' - \tau'')^2} \qquad (A4.17)$$

where

$$\alpha = ik'd \text{ and } \delta = ik''d$$

LITERATURE CITED

A4.1   Flohr, M.D. and Cress, D.H. Acoustic-to-seismic coupling
        properties and applications to seismic sensors.   Technical
        Reports E1-79-1 U.S. Army WES, February 1979

APPENDIX 5

MOTION OF THE INTERFACE.   THE GEOMETRIC APPROXIMATION

Using equations (6.18) and the integral expressions for the potentials,
and after performing the appropriate differentiations with respect
to z, we obtain the components of displacement at the interface where
z = 0:

$$u_r = \frac{\partial}{\partial r} \int_0^\infty \frac{1}{\Delta_0} \left[\Delta_3 + a_{32}\Delta_2 - \nu_4\Delta_4\right] \frac{e^{-\nu_1 z_0}}{\nu_1} J_0(Kr) K dK \tag{A5.1}$$

$$u_z = \int_0^\infty \frac{1}{\Delta_0} \left[\nu_3\Delta_3 + a_{32}\nu_2\Delta_2 + K^2\Delta_4\right] \frac{e^{-\nu_1 z_0}}{\nu_1} J_0(Kr) K dK \tag{A5.2}$$

These integrals are now in a form familiar in many analyses of reflected
spherical waves in which the reflected field is expressed as a
superposition of plane waves multiplied by the appropriate reflection
coefficient (Brekhovskikh [6.5]). In these the contribution from
the saddle point (at $K = k_1 \sin\theta$, where θ is the angle of incidence)
is obtained as an asymptotic expansion, the first term of which gives
the geometric approximation. Ignoring the contributions from the
branch cuts and poles, we have

$$u_r \sim \frac{\partial}{\partial r} \left[\frac{1}{\Delta_0} (\Delta_3 + a_{32}\Delta_2 - (k_1^2\sin^2\theta - k^2)^{\frac{1}{2}}\Delta_4)\frac{e^{ik_1 R}}{R} (1 + 0(R^{-1})) \right]$$

$$\text{or} \quad u_r \sim \frac{ik_1 \sin\theta}{\Delta_0} \left[\Delta_3 + a_{32}\Delta_2 - (k_1^2\sin^2\theta - k_4^2)^{\frac{1}{2}}\Delta_4\right] \frac{e^{ik_1 R}}{R} (1 + 0(R^{-1})) \tag{A5.3}$$

and

$$u_z \sim \frac{1}{\Delta_0} \left[(k_1^2 \sin^2 \theta - k_3^2)^{\frac{1}{2}} \Delta_3 + a_{32} (k_1^2 \sin^2 \theta - k_2^2)^{\frac{1}{2}} \Delta_2 \right.$$

$$\left. + k_1^2 \sin^2 \theta \, \Delta_4 \right] \frac{e^{ik_1 R}}{R} (1 + O(R^{-1})) \tag{A5.4}$$

where $R^2 = r^2 + z_0^2$, $\sin\theta = \frac{r}{R}$, and the determinants are evaluated

for $K = k_1 \sin\theta$.

We do not expect the geometric approximation to be valid at grazing

incidence because the determinants Δ_2, Δ_3, Δ_4 all contain a factor

ν_1, and thus approach zero as $\theta \rightarrow \pi/2$. To see this we recall that

they were formed by replacing columns 2, 3, or 4 of the matrix

in equation (6.47) by the vector on the right-hand side. This new

column may then be added to column 1 without affecting the value of

the determinant, and this results in a single non-zero element

$2\nu_1$ in the first column, which must be a factor of the determinant.

The evaluation of the higher order correction terms in the saddle -

point approximation would be over complicated because of the need

for 1st and 2nd derivatives of the various determinants. However,

we later use a simplified method which enables us to obtain the

correction term at grazing incidence.

A5.1 The branch cut integrals

If we treat each branch cut integral separately, then our problem in general is to evaluate an integral of the form

$$I = \int_0^\infty F(K) J_0(Kr) K dK$$

where $F(K)$ has a single branch point at, say, $K = k_j$. If we write

$$I = \lim_{z' \to 0} \int_0^\infty F(K) e^{-\nu_j z'} J_0(Kr) K dK$$

where $\nu_j^2 = K^2 - k_j^2$, $\operatorname{Re}\nu > 0$, then the integration around the branch cut becomes implicit.

We now expand $F(K)$ as a Taylor series in ν_j, so that

$$F(K) = F(k_j) + \frac{dF}{d\nu} \nu_j + \frac{1}{2} \frac{dF}{d\nu_j} \nu_j +$$

We now require the integrals

$$\lim_{z' \to 0} \int_0^\infty e^{-\nu_j z'} J_0(Kr) K dK = \lim_{z' \to 0} \left[\frac{\partial}{\partial z'} \left(\frac{e^{ik_j R'}}{R'} \right) \right]$$

$$= 0$$

where $R'^2 = r^2 + z'^2$,

$$\lim_{z \to 0} \int_0^\infty \nu_j e^{-\nu_j z'} J_0(Kr) K dK = \lim_{z' \to 0} \left[\frac{\partial^2}{\partial z'^2} \left(\frac{e^{ik_j R'}}{R'} \right) \right],$$

$$= \frac{e^{ik_j r}}{r^2} \left(ik_j - \frac{1}{r} \right).$$

where we have used the integral representation for a source of spherical waves, as in section 6.8. These are sufficient to enable us to evaluate the integral to terms in $\frac{1}{r^2}$, and we now have

$$I \sim \left(\frac{dF}{d\nu_j}\right)_{k=k_j} \frac{ik_j e^{ik_j z}}{r^2} + O(r^{-3}) \tag{A5.5}$$

Inspection of the matrix in equation (6.47) shows that for all terms in equations (A5.1), (A5.2) we can write in general form

$$F(K) = \frac{g_1(K) + \nu_j h_1(K)}{g_2(K) + \nu_j h_2(K)} \tag{A5.6}$$

giving

$$\left(\frac{dF}{d\nu_j}\right)_{K=k_j} = \frac{h_1(k_j)g_2(k_j) - h_2(k_j)g_1(k_j)}{[g_2(k_j)]^2} \tag{A5.7}$$

The analysis given here has not been rigorous, and certainly one questionable item is the convergence of the Taylor series for $F(K)$. Without giving a detailed discussion, this will be in doubt when $g_2(k_j)$ is small, implying a pole near the branch point. To find an upper limit for the branch cut integral we ignore g_2, leaving

$$F(K) = \frac{g_1(K)}{\nu_j h_2(K)} + \frac{h_1(K)}{h_2(K)}$$

The second term gives no contribution, and we now have

$$I = \lim_{z' \to 0} \int_0^\infty \frac{g_1(K)}{h_2(K)} \frac{e^{-\nu_j z'}}{\nu_j} J_0(Kr)KdK$$

Using the methods of section 6.11, this gives

$$I \sim \frac{g_1(k_j)}{h_2(k_j)} \frac{e^{ik_j r}}{r} + O(r^{-2}) \tag{A5.8}$$

We therefore expect equation A5.5 to be valid only if

$$\left| \frac{g_1(k_j)}{h_2(k_j)} \frac{e^{ik_j r}}{r} \right| \gg \left| \frac{ik_1 (h_1(k_j)g_2(k_j) - h_2(k_j)g_1(k_j))}{[g_2(k_j)]^2} \frac{e^{ik_j r}}{r^2} \right|$$

or

$$\left| \frac{r\, g_1(k_j)\, [g_2(k_j)]^2}{k_j h_2(k_j)[h_1(k_j)g_2(k_j) - h_2(k_j)g_1(k_j)]} \right| \gg 1 \qquad (A5.9)$$

This quantity may be regarded as related to the numerical distance established more precisely for the rigid porous medium.

A5.2 Grazing incidence

Although the evaluation of the correction term in the saddle-point integral is impractical for an elevated source, when $z_o = 0$ the integral may be handled in exactly the same way as any other branch cut integral. This gives us the correction term for grazing incidence, and this may be a useful approximation for all cases where the geometric term is not dominant.

As a demonstration, we again consider the field at the surface of a rigid porous half-space at grazing incidence. This is given by

$$\phi \sim \frac{2i}{k_1 M^2 (n^2-1)} \frac{e^{ik_1 r}}{r^2} + O(r^{-3})$$

The upper limit is

$$\phi \sim 2 \frac{e^{ik_1 r}}{r}$$

and (6.64) becomes

$$\left| k_1 r M^2 (n^2 - 1) \right| \gg 1$$

These results are the limiting case of the more elaborate saddle-point integration.

A5.3   The k_1 branch cut integrals

To keep the expressions for the integrals as compact as possible, we define δ_{ijk} as the cofactor of the matrix element in row j and column k in the expansion of the determinant Δ_1. We then find expressions for g_1, c_1 etc. in the general equation (A5.6)

When dealing with the k_1 branch cut integral, we must have $z_o = 0$. In equation (A5.1) we obtain

$$g_1(k_1) = 2(\delta_{311}(k_1) + a_{32} \delta_{211}(k_1) - (k_1^2 - k_4^2)^{\frac{1}{2}} \delta_{411})$$

$$h_1(k_1) = 0$$

$$g_2(k_1) = \Delta_o(k_1) \qquad h_2(k_1) = \delta_{011}(k_1)$$

and in equation (A5.2)

$$g_1(k_1) = 2 ((k_1^2 - k^2)^{\frac{1}{2}} \delta_{311} + a_{32}(k_1^2 - K^2)^{\frac{1}{2}} \delta_{211} + k_1^2 \delta_{411})$$

$$h_1(k_1) = 0, \quad g_2(k_1) = \Delta_o(k_1), \quad h_2(k_1) = \delta_{011}(k_1)$$

Using equation (A5.5), and noting that

$$\frac{\partial}{\partial r} \left(\frac{e^{ik_1 r}}{r^2} \right) = \frac{ik_1 e^{ik_1 r}}{r^2} + 0(r^{-3})$$

we obtain the displacements in the far-field

$$u_r = \frac{2 k_1^2 \delta_{011} [\delta_{311} + a_{32} \delta_{211} - (k_1^2 - k_4^2)^{\frac{1}{2}} \delta_{411}]}{\Delta_o^2} \frac{e^{ik_1 r}}{r^2} \qquad (A5.10)$$

$$u_z = \frac{-2ik_1\delta_{011}\left[(k_1^2 - k_2^2)^{\frac{1}{2}}\delta_{311} + a_{32}(k_1^2 - k_2^2)\delta_{211} + k_1^2\delta_{411}\right]}{\Delta_0^6} \frac{e^{ik_1r}}{r^2} \qquad (A5.11)$$

Using (A5.9), these expressions will be valid if

$$\frac{r\Delta_0^2}{k_1^2\delta_{011}} \gg 1 \qquad (A5.12)$$

A5.4 The k_2 branch cut integrals

For this and the remaining branch cut integrals we are not limited to $z_0 = 0$, but otherwise we proceed as before. For u_r we have

$$g_1 = \frac{e^{-\nu_1 z_0}}{\nu_1} [\Delta_3 + a_{32}\Delta_2 - \nu_4\Delta_4] \tag{A5.13}$$

$$h_1 = \frac{e^{-\nu_1 z_0}}{\nu_1} [\delta_{412} + a_{32}\delta_{342} - \nu_4(\delta_{412} + a_{32}\delta_{442})] \tag{A5.14}$$

$$g_2 = \Delta_0 \tag{A5.15}$$

$$h_2 = \delta_{012} + a_{32}\delta_{042} \tag{A5.16}$$

and for u_z

$$g_1 = \frac{e^{-\nu_1 z_0}}{\nu_1} [\nu_3\Delta_3 + k_2^2\Delta_4] \tag{A5.17}$$

$$h_1 = \frac{e^{-\nu_1 z_0}}{\nu_1} [a_{32}\Delta_2 + \nu_3(\delta_{412} + a_{32}\delta_{342}) + k_2^2(\delta_{412} + a_{32}\delta_{442})] \tag{A5.18}$$

$$g_2 = \Delta_0 \quad , \quad h_2 = \delta_{012} + a_{32}\delta_{042} \tag{A5.19},(A5.20)$$

where it is assumed that all expressions are evaluated for $K = k_2$. We shall not carry out here the straightforward substitution into equations (A5.7) and (A5.5).

A5.5 The k_3 branch cut integrals

For u_r

$$g_1 = \frac{e^{-\nu_1 z_0}}{\nu_1} [\Delta_3 + a_{32}\Delta_2 - \nu_4\Delta_4] \tag{A5.21}$$

$$h_1 = \frac{e^{-\nu_1 z_0}}{\nu_1} [a_{32}(\delta_{243} + a_{23}\delta_{213}) - \nu_4(\delta_{443} + a_{24}\delta_{413})] \tag{A5.22}$$

$$g_2 = \Delta_0 \tag{A5.23}$$

$$h_2 = \delta_{043} + a_{23}\delta_{013} \tag{A5.24}$$

and for u_z

$$g_1 = \frac{e^{-\nu_1 z_0}}{\nu_1} [a_{32}\nu_2\Delta_2 + k_3^2\Delta_4] \tag{A5.25}$$

$$h_1 = \frac{e^{-\nu_1 z_0}}{\nu_1} [\Delta_3 + a_{32}\nu_2(\delta_{243} + a_{23}\delta_{213}) + k_3^2(\delta_{443} + a_{23}\delta_{413})] \tag{A5.26}$$

$$g_2 = \Delta_0 \tag{A5.27}$$

$$h_2 = \delta_{043} + a_{23}\delta_{013} \tag{A5.28}$$

where all evaluations are carried for $K = k_3$.

A5.6   The k_4 branch cut integrals

For u_r

$$g_1 = \frac{e^{-\nu_1 z_0}}{\nu_1} [\Delta_3 + a_{32} \Delta_2]$$

(A5.29)

$$h_1 = \frac{-e^{-\nu_1 z_0}}{\nu_1} [\Delta_4 + 2\mu k_4^2 (\delta_{334} + a_{32} \delta_{234})]$$

(A5.30)

$$g_2 = \Delta_0$$

(A5.31)

$$h_2 = -2\mu k^2 \delta_{034}$$

(A5.32)

and for u_z

$$g_1 = \frac{e^{-\nu_1 z_0}}{\nu_1} [\nu_3 \Delta_3 + a_{32} \nu_2 \Delta_2 + k_4^2 \Delta_4]$$

(A5.33)

$$h_1 = \frac{-e^{-\nu_1 z_0}}{\nu_1} [2\mu k_4^2 (\nu_3 \delta_{334} + a_{32} \nu_2 \delta_{234})]$$

(A5.34)

$$g_2 = \Delta_0$$

(A5.35)

$$h_2 = -2\mu k_4^2 \delta_{034}$$

(A5.36)

where the evaluations are carried out for $K = k_4$.

A5.7 Surface waves

Surface wave contributions will occur when poles of the various integrands lie
between the real axis and the contour of integration. For this to happen
we must have $\Delta_o = 0$.

When the wavenumbers of the different wave types are real, a true surface
wave must have a real wavenumber greater than these ([6.3], [6.4]).
When at least one wavenumber is complex, as in our application, the
situation is less clear. In general it will be necessary to search
for zeros of Δ_o by some numerical means, and also to establish criteria
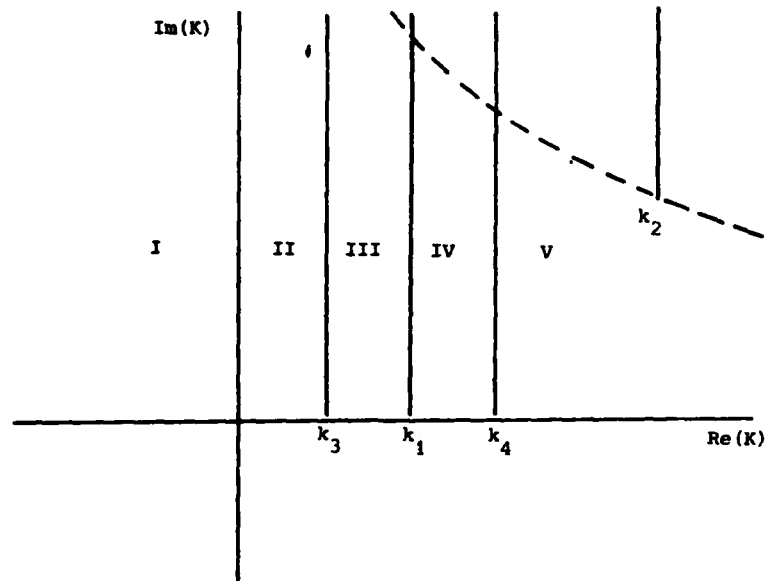as to whether they lie within the closed integration contour.

The general form of the required integral is

$$I = \int_0^\infty F(K) J_o(Kr) K dK$$

which may be rewritten as

$$I = \tfrac{1}{2} \int_{-\infty}^\infty F(K) H_o^1(Kr) K dK \qquad (A5.37)$$

In the simplifying case of grazing incidence the required integration
contours are those which pass around the vertical branch cuts emanating
from the branch points at k_1, k_2, k_3, k_4.

A typical situation is shown in the diagram, where poles in any of the
regions I - V will contribute to the integral. The signs of the
square roots ν_1, ν_2 etc. depend on the region, and in region I

$$Re\ \nu_1 > 0 \qquad Im\ \nu_1 < 0$$
$$Re\ \nu_2 > 0 \qquad Im\ \nu_2 < 0$$
$$Re\ \nu_3 > 0 \qquad Im\ \nu_3 < 0$$
$$Re\ \nu_4 > 0 \qquad Im\ \nu_4 < 0$$

In region II

$$Re\ \nu_1 < 0 \qquad Im\ \nu_1 < 0$$
$$Re\ \nu_2 > 0 \qquad Im\ \nu_2 < 0$$
$$Re\ \nu_3 < 0 \qquad Im\ \nu_3 < 0$$
$$Re\ \nu_4 < 0 \qquad Im\ \nu_4 < 0$$

In region III

$$\text{Re } \nu_1 < 0 \qquad \text{Im } \nu_1 < 0$$

$$\text{Re } \nu_2 > 0 \qquad \text{Im } \nu_2 < 0$$

$$\text{Re } \nu_3 > 0 \qquad \text{Im } \nu_3 > 0$$

$$\text{Re } \nu_4 < 0 \qquad \text{Im } \nu_4 < 0$$

In region IV

$$\text{Re } \nu_1 > 0 \qquad \text{Im } \nu_1 > 0$$

$$\text{Re } \nu_2 > 0 \qquad \text{Im } \nu_2 < 0$$

$$\text{Re } \nu_3 > 0 \qquad \text{Im } \nu_3 > 0$$

$$\text{Re } \nu_4 < 0 \qquad \text{Im } \nu_4 < 0$$

In region V

$$\text{Re } \nu_1 > 0 \qquad \text{Im } \nu_1 > 0$$

$$\text{Re } \nu_2 > 0 \qquad \text{Im } \nu_2 < 0$$

$$\text{Re } \nu_3 > 0 \qquad \text{Im } \nu_3 > 0$$

$$\text{Re } \nu_4 > 0 \qquad \text{Im } \nu_4 > 0$$

Here we have assumed that the pole lies below the dashed line which
consists of the contours $\text{Re } \nu_2 = 0$ and $\text{Im } \nu_2 = 0$.

We now write the integrals as

$$I = I_1 + I_2 + I_3 + I_4 + 2\pi i \text{ res } (K_p)$$

where I_1, I_2 etc. are the branch cut integrals, and $\text{res}(K_p)$ represents
the residues of any poles lying within the prescribed regions.

In equation 6.92 we have in general

$$F(K) = G(k)/\Delta_o$$

giving

$$\text{res}(K_p) = \frac{K_p}{2} \frac{G(K_p)}{\Delta_o'(K_p)} H_o^1 (K_p r)$$

where $\Delta_o'(K_p) = \frac{d\Delta_o}{dK}$, $K = K_p$

Using the asymptotic representation for the Hankel function, we obtain

$$2\pi i \text{ res}(K_p) \sim \frac{G(K_p)}{\Delta_o'(K_p)} \left(\frac{2i\pi K_p}{r}\right)^{\frac{1}{2}} + 0 (r^{-3/2}) \qquad (A5.38)$$

Making use of equations A5.1 and A5.2 the surface wave contributions to the ground motion are

$$u_r \sim \frac{iK_p}{\nu_1 \Delta_o'} \left[\Delta_3 + a_{32}\Delta_2 - \nu_4\Delta_4\right] \left(\frac{2i\pi K_p}{r}\right)^{\frac{1}{2}} e^{-\nu_1 z_o + iK_p r} + 0(r^{-3/2}) \quad (A5.39)$$

$$u_z \sim \frac{1}{\nu_1 \Delta_o'} \left[\nu_3\Delta_3 + a_{32}\nu_2\Delta_2 + K_p^2\Delta_4\right] \left(\frac{2i\pi K_p}{r}\right)^{\frac{1}{2}} e^{-\nu_1 z_o + iK_p r}$$

$$+ 0(r^{-3/2}) \qquad (A5.40)$$

where $\nu_1, \nu_2, \nu_3, \nu_4, \Delta'_o, \Delta_2, \Delta_3, \Delta_4$ are evaluated for $K = Kp$.

The major difficulties are the determination of K_p, and the evaluation of $\Delta'_o (K_p)$. In the next section we use a light fluid approximation which simplifies the problem considerably.

A5.8 The light fluid limit.

A limiting case of some interest occurs when the density of the fluid is much less than that of the solid in the lower medium, and we expect this to be applicable when modelling ground surfaces. In this case we have $\rho_1 << \rho$, $\rho_2 << \rho$, and also recall from the theory of rigid porous media that $\rho_1 << \rho_2$ at low frequencies. Since we expect the propagation constants of the various wave types to be roughly comparable, then the compressibility of the fluid must also be much greater than that of the solid.

If we examine the effect of this on the fast and slow waves, then the approximations

$$k_2 \simeq k'_2, \quad k_3 \simeq k'_3$$

are valid if

$$\frac{M}{H} \ll 1, \quad \frac{\rho_1^2}{\rho\rho^2} \ll 1$$

It should be remarked here that α is always less than unity in Biot's theory.

For the shear wave

$$k_4^2 \simeq \frac{\omega^2 \rho}{\mu} \quad \text{if} \quad \frac{\rho_1^2}{\rho\rho_2^2} \ll 1$$

From equation 6.36

$$a_{32} \simeq \frac{\rho^2}{\rho} \, (\frac{\rho_1}{\rho_2} - \alpha)/(\frac{k'^2_2}{k'^2_3} - 1) \tag{A5.41}$$

$$= \frac{M}{H} \, (\frac{\rho_1}{\rho_2} - \alpha)/(1 - \frac{k'^2_3}{k'^2_2}) \tag{A5.42}$$

and if $k'^2_3 < k'^2_2$, $\frac{M}{H} \ll 1$ implies $a_{32} \ll 1$.

From equation 6.37

$$a_{23} \simeq (\frac{k'^2_3}{k'^2_2} \alpha - \frac{\rho_1}{\rho_2})/(1 - \frac{k'^2_3}{k'^2_2}) \tag{A5.43}$$
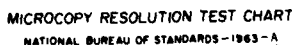
MICROCOPY RESOLUTION TEST CHART

NATIONAL BUREAU OF STANDARDS-1963-A

These expressions simplify further if $\rho_1/\rho_2 \ll \alpha$, and $k_3'^2 \ll k_2'^2$.

Since the fast wave will invariably have the highest velocity of all wave types, this latter condition is effectively one of local reaction. Under these circumstances we have

$$a_{32} \simeq \frac{-\alpha M}{H} \tag{A5.44}$$

$$a_{23} \simeq \frac{\alpha M}{H} \frac{\rho}{\rho_2} = \alpha \frac{k_3'^2}{k_3'^2} \tag{A5.45}$$

In the light fluid limit we can also show that

$$\Delta_o \simeq \Delta_a \, \Delta_b \tag{A5.46}$$

where

$$\Delta_a = \omega^2 \, (\rho_2 \nu_1 + \rho_1 \nu_2) \tag{A5.47}$$

$$\Delta_b = (2\mu\kappa^2 - k_3'^2 H)(\tfrac{1}{2}k_4^2 - \kappa^2)$$

$$- 2\mu\nu_3\nu_4\kappa^2 \tag{A5.48}$$

It can be seen that equation (A5.47) is the denominator found for the rigid porous case, and (A5.48) is the Rayleigh denominator for a semi-infinite elastic half-space. This is intuitively appealing since it means that in the light fluid limit wave propagation in the upper medium is identical to that for the rigid porous half-space, while the Rayleigh surface wave is virtually unaffected by the presence of the fluid.

Air-coupled surface waves of the Rayleigh type have been found

experimentally [6.2], so we suspect that poles corresponding to the
zeros of (A5.48) will be of importance. In the surface wave expressions
given in section (A5.7) we now have

$$\Delta_o{}'(K_p) = \Delta_a(K_p)\Delta_b{}'(K_p) \qquad\qquad (A5.49)$$

where

$$\Delta_b(K_p) = 0 \qquad\qquad (A5.50)$$

A5.9 Practical Calculations.

The calculation of the plane wave and branch cut contributions present no difficulty, but to obtain any surface wave contribution we need to find a zero of Δ_o and its derivative at this point (see section A5.7). To do this in practice we have used a numerical technique known as Muller's method (described in reference A5.5) which finds a root of an analytic complex function by using quadratic interpolation. Three initial guesses are used to obtain the first quadratic, and the nearest zero of this provides the next approximation to the unknown root, and the iteration is continued until the required accuracy is achieved. This root gives us the surface wave number K_p. Consequently it is a simple matter to find the derivative $\Delta_o' (K_p)$ by calculating the gradient of the last fitted quadratic.

From the considerations of the previous section we expect a surface wave of the Rayleigh type which will have a wave number approximately 1.2 times that of the shear wave, k_4. Using three initial guesses $1.15k_4$, $1.2k_4$ and $1.25k_4$ resulted in rapid convergence for all the examples tried, and there was no indication of any problem arising from the non-analytic nature of Δ_o (due to the branch cuts)

A5.10 Material parameters for soil.

Sound velocity (ω/k_1)	3.4×10^4 cm s^{-1}
Density of air (ρ_1)	1.2×10^{-3} g cm^{-3}
P - wave velocity $(\omega/\text{Re}(k_3'))$	5.0×10^4 cm s^{-1}

Im (k_3')/ Re(k_3')	1.25×10^{-2}
S - wave velocity $(\omega/\text{Re}(k_4))$	3.2×10^{4} cm s^{-1}
Im(k_4)/Re(k_4)	1.25×10^{-2}
Density of porous medium (ρ)	1.3 g cm^{-3}
Tortuosity	2.5
Shape factor	0.75
Flow resistivity	250 cgs rayls
Porosity	0.4
α	0.5

The imaginary parts of the compressional and shear wave numbers are consistent with the results found by Prange [A5.6] for attenuation in soils.

The tortuosity, shape factor, flow resistivity, and porosity are used to determine the equivalent rigid-porous wave number k_2' and complex density ρ_2 (see chapter 5). The value chosen for the parameter α is arbitrary, apart from the constraint in Biot's theory that it must lie between the porosity and unity. However, we did repeat some of the calculations for $\alpha = 0.9$, and found that the changes to the computed surface velocity were not more than 2dB, and in most cases considerably less.

A5.11   Results

Figures A5.1 - A5.5 show the contributions of the various wave types to the vertical component of surface velocity for a source height of 1 m and a horizontal separation of 100 m.   These are the plane wave

approximation, the near and far-field approximations to the k_1, k_3 and k_4 branch cut integrals, and the Rayleigh-type surface wave. The k_2 branch cut integral was always negligible because of rapid attenuation of the slow wave.

Figures A5.6 - A5.8 show the dominant contributions for source heights of zero, 1 m and 50 m.

In all these cases a point source of spherical waves is used, such that the pressure amplitude of the incident wave is

$$P = \frac{e^{ik_1 R}}{R}$$

The results show that with the source on the surface the main contributions are those of the Rayleigh-type wave and the k_1 branch cut integral. The Rayleigh wave dominates below 200 Hz, but is attenuated at higher frequencies. Elevation of the source to 1 m gives a significant plane wave contribution, which becomes increasingly dominant at high frequencies. The plane wave term dominates at all frequencies when the source height is increased to 50 m. There are contributions from the k_3 and k_4 branch cuts, but these are always a small part of the total motion.

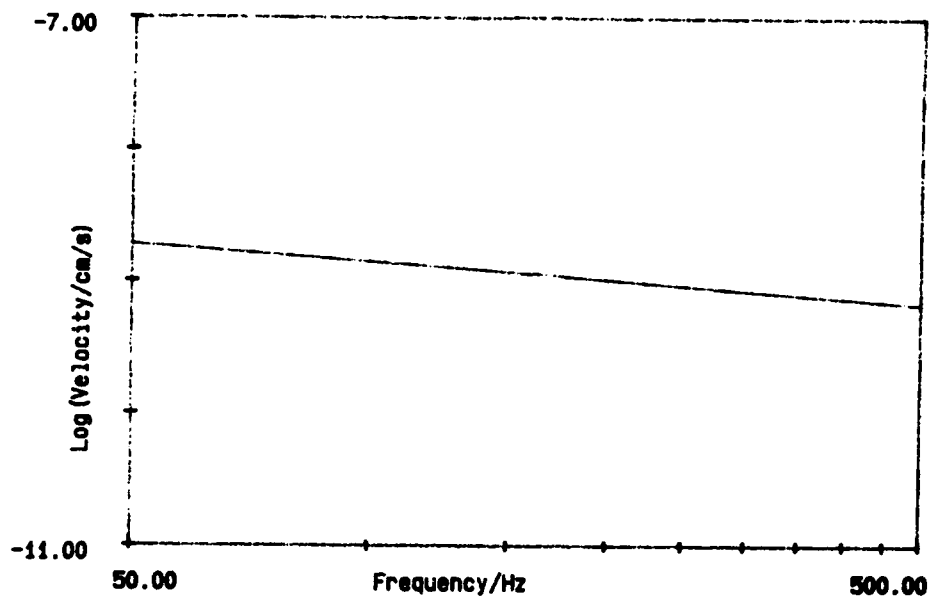Figure A5.1 Plane Wave Contribution for a Source Height of 1 m

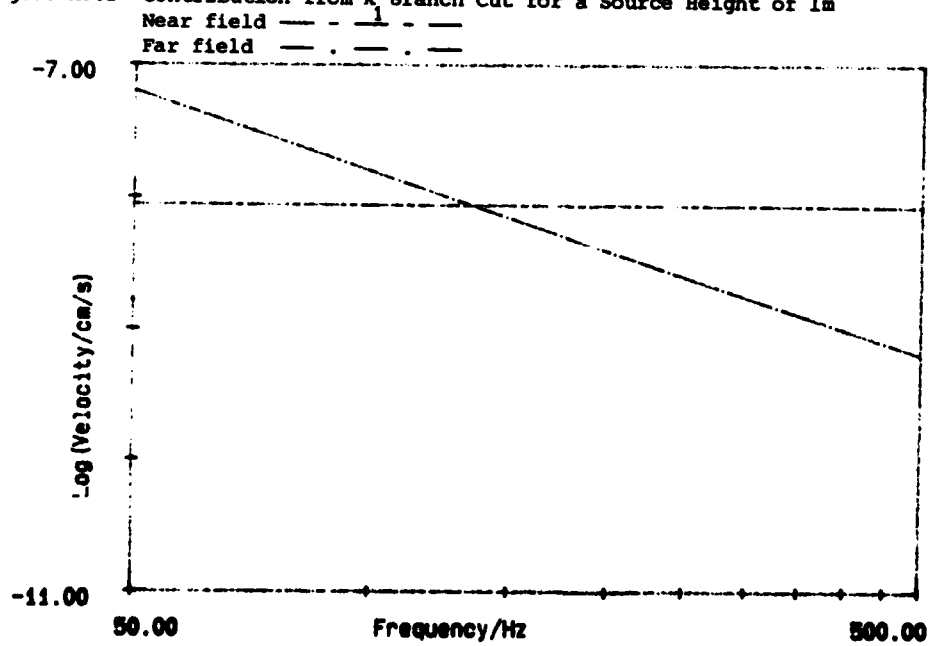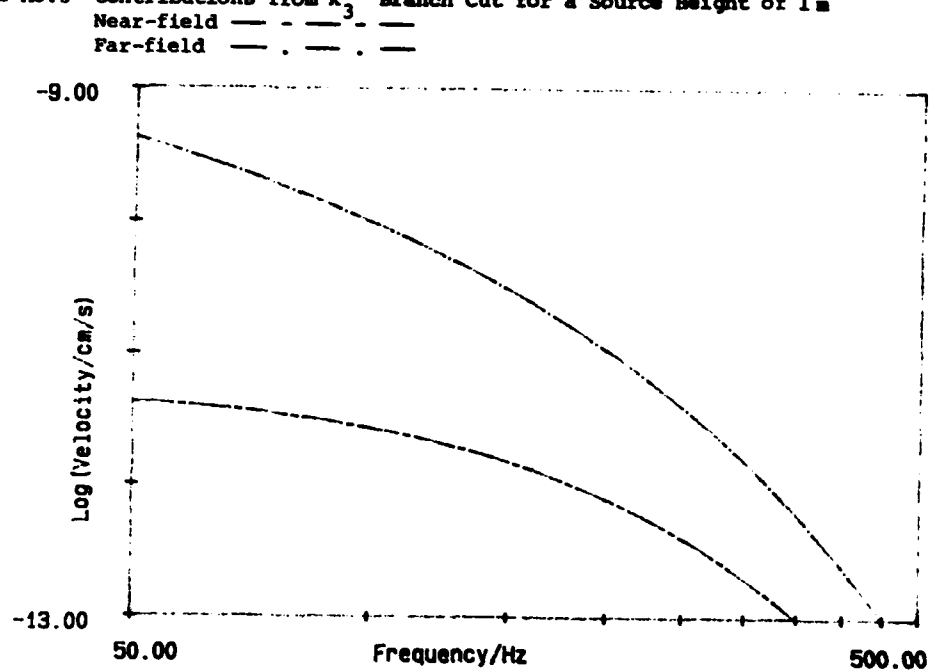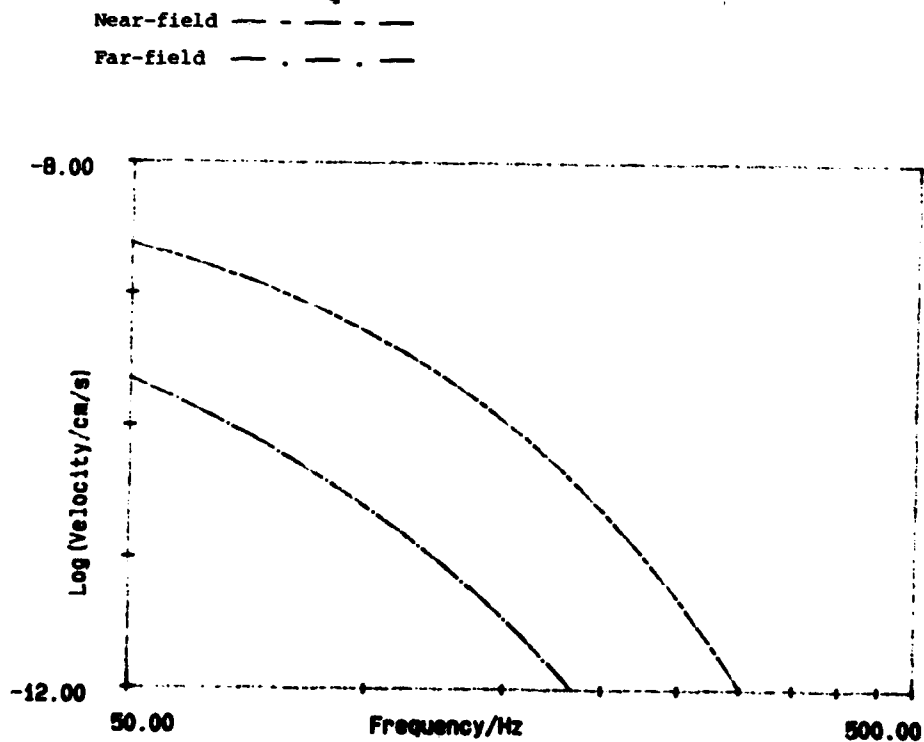Figure A5.2 Contribution from k Branch Cut for a Source Height of 1m
            Near field — - — 1 - —
            Far field — . — . —

Figure A5.3 Contributions from k_3 Branch Cut for a Source Height of 1 m
Near-field — · — · —
Far-field — · — · —

Figure A5.4 Contribution from k_4 Branch Cut for a Source Height of 1 m
Near-field — · — · —
Far-field — · — · —

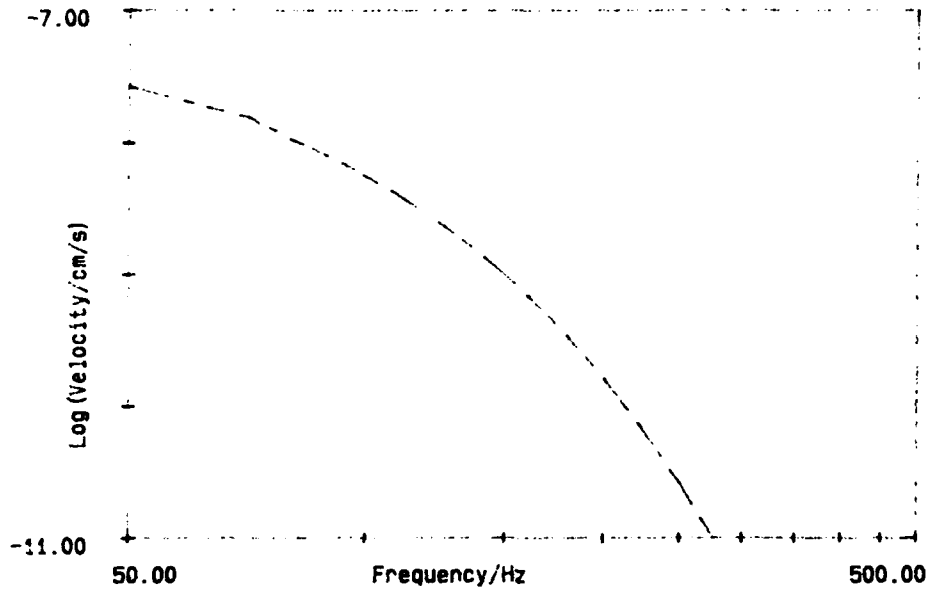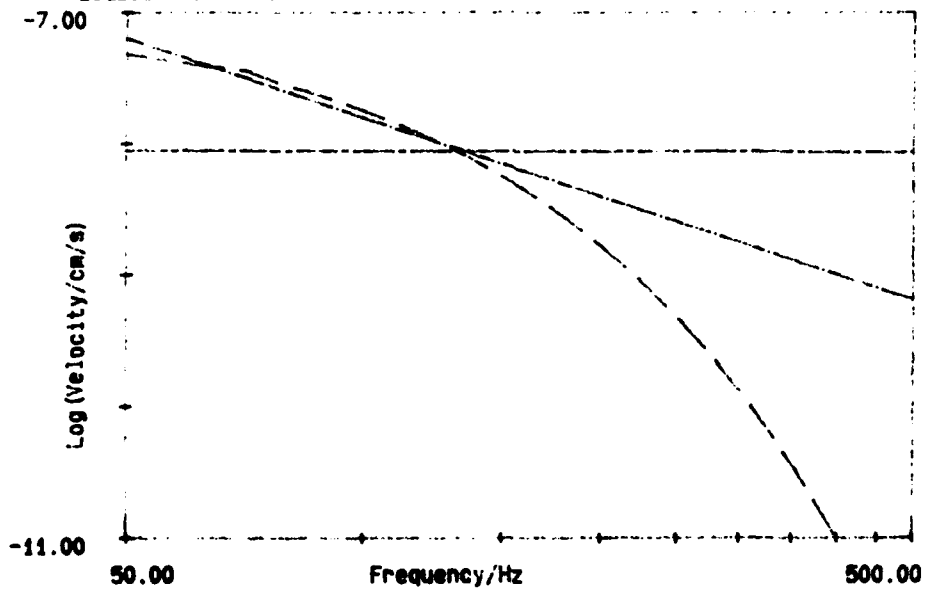Figure A5.5 Contribution from Rayleigh-type Wave for a Source Height of 1m

Figure A5.6 Contributions from k_1 Cut (Near- and Far-Field) and Rayleigh-Type Wave for Source and Receiver Both on Surface

Figure A5.7 Contributions from Plane Wave, k_1 Branch Cut (Near- and Far-Field) and
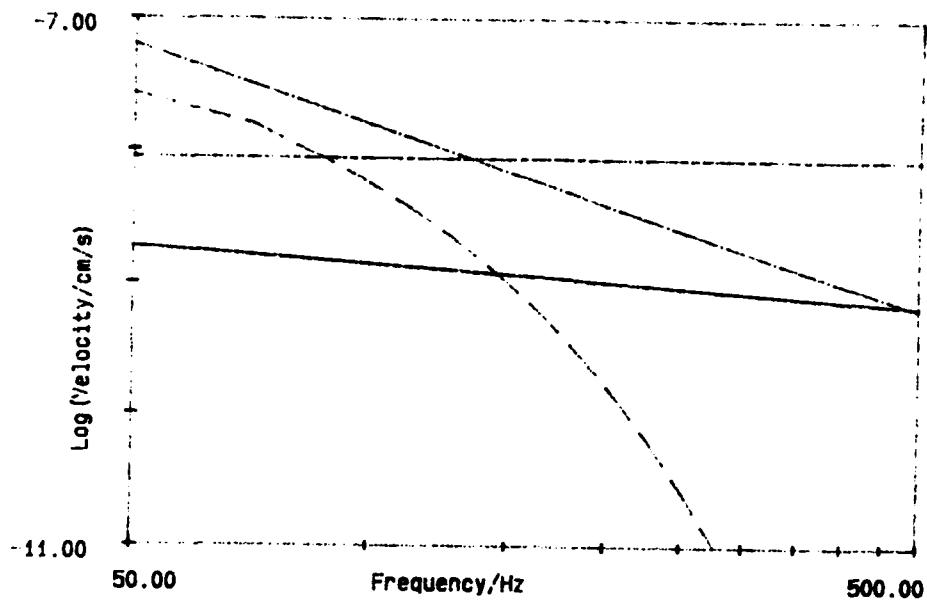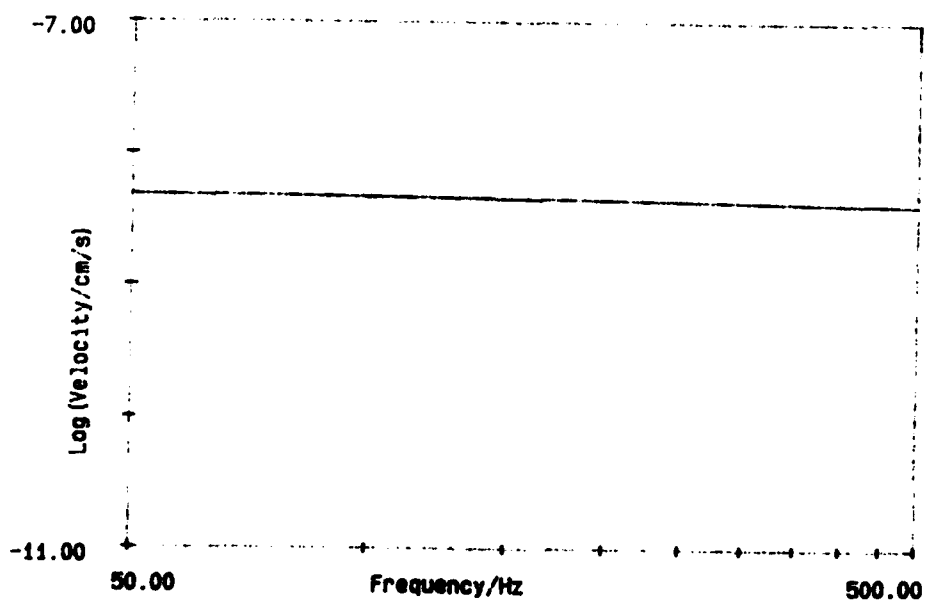Rayleigh-type Wave for Source Height of 1 m

Figure A5.8 Dominant Plane-Wave Contribution for a Source Height of 50 m

LITERATURE CITED

A.5.1   W.M. Ewing, W.S. Jardetsky and F. Press.
         Elastic Waves in Layered Media 1957 McGraw-Hill

A5.2   S.Feng and D.L. Johnson
         High Frequency Acoustic Properties of a Fluid/Porous Solid
         Interface. I. New Surface Mode
         J. Acoustic. Soc. Amer. 74 (3) 906-914 (1983)

A5.3   S. Feng and D.L. Johnson. High Frequency Acoustic Properties
         of a Fluid/Porous Solid Interface. II The 2D Reflection Green's
         Function. J. Acoustic Soc. Amer. 74 (3) 915-924 (1983)

A5.4   L. M. Brekhovskikh. Waves in Layered Media 1980 Academic Press.

A5.5   F.D. Conte and C. de Boor
         Elementary Numerical Analysis: An Algorithmic Approach.
         McGraw-Hill, New York, 1972.

A5.6   B. Prange.
         Parameters affecting damping properties.
         Proc. DMSR 77, Karlsruhe, 1977, Vol.1, p.61.

END

DATE
FILMED

3   84